

TECHNISCHE UNIVERSITÄT MÜNCHEN  
FAKULTÄT FÜR INFORMATIK



MASTER'S THESIS  
IN COMPUTER SCIENCE

Volume Flow Determination in the Cranial Vessel Tree  
Based on Quantitative Magnetic Resonance Data

Volumendurchflussbestimmung im kraniellen Gefäßbaum  
anhand von quantitativen Magnetresonanzdaten

Author: Jürgen Sotke  
Supervisor: Prof. Dr. Nassir Navab  
Advisor: Andreas Keil  
Thomas Seiler  
Submission Date: February, 15<sup>th</sup> 2008

Erklärung

*„Ich versichere, dass ich diese Master's Thesis selbständig verfasst und nur die angegebenen Quellen und Hilfsmittel verwendet habe.“*

Declaration

*"I assure the single handed composition of this master's thesis only supported by declared resources."*

Garching, den 14. Februar 2008

---

Jürgen Sotke

## Abstract

Phase Contrast Angiography (PCA) is a special technique used in Magnetic Resonance (MR) imaging, which is capable to detect the flow velocity of fluids. When it comes to the evaluation of blood flow in the human body, PCA has replaced other techniques for many diagnostic tasks within the last decade. Apart from technical improvements of both, MR scanners as well as scanning protocols, the reason for its increased employment are its noninvasiveness and the reliability of the results. Technical limitations of PCA, however, usually require a bipartite workflow for Quantitative Magnetic Resonance Angiography (QMRA) so far. It consists of a preliminary anatomical scan and the quantitative evaluation itself. A novel approach is proposed in this thesis to eliminate the necessity of the preceding anatomical scan for QMRA analysis. In order to achieve this, the segmentation of the vessel tree is performed on the PCA data itself. From the segmentation result an abstract model of the vessel tree is generated, which allows combining the topological information from this tree with the flow velocity data from the PCA scans. This combination makes it possible to use flow data from areas of high accuracy to eliminate inaccuracies in other parts of the scanned volume. As a result, the reliability of the flow information at every location in the tree can be regarded as high as the reliability of the much fewer locations that would have been the result of a bipartite workflow.

## Keywords:

Phase Contrast Angiography (PCA); Quantitative Magnetic Resonance Angiography (QMRA); Flow analysis; Vessel segmentation; Centerline extraction; Abstract vessel tree model

## Acknowledgements

I want to thank the following persons for their help during the course of this Master's Thesis:

Thomas Seiler, Andreas Keil, Prof. Nassir Navab, Fritz Vollmer, Ralf Endreß, Sebastian Marsch, Daniel Thomann, Inma Rodriguez, Eva Wembacher, George OGREZeanu, Dr. Armin Huber, Ingmar Thiemann, Julia Reinhardt, Steffen Sammet, Dominik Wesp, Monika Lehmpfuhl, Dirk Staneker, Markus Neff, Swen Woerlein, Robert Schmidt und Alexander Dorner.

## Table of Contents

Abbreviations .....	III
Scientific Constants and Symbols .....	IV
Table of Figures .....	VII
List of Tables.....	VIII
<b>1 INTRODUCTION .....</b>	<b>1</b>
1.1 The Significance of Quantitative Flow Measurement in Diagnoses.....	1
1.2 Goal of this Thesis .....	3
<b>2 TECHNICAL LIMITATIONS OF PCA AND RESULTING CONSTRAINTS.....</b>	<b>7</b>
2.1 Technical Obstacles .....	7
2.2 PCA Data-Acquisition .....	8
<b>3 APPROACHES TO AN INCREASED DATA SIGNIFICANCE.....</b>	<b>13</b>
3.1 General Considerations .....	13
3.2 Vessel Segmentation from PCA-data .....	14
3.3 Conditioning Flow Data by Analysis of the Vessel Geometry.....	14
3.4 Deduction of a Corrective Factor for Flow Data Inaccuracies .....	16
<b>4 VESSEL SEGMENTATION .....</b>	<b>18</b>
4.1 Preprocessing .....	18
4.2 Segmentation Algorithm .....	22
4.3 Post-processing .....	30
4.4 Remarks about the Segmentation Result .....	32

---

<b>5</b>	<b>COMPILATION OF AN ABSTRACT MODEL OF THE VESSEL TREE.....</b>	<b>34</b>
5.1	Centerline Extraction .....	34
5.1.1	Definition and Methods .....	34
5.1.2	Detection of Centered Points by Means of Distance Transform Maps .....	37
5.1.2.1	Local Maxima of Distance Transform Maps as Centerline Nodes .....	37
5.1.2.2	Issues Concerning Maxima Ambiguity .....	39
5.1.2.3	Averaging Over Multiple Local Maxima by Gaussian Filtering.....	42
5.1.3	Detection of Centered Points by Means of Topological Thinning.....	46
5.1.4	A Combined Approach.....	48
5.1.4.1	Branch Creation.....	48
5.1.4.2	Branch Connection .....	51
5.2	Assignment of Volumetric Information to the Abstract Vessel Tree .....	56
<b>6</b>	<b>EVALUATION OF THE FLOW DATA BASED ON THE ABSTRACT MODEL.....</b>	<b>59</b>
6.1	Adding Flow Information to the Abstract Model .....	59
6.2	Processing of the Flow Data .....	63
6.3	Analysis of Flow Rate Changes Along a Selected Branch Section .....	68
6.4	Results of the Flow Rate Evaluation.....	70
<b>7</b>	<b>CONCLUSIONS.....</b>	<b>75</b>
	<b>APPENDIX A: ANATOMY OF THE CRANIAL VESSEL TREE .....</b>	<b>77</b>
	<b>APPENDIX B: MR FUNDAMENTALS .....</b>	<b>79</b>
	<b>APPENDIX C: ANNOTATIONS REGARDING THE SOFTWARE.....</b>	<b>91</b>
	<i>Bibliography</i> .....	94

## Abbreviations

CA	Contrast Agent
CE	Contrast Enhanced.
CFD	Computational Fluid Dynamics
cm	Centimeter
CPU	Central Processing Unit
CT	Computed Tomography
DICOM	Digital Imaging and Communications in Medicine
DTM	Distance Transform Map
ECG	Electrocardiogram
GHz	Gigahertz
ID	Identification (number)
ITK	Insight Segmentation and Registration Toolkit
MFC	Microsoft Foundation Class
mm	Millimeter
MR	Magnetic Resonance
MRA	Magnetic Resonance Angiography
MRI	Magnetic Resonance Imaging
MRT	Magnetic Resonance Tomography
PC	Phase Contrast
PCA	Phase Contrast Angiography
QMRA	Quantitative Magnetic Resonance Angiography
RAM	Random Access Memory
SE	Structuring Element
TOF	Time of Flight
VTK	Visualization Tool-Kit

## Scientific Constants and Symbols

$\bar{x}$	Mean of a set of variables X
$\bar{y}$	Mean of a set of variables Y
$2D$	Two-dimensional
$3D$	Three-dimensional
$A$	Area
$B$	Magnetic field strength
$d$	Metric size in Euclidian space
$dQ$	Differential change of flow rate
$ds$	Differential change in displacement
$dt$	Differential change in time
$dV$	Differential volume interchange
$E$	Energy
$e$	Encoding factor for velocity mapping
$E[]$	Expected value operator
$e_x$	Encoding factor for velocity mapping of a PCA scan with a magnetic gradient in z-direction
$e_y$	Encoding factor for velocity mapping of a PCA scan with a magnetic gradient in y-direction
$e_z$	Encoding factor for velocity mapping of a PCA scan with a magnetic gradient in z-direction
$h$	Planck constant
$\hbar$	Dirac constant
$I$	Electric current
$i$	Location of a voxel
$I_{max}$	Grey value in PCA scan representing a positive $v_{enc}$
$j$	Location of a centerline voxel
$k$	Boltzmann constant
$l$	Length
$M$	Angular momentum
$N$	number of voxels
$n$	Number of samples

---

$p$	Probability
$Q$	Flow rate
$r$	resolution in Voxel space
$R$	Radius
$r_{x,y}$	Pearson product-moment correlation coefficient
$s$	Nuclear spin
$S$	Intrinsic angular momentum of the nuclear spin
$T$	Temperature
$V$	Volume
$v_{enc}$	Velocity encoding
$X$	A Quantity of samples
$X(i)$	Function returning the scalar value at a voxel location I from a PCA scan with a magnetic gradient in x-direction
$Y$	A Quantity of samples
$Y(i)$	Function returning the scalar value at a voxel location I from a PCA scan with a magnetic gradient in y-direction
$Z(i)$	Function returning the scalar value at a voxel location I from a PCA scan with a magnetic gradient in z-direction
$\alpha$	Intersection angle
$\alpha_{min}$	Minimal angle of all intersection angles between a centerline segment and the gradients of the different PCA scans
$\gamma$	Gyromagnetic ratio
$\Delta E$	Energy difference
$\Delta m$	Magnetic gradient
$\Delta p$	Pressure gradient
$\Delta Q$	Discrete change in flow rate
$\Delta s$	Discrete displacement
$\Delta \Phi$	Phase shift
$\varepsilon$	Scalar value representing zero flow in a PCA scan
$\varepsilon_x$	Scalar value representing zero flow in a PCA scan with a magnetic gradient in x-direction
$\varepsilon_y$	Scalar value representing zero flow in a PCA scan with a magnetic gradient in y-direction

---

$\varepsilon_z$	Scalar value representing zero flow in a PCA scan with a magnetic gradient in z-direction
$\eta$	Viscosity
$\theta$	Scaling factor
$\mu$	Magnetic moment Mean value
$\nu$	Electromagnetic frequency
$\sigma$	Standard deviation
$\sigma(x, y)$	Covariance of the quantities x and y
$\omega$	Rotational frequency

## Table of Figures

Figure 1:	Two step QMRA approach .....	3
Figure 2:	Multi -directional PCA scanning .....	9
Figure 3:	Basic principle of a PCA volume scan in three directions .....	10
Figure 4:	Heart beat triggered PC volume tomography .....	12
Figure 5:	The knowledge of vessel tree geometry allows for calculation of intersection angles between vessels and field gradients. ....	15
Figure 6:	Replacement of unreliable flow data through arithmetic calculation (+/-) from more reliable segments .....	16
Figure 7:	Axial view of the PCA volume with sagittal gradient from the Ohio-data .....	20
Figure 8:	Paraboloid flow velocity profile in a tubular structure [40].....	24
Figure 9:	Velocity profile (in percent of $v_{enc}$ ) through the arteria cerebri media taken from the sagittal scan of the Ohio data .....	25
Figure 10:	Growing progress illustrated by a region of $3 \times 7 \times 7$ voxels .....	27
Figure 11:	Final segmentation result .....	28
Figure 12:	Over-segmentation caused by seed points outside the vessel volume .....	29
Figure 13:	Prevention of over-segmentation by eliminating seeds outside the vessel volume.....	29
Figure 14:	Morphological operations.....	31
Figure 15:	Closing as an example for a morphological operation.....	31
Figure 16:	Incorrect ostensible recombination of the arteria posterior cerebri and the arteria superior cerebelli in the closing result.....	32
Figure 17:	Vessels wrongly segmented as connected due to limited special resolution .....	33
Figure 18:	2D-Distance mapping.....	36
Figure 19:	Local maxima of a distance transform map .....	38
Figure 20:	Approach to reduce effort concerning the search for closest neighbors .....	39
Figure 21:	Effect of a loss of radial symmetry on DTM maxima .....	40
Figure 22:	Minimal spanning tree between DTM maxima with undesired bifurcation at the blue node .....	40
Figure 23:	Zigzagging of the centerline caused by maxima multiplets .....	41
Figure 24:	Centerline meanders caused by ambiguous local maxima .....	41
Figure 25:	$3 \times 3$ - and $5 \times 5$ - kernel for a Gaussian filtering operation [12, p.29].....	42
Figure 26:	Averaging over accumulations of local maxima in DTMs by Gaussian filtering .....	43
Figure 27:	Averaging over local maxima by applying Gaussian filtering .....	44
Figure 28:	Elimination of meanders by means of Gaussian filtering.....	44
Figure 29:	Loss of connectivity in thin, curved vessels as a result of Gaussian filtering .....	45
Figure 30:	Result of topological thinning with a close up of the right sinus transversus .....	47
Figure 31:	Connection of local maxima of a Gaussian filtered DTM by centerline points gained from topological thinning .....	50
Figure 32:	Vessels with stub branching off .....	51

Figure 33: Distinction between isolated local maxima within processed vessels and within stubs...	52
Figure 34: Unprocessed centerline points connected to a minimal spanning tree (blue) and existing centerline segments (green) .....	54
Figure 35: Result of branch connection over centerline points from topological thinning. ....	55
Figure 36: Assignment of branch voxels to their corresponding centerline edge .....	57
Figure 37: Voxel assignment to segments with closest centerline.....	58
Figure 38: Rendering of flow velocity vectors.....	61
Figure 39: Visualization of flow quantities - left: flow rates; right, top: flow velocities; right, bottom: sagittal component of the flow velocity .....	64
Figure 40: Flow rates along a section of the sinus rectus .....	67
Figure 41: Location of six branch sections selected for flow evaluation.....	71
Figure 42: Flow rates and minimal intersection angles of the six sampled branch sections displayed in Figure 41.....	72
Figure 43: Changes in flow rates and change of the minimal intersection angles of the samples 2 and 5 from Figure 41 .....	73
Figure 44: The major cranial veins.....	77
Figure 45: The major cranial arteries (as far as visible in the Ohio data) .....	78
Figure 46: Precession of a proton along the direction of the external magnetic field.....	81
Figure 47: Classical interpretation of the longitudinal magnetic moment .....	84
Figure 48: Induction of a phase shift by applying an external magnetic gradient.....	86
Figure 49: Applying a bipolar gradient improves phase contrast towards stationary tissue .....	87
Figure 50: Velocity aliasing caused by exceeded $v_{enc}$ .....	89
Figure 51: Velocity artifact in the sinus rectus as it can be found in the axial scan of the Ohio-data. ....	89
Figure 52: Application flow .....	92

## List of Tables

Table 1: Relaxation times of different tissues.....	85
-----------------------------------------------------	----

# 1 INTRODUCTION

## 1.1 The Significance of Quantitative Flow Measurement in Diagnoses

That a smooth blood circulation is essential for the well-being of the organism seems evident. Just as well it is obvious that the knowledge about disturbances of the circulation is of significant value for the diagnoses and treatment of many cardiovascular diseases. Hence, P.R. Moran stated in 1983, when the first operating experiences with quantitative magnetic resonance (MR) techniques had been made:

*“...the flow of fluids in a human subject is a most important phenomena, and its measure and imaging would provide diagnostic medicine with invaluable information for functional assessment and physiological status.”* [20, p.199]

G. Krestin for example states that a disturbed blood flow in the arteries supplying the kidneys is the cause for the renal insufficiency of 15% of all patients on dialysis [14, p. 7]. Numerous other examples for the significance of flow quantification in human medicine can be found in [14], [19], [20] and [36].

Thus, it does not come as a surprise that Doppler sonography<sup>1</sup>, which is capable of quantifying flow velocities in sonographed vessels, has become one of the most important diagnostic imaging techniques since it was first applied in the 1950s [12, II/ p.25]. However, it might surprise that among all none-invasive methods<sup>2</sup>, so far only Doppler sonography has become a truly established technique concerning quantitative flow analysis [36, p. 698], despite many valuable approaches based on Magnetic Resonance Tomography (MRT) having been developed since<sup>3</sup>. Of course, these new

---

<sup>1</sup> Doppler sonography quantifies the velocity of flowing liquids by measuring the Doppler effect ultrasound pulses experience when reflected by these moving liquids. See [44] for detailed explanation.

<sup>2</sup> In areas not examinable by sonographic methods (like the cranial vessels) some invasive techniques, usually involving the administration of contrast agents, have become the gold standard, but since these are all invasive approaches, this thesis will not deal with such techniques.

<sup>3</sup> Other approaches like those based on conventional X-Ray or Computed tomography usually only supply insights into anatomical aberrances but no quantitative information.

approaches have some drawbacks, which will be addressed in the course of this thesis, but sonography has some significant limitations either, like

- very limited penetration depth and a trade-off between resolution and penetration depth
- the deficiency in the penetration of bone, which e.g. limits sonography of the brain
- similar difficulties arise with gas between the transducer and the region of interest
- since the transducer is usually not tracked during image acquisition, it is sometimes difficult or even impossible to tell afterwards, where the recorded area is exactly located in the body, especially if the recorded region is very small

The mentioned MR-techniques (which are explained in appendix B) do not hold these limitations and should thus be expected to be in common use for many indications. Vassol Inc. [41], Heiland [8] and Hemmingsson [9] point out that quantitative magnetic resonance angiography (QMRA) can provide excellent results for many applications.

Until today, however, these techniques are not widely-used. This is not caused by lower reliability of QMRA results as the reliability has been proven in many experiments like in vivo ultrasound experiments (as performed by [26], [17]) as well as ex vivo experiments with defined artificial flow (compare [33]). Hemmingsson even sees magnetic resonance imaging (MRI) superior to ultrasound in some fields:

*“MRI of the carotids seems to be superior to ultrasound in the diagnosis of occlusion of the vessels and the technique can be used as a screening test for carotid artery stenosis.”* [9, p. 3]

Lotz et al. see the reason for this (apart from *“the high availability of Doppler flow units”*) in higher acquisition times as well as in the need for post processing of MR-Data. [17, p. 652]

Many difficulties concerning QMRA, however, remain, which still limit its use, despite all its advantages. Eliminating these drawbacks could vastly increase the application range. Hence, it will be the ambition of this thesis to address the most pressing of these matters by means of intelligent data processing.

## 1.2 Goal of this Thesis

For reasons explained in appendix B.3 of all quantitative MR techniques only a method called Phase Contrast Angiography (PCA)<sup>4</sup> is suitable for the evaluations which are subject of this thesis. Most PCA examinations are so far restricted to very small regions of interest (ROI) containing a few vessels only [9, p.658]. This is mainly caused by the fact that this technique is, for reasons to be explained in the chapters 2.2 and 2.3, a time consuming and thus costly task, bearing some significant technical limitations.

If a constriction to a small region is not feasible, a bipartite workflow requiring two MR imaging sessions is often engaged so far as for example in [36] and [41]. The first step consists of a MR-scan (or any other suitable medical imaging technique) providing data suitable for vessel segmentation (e.g. Time of Flight (TOF) or angiography by means of computed tomography (CT) with contrast agent)<sup>5</sup>. Based on this data, a second scan can be planned, taking the technical limitations of phase contrast into account:

*“This 3D structure is used to identify and facilitate perpendicular cuts during scanning...”* [36, p. 698]

Figure 1 taken from [41] illustrates this approach.

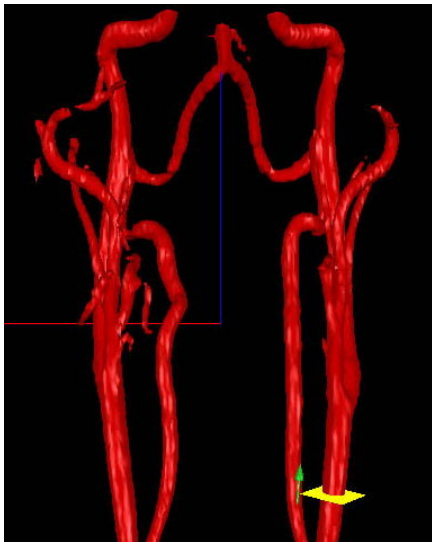


**Figure 1: Two step QMRA approach**

After segmentation of a conventional angio scan, the attending physician can define planes (yellow) through which blood flow will be measured during a later scan.

---

<sup>4</sup> Or more generally just “phase contrast” (PC).

<sup>5</sup> These techniques are explained in appendix B.3.

If there are only a few vessels in the ROI, for which flow information is of interest, this information can be gained by defining at least one slice intersecting all these vessels perpendicularly.

Even less PCA slices are needed all together, if only the flow velocities in vessels entering and leaving the ROI are measured and the flow in between is determined by flow simulation [42]. There is a whole interdisciplinary field in science called Computational fluid dynamics (CFD), which only deals with such mathematical and computationally complex flow simulations.

Nonetheless, both approaches require a preceding anatomical scan. On the basis of this anatomical scan the attending physician has to plan the position and orientation of the PCA slices in the second scan, in order to determine flow velocities in these vessels (compare Figure 1). This planning step is required even if the number of vessels in question is comparably limited, making the described techniques either very time consuming (since the patient has to come back for a second scan) or requires the attending physician to be present throughout the scans. The considerable time period between both scans additionally demands either accurate patient registration or (often multimodal) image registration<sup>6</sup> during post processing. In the case of flow simulation, the results can still not be considered completely reliable [24, p.1], which leaves an element of uncertainty on this method often not acceptable for medical purposes. Therefore it is inefficient to perform an anatomical scan for vessel segmentation first and a quantitative scan of the same region later – based on the results of the first scan.

Finally it has to be considered that a single PCA slice sample through a vessel allows strictly speaking only conclusions about the flow through solely the sampled plane. This limitation can have at least two negative effects.

---

<sup>6</sup> The term „patient registration“ means that the position and orientation of the ROI relative to the scanner has to be well determined during every scan in order to integrate the different scanning results later. This is particularly challenging for non rigid body parts like the abdomen. The term „image registration“ refers to a technique where corresponding features in both scans are used to integrate the scanning results after acquisition. If the two datasets to register have been produced by different scanning techniques (like contrast agent CT in the first and PCA in the second scan) such a registration is called multimodal.

First, there always remains the risk that small feeding or draining vessels in the vicinity of the sampled slice are not depicted due to the limited resolution of any tomographic imaging technique. This makes any assumptions about the flow immediately in front or behind the selected plane speculative.

Secondly, locally confined phenomena like turbulent flow can result in measuring too low flow velocities in the selected plane.

For these reasons, in order to reach acceptable reliability, at least a few additional PCA samples are advisable for such two-step-approaches.

Furthermore, it is not always feasible to determine in advance, which vessels need to be examined to get the necessary information to make a diagnosis, which again increases the number of slices to define for scanning.

Planning all these planes and setting them up for the second, quantitative scan involves a considerable amount of time and effort. For this reason it seems advisable to perform a quantitative scan of the whole ROI instead. This would also allow limiting data acquisition to only one scanning session. In addition it would, in contrast to the method of pre-planned slices, present valuable flow information throughout the whole region of interest. Yet, such a PCA volume scan is very intricate and would, for reasons explained in chapter 2, not yield the same optimal accuracy in every part of the scan as the two-step approach can provide it for the pre-planned slices<sup>7</sup>. This could result in comparably low accuracies in just those areas which represent the areas of interest.

Hence, the goal of this thesis is to provide a workflow limiting the quantitative flow evaluation within a vessel tree<sup>8</sup> in any rigid ROI to only one scanning-session as well as to provide the software capable to process the thus acquired data. It devises methods to compensate for the locally unequal reliability of the PCA volume scan data concerning both, accuracy and validity. As a result precise flow data throughout the whole region of

---

<sup>7</sup> To eliminate these inaccuracies, the PCA volume scans would have to be performed with unacceptable effort.

<sup>8</sup> Although the test-data used in this thesis is cranial, there should only very little if any changes are necessary in order to process similar data from other organs like the kidneys as well. Less rigid organs like the lungs would make additional preprocessing steps necessary, which are not provided by the software developed in the course of this thesis.

interest and not only for some selected slices are provided. This leads to an overall increased reliability and significance of the final result, compared to the described bipartite approaches. Hence, quantitative MR angiography will become faster (and thus cheaper) as well as easier to validate and more reliable.

The thesis will deal with cranial vessels only but results should be adaptable to other organs like liver and kidneys or the limbs [41].

## 2 TECHNICAL LIMITATIONS OF PCA AND RESULTING CONSTRAINTS

### 2.1 Technical Obstacles

Not until the problems inherent to all MR techniques for quantitative flow analysis as they were mentioned in the previous section have been explained, the reader can understand the difficulties linked to quantitative flow analysis by means of MR techniques.

It is not necessary for the reader to understand the causes of these limitations in order to understand the problems arising thereof, but for a deeper understanding the relevant details of MR are explained in appendix B. The reader should just be informed that PCA has two significant limitations<sup>9</sup>.

The first limitation is that the range of flow velocities that can be measured with adequate resolution is limited. In order to get sound results the maximum of the flow velocities to be expected in the ROI must be estimated in advance and taken into account during data acquisition [14, p.6]. This highest expected velocity is called velocity encoding ( $v_{\text{enc}}$ ) and has to be set as a PC scan parameter. If flow velocities are estimated too high (i.e.  $v_{\text{enc}}$  was selected higher than necessary), intense noise [26, p. 809], poor velocity contrast and even a loss of signal can be the result [9, p.2]. If the flow velocities are underestimated, however, so-called velocity artifacts are the result, where velocities higher than  $v_{\text{enc}}$  are wrongly interpreted as low velocities in the opposite direction (compare B.2)<sup>10</sup>. These limitations are especially problematic if vessels with very variate flow velocities (like the coronal arteries) are contained in the

---

<sup>9</sup> Strictly speaking, there is even a third limitation common to all MR techniques, which is a low spatial resolution compared to other, invasive techniques like digital subtraction angiography [20]. But since this is a technical problem, which cannot be addressed by software solutions, it will not be subject of this thesis.

<sup>10</sup> The effect, usually called “velocity aliasing”, is comparable to a spinning cartwheel in a movie, which seems to turn backwards because the frame rate of the camera is too low to correctly reflect the position shift of the spokes.

(ROI). Yet, suitable velocity encoding can be usually found by trial and error within a few minutes.<sup>11</sup>

The second, more severe limitation is the sensitivity of PCA towards flow directions. The technique is only capable to accurately measure flow velocities within a very limited directional range<sup>12</sup>. According to Lotz et al. [17, p. 658] a deviation of more than 15° already leads to imprecise results. Hence, several PCA scans have to be performed in order to examine vessels with strongly deviating orientations as will be explained in the next section.

## 2.2 PCA Data-Acquisition

Although there has always a trade-off to be found between acquisition effort and the quality of the resulting flow information, PCA volume scans are a sophisticated task even for the most limited pretensions.

The first indispensable pretension concerns the number of complete volume scans that need to be performed. As mentioned, PCA scans are sensitive to the flow direction and thus only capable to detect flow in roughly one selected orientation. Technically, this orientation is determined by the orientation of a gradient superimposed on the scanner's magnetic field. The planes in Figure 2 are areas of homogenous magnetic field strength. The same is true for any plane parallel to these planes, since these might pose either a stronger or weaker magnetic field but are of homogenous strength. As a result, the magnetic field gradient vector is perpendicular to these planes. For reasons to be explained in appendix B.2, any vessel has to be roughly perpendicular to these planes (i.e. parallel to the gradient) in order to determine its flow. Therefore the orientation for which the scan is most reliable is identical to the orientation of the magnetic gradient.

---

<sup>11</sup> If high velocity resolution is essential, several scans with different  $v_{enc}$ , so called Multi-Venc-Sequences, have to be performed on the same ROI [20, p. 679].

<sup>12</sup> See appendix B.2 for a detailed explanation of this phenomenon.

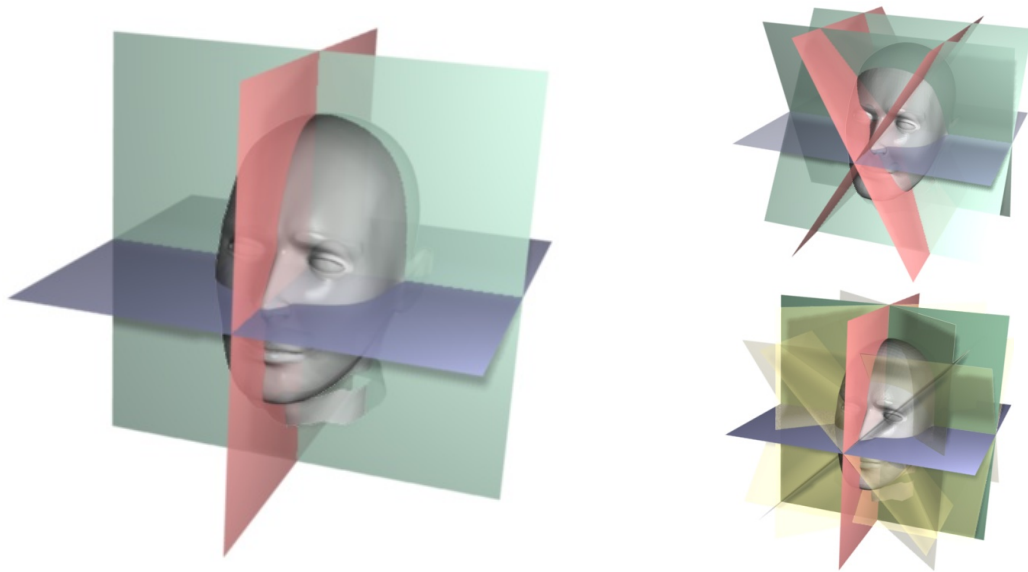


**Figure 2: Multi -directional PCA scanning**

**left: Due to the directional sensitivity of PCA, at least three different orientations for the field gradient are required to measure flow velocities in a three dimensional vessel tree right, top and bottom: the more orientations available, the higher the amount of vessels for which flow information can be considered reliable.**

Since velocities measured in vessels with an orientation deviating too much from this orientation of the gradient have to be considered unreliable, multiple scans have to be performed with different flow orientations to be examined each time. Three directions can be considered the absolute minimum for most volumetric flow determination tasks<sup>13</sup> [8, p. 678], but the more directions, the larger is the number of vessels for which the flow data can be considered reliable.

Commonly used anatomical terms exist for the three basic plane orientations shown in the left part of Figure 2. The orientation of the red plane in the figure is called “sagittal”, the blue one has an “axial” orientation and the so called “coronal” plane is colored green. Planes perpendicular to only one of these anatomical planes (as shown on the right side of Figure 2) are called “oblique”, those perpendicular to none of these are called “double oblique”.

---

<sup>13</sup> Actually one more scan has always to be performed as will be explained in appendix B.2.

Yet, when talking about PCA volumes, these anatomical terms can refer to an orientation other than the orientation of the planes of homogenous magnetic field strength (often called “read out planes”). Since it is common to view volumetric scan data in the form of two dimensional slices, these slices have an orientation with regard to the whole image volume as well. Giving solely an orientation to describe the modality of a depicted image would thus be mistakable, since it would not be clear whether the word “axial” for example refers to an axial read-out plane or whether a slice through the data volume with axial orientation is displayed. But since flow is usually the subject of interest throughout this thesis, the term “axial scan” will hence refer to a „scan with axial read out plane“ if not explicitly expressed otherwise.<sup>14</sup>

A single PCA scan, however, can only be performed on one of these planes at a time, which is called the “read-out plane”. Therefore a scan over a whole volume has to consist of several of these read-out planes (Figure 3).

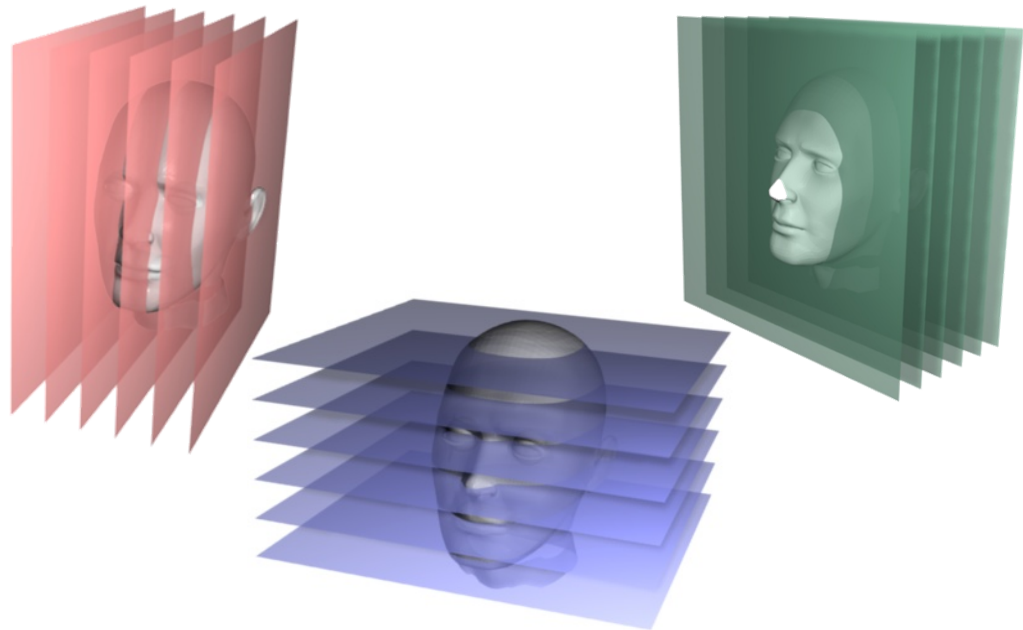


**Figure 3: Basic principle of a PCA volume scan in three directions**  
**left: sagittal scan, middle: axial scan, right: coronal scan**

---

<sup>14</sup> When referring to PCA data acquisition, the words “plane“ and “slice” can be used synonymously sometimes, since the result of a scan with a given read-out plane is an image slice with the same position and orientation.

As mentioned in section 1.1, volumetric QMRA is (especially in Germany<sup>15</sup>) hardly in clinical use so far and therefore most institutions operating MR scanners do not perform scans as they are needed for the new approach this thesis pursues. Only one institute, the Ohio State University Medical Center could be resurrected to provide a cranial PCA volume scan. It was performed on a new ultra high field MR-scanner with a field strength of eight Tesla manufactured by Philips Medical Systems. The data (which will be referred to as “Ohio-Data” in the following) consists of a set of three volume scans with the three gradient orientations given in Figure 2.

As Heiland et al. point out, pulsatile flow can cause problems in artery flow since “*signal intensity depends on the phase of the heart beat cycle in which the data was acquired*” [8, p. 679] and proposes ECG triggering<sup>16</sup>.

ECG triggering causes data acquisition to be more time consuming<sup>17</sup>, since the triggering has to be carried for each image slice but it usually has to be done to ensure that all slices of a set are recorded at the same phase of the heart beat cycle.

Triggering can be used in two ways. For the first method each slice position is depicted only once. This is feasible if only flow rates during a defined phase of the heart cycle are of interest, for example to determine maximum flow. This is sufficient to determine the impact of shunts<sup>18</sup> for instance. For a dynamical recording of pulsatile flow through the vessels, the second method is engaged. For this technique, called cine-mode MRI, several images are recorded during different defined phases of the heart beat at each slice.

---

<sup>15</sup> Nearly all recent publications concerning QMRA originate from the USA.

<sup>16</sup> An electro cardio graph (ECG) is used to trigger the recording of all slices, allowing to synchronize the scan with the pulse of the patient.

<sup>17</sup> How much the acquisition time is prolonged by ECG-triggering depends on the scan modalities. In [10, p.21] for example scanning time was prolonged by the factor 3.

<sup>18</sup> A shunt is an abnormal bypass, for example a vessel allowing arterial blood to directly passage into a vein.

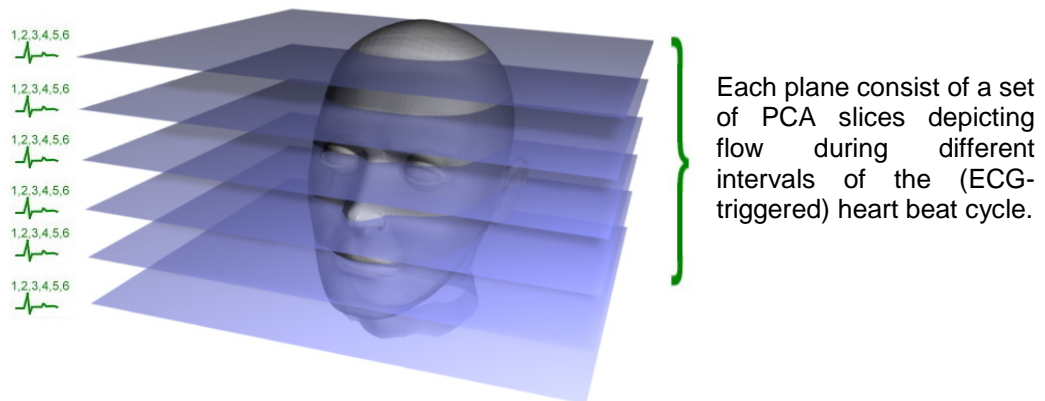


**Figure 4: Heart beat triggered PC volume tomography**

J. B. Park et al. [24] propose a time-averaged velocity measurement which uses ECG triggering only to determine the start and end of a pulsatile cycle. The technique makes averaging obsolete, but poses almost no time saving.

Unfortunately, the Ohio-scans were performed without any ECG triggering or other means of pulsatile averaging, a fact that will have some major impacts on the evaluations throughout this thesis as will be explained in section 6.4.

## 3 APPROACHES TO AN INCREASED DATA SIGNIFICANCE

### 3.1 General Considerations

The previous chapter has shown that in principle, both of the inherent limitations to the accuracy of PCA volume scans (as explained in section 2.1) can be arbitrarily reduced by increasing the number of scans. As pointed out already, the more different gradient orientations are used during data acquisition, the higher the chance that all vessels of interest are scanned with an optimal gradient orientation. Thus it would theoretically suffice to perform the quantitative scans with dozens of different gradients to ensure the vessels of interest are scanned with a quality equal to that of preplanned slices. Since such an optimal data foundation would, however, involve hours of scanning time<sup>19</sup> and require the patient to remain in the same position throughout this period it is not practical to solely rely on PCA data when it comes to the examination of whole vessel trees<sup>20</sup>. To limit the effort for data acquisition to a reasonable amount there have concessions to be made, especially concerning the number of PCA volume scans with different orientations.

Hence, three approaches to reduce scanning effort, or in other words to significantly increase the reliability of data acquired with a reasonable effort, will be evaluated in this thesis.

---

<sup>19</sup> A PCA volume scan with only three gradients performed on the author's head in a 3-Tesla MRI scanner at the university hospital of Heidelberg took some 40 minutes. Unfortunately the data was unusable due to faulty scanning parameters and the scan could not be repeated.

<sup>20</sup> Applications of quantitative MR techniques are until today often limited to the examination of very small and well defined regions. In general these regions are confined to only a single image slice like a plane through the cardiac valves.

## 3.2 Vessel Segmentation from PCA-data

Although this approach does not increase the reliability of the acquired PCA data, a reduction in scanning effort by eliminating the need for a separate anatomical scan reduces overall scanning time and thus allows utilizing more scanning time on the quantitative scans without increasing costs.

This first approach makes it necessary to find a segmentation technique capable to deal with the PCA-data. Segmentation had otherwise merely to be performed on a volume scanned with a modality specially devised for such a task. This task will be the subject of chapter 4.

## 3.3 Conditioning Flow Data by Analysis of the Vessel Geometry

This second approach by far amounts to the largest part of this thesis as well as most of the software implementation concerning this work. The idea is to use information gathered about the structure of the vessel tree to limit the amount of flow data needed or in other words to deduce flow information about areas with unreliable or even missing flow data from information about the geometry of the vessel tree. Chapter 5 will deal with the task of generating an abstract model of the vessel tree on the basis of the segmentation devised in chapter 4. The thus created abstract representation of the vessel tree can be utilized as described in this chapter.

As explained in section 2.1, flow data of some vessel segments cannot be, due to the angular sensitivity of PCA, considered reliable. But instead of restricting the flow analysis to a few selected vessels, the whole volume is examined and the most suitable (i.e. reliable) vessel segments are selected from this volume. Figure 5 explains how the knowledge about the topology of the vessel tree can be utilized to determine these most reliable segments.

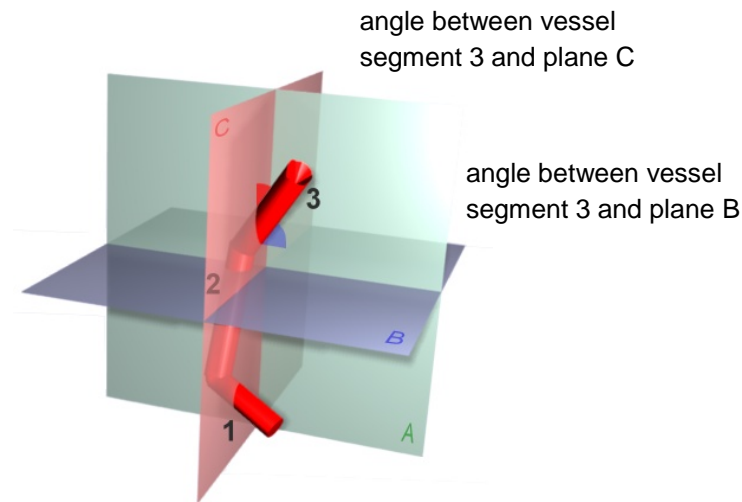


**Figure 5: The knowledge of vessel tree geometry allows for calculation of intersection angles between vessels and field gradients.**

Flow volumes of the remaining vessels with a less suitable orientation will be determined using the abstract vessel representation. With the flow information of the “reliable branches” the flow rates for the whole vessel tree are calculated by combining these reliable values.

Figure 6 illustrates this approach: with a sufficient amount of vessel segments roughly parallel<sup>21</sup> to the field gradient (and thus considerable as “reliable”) it would be possible – in combination with the abstract model of the vessel tree - to computationally replace less reliable<sup>22</sup> segment’s flow data.

---

<sup>21</sup> As mentioned before, the angle should preferably be smaller than 15°.

<sup>22</sup> I.e. the flow data of segments, which are badly aligned with regard to all gradients.



In order to understand the different issues concerned with the angular sensitivity of PCA it is necessary to distinguish between contrast and data accuracy. While the flowing blood remains well visible even for comparably large angles, the quantitative accordance between scan values and actual velocities is unsatisfactory for angles larger than the  $15^\circ$  mentioned in section 2.1. On the other hand, the maximal angle until a signal vanishes in the background noise is much higher. It depends on  $v_{enc}$  and the flow velocity in the vessel [29, p.1], but an angle of roughly  $60^\circ$  seems to pose the upper limit for most vessels in the Ohio-data.

First the flow data for some of the branch segments rated as unreliable are adjusted as described in the previous section. The difference between measured and calculated flow values can then be determined. If a correlation between the degree of angular misalignment and the difference between original and adjusted flow data values can be derived, a corrective function might be found. It is not to be expected, that the only PCA-volume scan available for this thesis provides enough data to statistically prove the transferability of such a function to other scans, or even to completely rely on such a function as an alternative to the previous approach once it has been set up. But it might pose a means to prove the reliability of the approach proposed in section 3.3 or even to give strong evidence, whether the flow in a certain vessel segment might be underestimated, due to poor angular alignment.

## 4 VESSEL SEGMENTATION

### 4.1 Preprocessing

As can be gathered from Figure 52 in appendix C, an Insight Segmentation and Registration Toolkit<sup>23</sup> (ITK) library function is used to read the original PCA data. Medical imaging data is usually stored in accordance to the DICOM standard.

Apart from other functions the DICOM standard, defines the way in which the scanning results are stored<sup>24</sup>. Usually a DICOM-file consists of several tags containing information about the patient as well as the scanning modalities and parameters. There are so far only two DICOM-conform ways to store volumetric data, single frame storage and multi frame storage. In single frame storage, each slice is stored in a separate file with nearly all further DICOM information stored redundantly in every file. By contrast all slices belonging to a volume scan are stored subsequently within a single file in multi frame storage mode.

Since the Ohio data however uses a special, proprietary format from Philips, no library or public source code was available to read this format at the time this thesis was devised. Even few month old image viewers issued by Philips, were not able to properly open the data and for this reason, an initial data processing step became necessary.

Until recent it was common to store each image slice in the DICOM standard in single frame format. To speed up data transfer, however, multi-frame format images are advancing since a few years. Yet, these multi-frame data sets were so far only used to store one single volume scan with (apart from slice positions) identical modalities. Philips has, however, devised a new, DICOM based way to store scan data, which could be best called multi-volume images. Since these volumes do not even necessarily represent the same scanning technique, some of the information concerning scan

---

<sup>23</sup> See appendix C for explanations about ITK.

<sup>24</sup> See [32] for detailed information about the DICOM standard.

modalities are not stored in the DICOM file tags of the file as usual, since some entries (like gradient directions) would not apply to all volumes.

For this reason Philips stores some necessary information in additional files in a proprietary format and therefore (among others) the information which dataset belongs to which gradient and even which image belongs to which volume cannot be gathered from the DICOM headers.

This unorthodox way of storing scan information prevented the ITK-library-function mentioned before from reading the data properly. For this reason the datasets had to be decomposed into single-frame images, before they could be read and processed by the QMRA software.<sup>25</sup>

Apart from these specific provisions concerning the characteristics of the Ohio-data, the special properties of PCA images make preprocessing of the data foundation necessary.

As explained in section 3.4, PCA provides very good contrast between blood and stationary tissue as long as the flow direction is almost parallel to the field gradient. It is, however, uncommon that all vessels in a ROI are parallel to each other and can thus not all be parallel to the same gradient. Therefore a single PCA scan is not suitable for vessel segmentation.

As can be gathered from Figure 7, the vessels in a sagittal scan are only well visible (as white or black stripes) as long as they run roughly in lateral direction (from right to left or from left to right) and thus parallel to the magnetic field gradient.

---

<sup>25</sup> Actually only one of all examined tools, “Dicom2” (<http://barre.nom.fr/medical/dicom2>) by Sébastien Barré, proved capable to perform this task. Therefore this freeware tool can be found on the DVD included with this thesis.

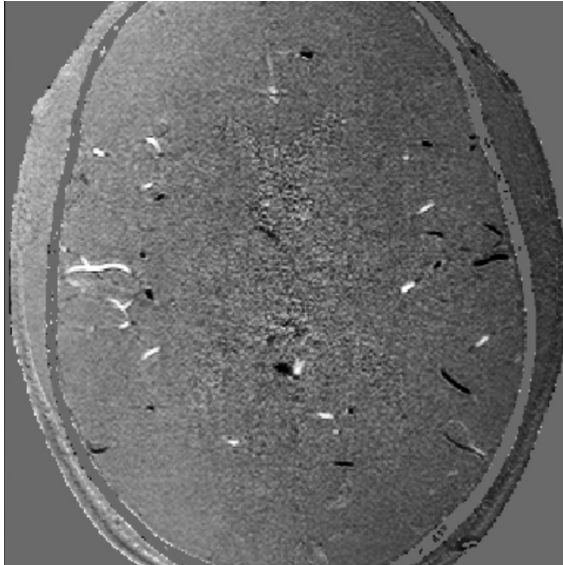


**Figure 7: Axial view of the PCA volume with sagittal gradient from the Ohio-data**

As soon as the orientation of the vessels differs too much from the gradient direction, they are not captured by the sagittal scan anymore<sup>26</sup>. It is evident that such a discontinuous depiction is not practical for segmentation. The common solution is to perform an additional scan using a different technique with good contrast between blood and stationary tissue in all directions (like contrast enhanced MRA, which is described in appendix B.3).

Since it is, however, one of the objectives of this thesis to investigate, whether sufficient segmentation results can be accomplished from the sole PCA scans, the three PCA scans are combined in a way appropriate to overcome the directional confinement of PCA. A combination of merely three volume scans is sufficient, because PCA still poses good vessel/tissue-contrast even for angles over  $45^\circ$ <sup>27</sup>.

The maximal angle until a signal vanishes in the background noise depends on  $v_{enc}$  and the flow velocity in the vessel, but an angle of roughly  $60^\circ$  seems to pose the upper limit

---

<sup>26</sup> A closer look at the data reveals that the coherence of vessel direction and scan direction is not that strict: due to turbulent flow the velocity vector of the blood often has a component not parallel to the vessel itself and thus vessels are sometimes well visible even if they run nearly perpendicular to the field gradient.

<sup>27</sup> As explained in chapter 3.4, a sound contrast in PCA images is not synonymous with reliable flow velocity information.

for most vessels in the Ohio-data. Thus, every vessel section should be visible in at least one scan if at least three scans with different perpendicular gradients are performed.

Several operations can be used to combine these scans, as long as it is assured that a vessel segment visible in one of the scan volumes remains visible in the combined data. Out of these operations four of the most common have been implemented in the software developed in the course of this thesis:

1) Thresholding with subsequent OR

A thresholding is performed so that the binary value 0 is assigned to every voxel which has a value<sup>28</sup> lower than a given threshold<sup>29</sup> and the value 1 to every other voxel. Afterwards an OR operation is performed among all thresholded datasets. The advantage of this way of combining the data is that the outcome is segmented data already. The disadvantage is, however, that a suitable threshold has to be set by the user and that mere thresholding usually does not lead to optimal segmentation results.

2) Quadratic sum of scalar values

All scalar values are squared before they are summed up with the values of the other datasets. This method is fast and poses good contrast between blood and background noise.

3) Square root of quadratic sum

This method is identical to method 3) but the square root is extracted in an additional step. The advantage of this proceeding will be explained in the next section.

---

<sup>28</sup> If the PCA data is stored as signed value, the absolute value has to be used; if the data is stored as unsigned values (like the Ohio-data), the difference of each value to the value representing zero flow has to be used instead.

<sup>29</sup> An upper value is not necessary for PCA data, since in contrast to TOF all values above the lower threshold can be considered to belong to dynamic tissue, i.e. blood.

## 4.2 Segmentation Algorithm

The most common segmentation approach for any dataset not suitable for pure thresholding are so called “region growing” techniques. Region growing is a method in image processing, where, starting from one or more seed points, adjacent points of such a seed are tested if they meet a certain growing criterion. If they do, they are merged to the region and serve as new seeds for the next growing step. Otherwise they are abandoned. Yet, in contrast to conventional region growing algorithms, the growing criterion has to be adaptive for the segmentation of MRA images as Eiho, Sekiguchi et al. emphasize:

*“As the range of the blood vessel intensity in MRA is widely spread, conventional binarizing method is unable to extract blood vessel region. The same is true for region growing, because the growing condition is also determined from the range of the intensity value. To overcome this problem, it is obvious that the growing condition has to be changed adaptively according to the local vessel intensity.”* [4, p.1]

It was originally intended to use this segmentation algorithm developed by Eiho, Sekiguchi et al. [4] and implemented as an ITK-filter by Florian Maier. Pascal Bertram, had already successfully adapted and used this filter as presented in [2], which deals with vessel segmentation from CT images.

The distinctive feature of the “branch based region growing algorithm” towards most other region growing algorithms is that it does not grow arbitrarily into every branch encountered during the segmentation process, but it tries to detect bifurcations and grows into only one branch at a time. This allows some improvements compared to most other region growing algorithms especially concerning leaking<sup>30</sup>.

The growing behavior within each branch is controlled by an adaptive Thresholding. The algorithm calculates the mean value  $\mu$  and the standard deviation  $\sigma$  of the current branch region’s intensities. From this a dynamic lower threshold ( $th_{dyn}$ ) is set individually for each branch.

---

<sup>30</sup> In the context of region growing, the term leaking describes the common but undesired effect that parts of the processed image data become part of the segmentation result, which are at the bounds of the image structure targeted by the segmentation but do not belong to it.

$$th_{dyn} = \max(\mu - h \cdot \sigma, th_{low}) \quad (4.1)$$

Equation 4.1 [18, p. 10] specifies the calculation of the dynamic threshold, where  $th_{low}$  is a predefined lower bound for the threshold. The multiplier  $h$  can be used to parameterize growing behavior, where a small  $h$  reduces the risk of leakage but causes small structures to remain unsegmented. The mean value  $\mu$  and the standard deviation  $\sigma$  are determined for each iteration step of the growing process. Only voxels with a value above this dynamic threshold are merged to the region and can serve as new seed points for the next growing step.

Afterwards the algorithm continues to grow into one of the postponed branches. When the growing process of a branch has come to an end, the branch region will not be added to the segmented region unless the criterion

$$\overline{\mu}_i \geq \begin{cases} c_{min} + k \cdot d_i, & d_i < d_c \\ c_{min} + k \cdot d_c, & otherwise \end{cases} \quad (4.2)$$

is fulfilled [4, p.3]. Thus a branch  $i$  will only be added to the final segmentation result, if  $i$  is a thin branch (i.e. thinner than  $d_c$ ) and its average intensity  $\overline{\mu}_i$  is higher than  $c_{min} + k \cdot d_i$  respectively higher than  $c_{min} + k \cdot d_c$ , if  $i$  is thicker than the threshold  $d_c$ .  $c_{min}$  is a predefined lower limit,  $k$  a multiplier used to parameterize the leak detection,  $d_i$  the average thickness of the branch and  $d_c$  an upper limit for the branch's average thickness. The idea behind criterion 4.2 is that Eiho, Sekiguchi et al. see a linear relation between vessel thickness and voxel intensities in MR angio images.

With regard to the good segmentation results for many different datasets as presented in [18], [4] and [2] the branch based region growing algorithm was used first in the search for a suitable segmentation method.

Unfortunately, segmentation results were dissatisfactory. Depending on the growing parameters, either only large vessels were segmented or the results showed excessive leaking. A look at the development of the dynamic threshold values  $th_{dyn}$  throughout the growing progress revealed that this was caused by the dynamic threshold only rarely exceeding  $th_{low}$ . One cause could be found in the high variance of the preprocessing

result emerging from the use of quadratic sum in the preprocessing<sup>31</sup>. Since the algorithm for determining the dynamical threshold uses the variance of the branches' values, the squared values cause variances too high to serve as a reasonable threshold parameter. As a result the region growing performed like a thresholding algorithm performed with  $th_{low}$ , when quadratic sum as described in section 4.1 was used as the operation for preprocessing. For this reason the square root of the quadratic sum (the fourth algorithm in 4.1) was used instead.

But nonetheless, the value of  $th_{dyn}$  quickly dropped to  $th_{low}$  after few segmentation steps. The reason for this behavior could be found in a still too high variance of the original data. Since flow velocities decrease quadratically from the center of a tube to its wall as can be gathered from the Hagen- Poiseuille-law [40]

$$v(r) = \frac{\Delta p}{4\eta \cdot l} \cdot (R^2 - r^2) \quad (4.3)$$

the original data posed high variances already.

Formula 4.3 gives the flow velocity  $v(r)$  for any radius  $r$  from the center of a tube with radius  $R$  and length  $l$  conducting a fluid with viscosity  $\eta$  for a given pressure gradient  $\Delta p$  between tube inlet and outlet. Although equation 4.3 applies only to laminar flow and can thus describe the velocity profile only for laminar flooded vessel segments, it should be kept in mind that flow velocities fall approximately exponentially from the center of a vessel to the vessel wall. Hence, the idealized flow profile of a current in a tube is a paraboloid as illustrated in Figure 8 with a flow profile posing the quadratic velocity distribution stated above.

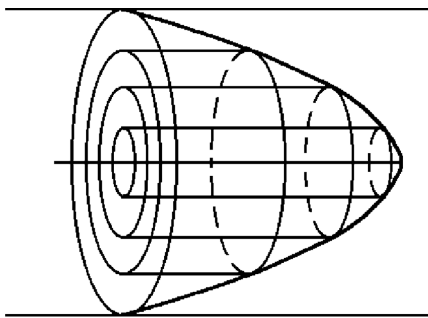


**Figure 8: Paraboloid flow velocity profile in a tubular structure [40]**

<sup>31</sup> Second one of the algorithms proposed in 4.1.

To prove the transferability of the theoretically predicted velocity profile to the Ohio-data, Figure 9 shows the velocity profile of the left arteria cerebri media<sup>32</sup> in the sagittal scan. The right part of the figure shows the velocity profile of the vessel, which exhibits a roughly quadratic velocity distribution as expected.

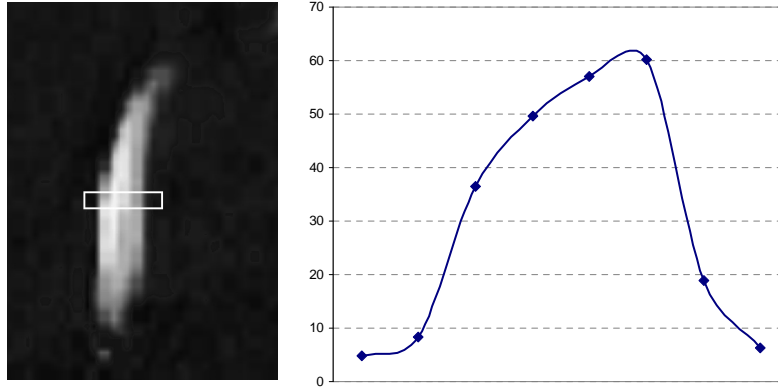


**Figure 9: Velocity profile (in percent of  $v_{enc}$ ) through the arteria cerebri media taken from the sagittal scan of the Ohio data**

Hence, while the branch-based region growing algorithm proved very useful for the datasets in [18], [4] and [2], it failed to produce acceptable results from the PCA data despite its fair contrast between vessels and stationary tissue.

An adjustment of the region growing algorithm as presented in the following, however, led to segmentation results suitable for the approaches introduced in chapter 3. The dynamic threshold criterion  $th_{dyn}$  (see equation 4.1) was replaced by a criterion which only takes the immediate neighborhood into account. A voxel  $v$  is only added to the region if its intensity  $\mu$  meets the criterion

$$\mu(v) > th_{low} \quad (4.4a)$$

or if the average intensity  $\bar{\mu}$  of its neighborhood<sup>33</sup>  $N(v)$  meets the criterion

$$\bar{\mu}(N(v)) > d \cdot th_{low} - \sigma(N(v)) \quad (4.4b)$$

<sup>32</sup> Refer to appendix A for an introduction to the cranial vessel anatomy.

<sup>33</sup> The neighborhood of a voxel is made up of all other voxels within a certain volume around this voxel.

where  $th_{low}$  is again a predefined lower threshold which can either be a fixed value or determined in a preprocessing step,  $d$  is a parameter to manipulate growing behavior and  $\sigma$  the standard deviation.

Most suitable proved the parameterization of the neighborhood by a volume of three pixels in all three directions of the coordinate system (in the following called 3×3-neighborhood).

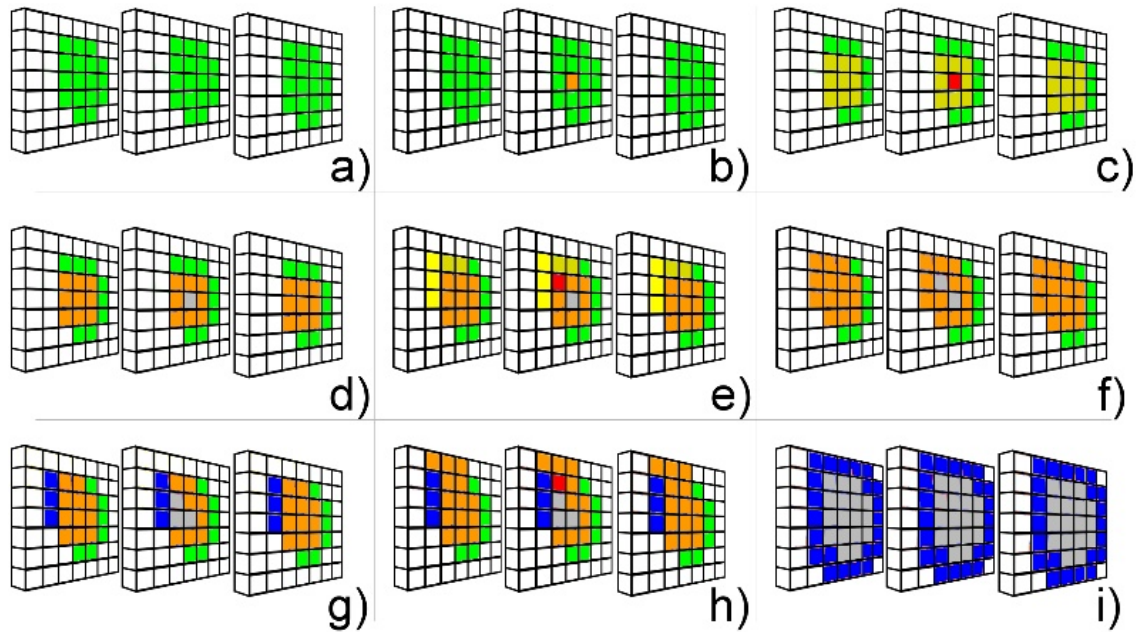
Region growing has to start on the inside of a vessel. Otherwise regions outside the vessels would become part of the segmentation<sup>34</sup>. Therefore every voxel not meeting the growing criterion (4.4a or 4.4b) can be considered to be the first voxel outside the lumen and thus part of the vessel “hull”. Although this hull does not depict the anatomical reality, storing these “hull points” can be useful for later visualization. For example the blood flow could be visualized as vector lines in a semi transparent hull.

Figure 10 illustrates the region growing process for a region of 3×7×7 voxels:

- a) All voxels inside the vessel are colored in green
- b) A seed point is set (orange)
- c) If it does not meet criterion (4.4a) (as assumed in the example – indicated by the color red), all voxels in the 3×3-neighborhood are investigated (yellow).
- d) Since this 3×3-neighborhood meets criterion (4.4b), the original voxel is added to the region (grey); all neighborhood voxels are added to the seed set
- e) The next seed is selected from the seed set. Since it again does not meet criterion (4.4a) (again indicated by the color red), its neighborhood is investigated again
- f) The red voxel passes criterion (4.4b) and its neighbors are added to the seed set
- g) Some of the new seeds do neither path criterion (4.4a) nor (4.4b) and are thus marked as “hull voxels”; their neighbors are not added to the seed set
- h) Other “hull voxels” are determined in the same way
- i) Final segmentation result

---

<sup>34</sup> How the initial seeds are selected in a way to ensure this will be explained at the end of this chapter.



**Figure 10: Growing progress illustrated by a region of  $3 \times 7 \times 7$  voxels**

green: Voxels inside vessel, orange: Seed voxel for growing step, red: Investigated voxel not meeting criterion (4.4a), yellow: Voxels investigated for criterion (4.4b), grey: Voxel belonging to the segmentation result, blue: Voxels depicting stationary tissue (“vessel hull”)

Since leaking did not pose a problem during segmentation, criterion (4.2) could be abandoned to accelerate the segmentation process. This way, the whole branch based approach could be discarded which allowed to eliminate the time consuming branch detection.

Regarding the seed points, the good contrast of the preprocessing result allowed to implement a function for the generation of an initial set of seed points. While in the original implementation seed points had to be set manually a search for local maxima ensured suitable seed points to be found. The only parameter to the algorithm is the number of local maxima to be searched for, i.e. the number of partitions the original volume is divided into before the local maximum in each partition is searched for. Due to the high connectivity of the vessel tree depicted in the Ohio data (as can be seen in Figure 11), taking the local maximum of the whole volume as a seed voxel was enough to get a segmented volume with more than 56% (81,756 out of 145,990 voxels) of the final segmentation result. Two partitions already led to more than 94% of the final

segmentation result and 100% were achieved with 16 seeds. Figure 11 shows the segmentation outcome.

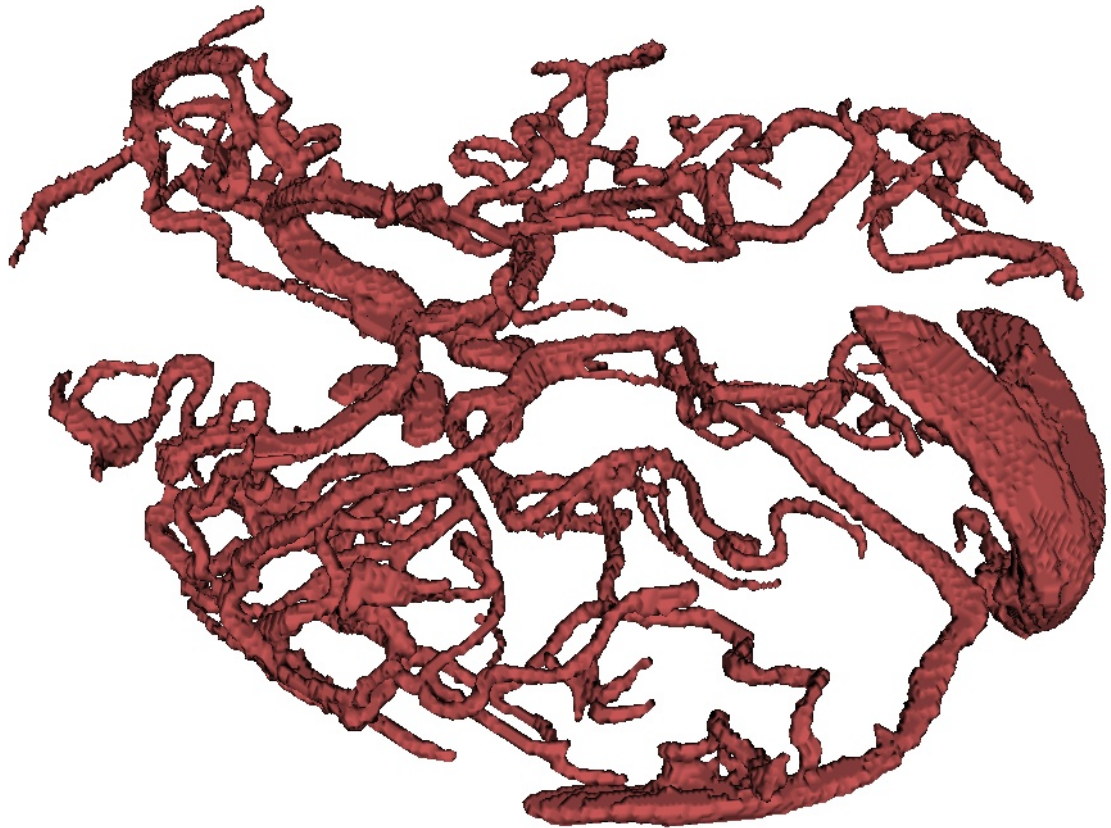


**Figure 11: Final segmentation result**

But since the software is intended to work on less connective vessel trees as well, the number of partitions was set to 64. Such a decomposition of the volume, however, can cause partitions which do not contain any vessels at all and thus produce seed points outside the vessel tree. This again would generate regions outside the vessels to be segmented because criterion (4.4b) allows regions to be segmented even if their average value is below  $th_{low}$ , as long as they are homogenous. Figure 12 illustrates this bearing.

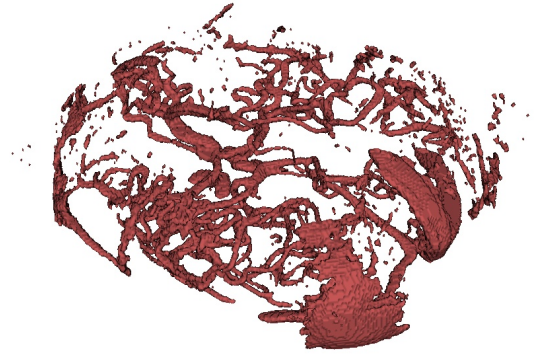
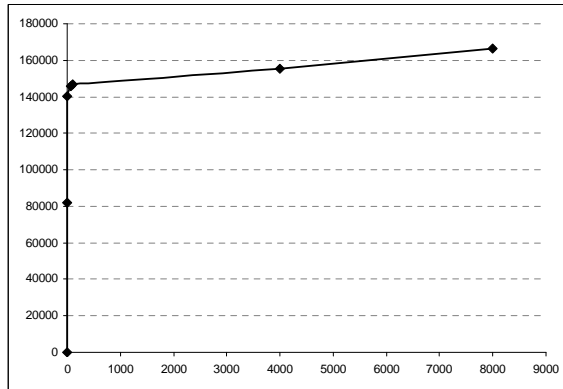


**Figure 12: Over-segmentation caused by seed points outside the vessel volume**

**left:** size of the segmented region in voxels (ordinate) depending on the volume partitioning: with increasing number of partitions, the more likely become seed points outside the lumen. cause only a linear increase of the segmentation volume

**right:** segmentation result for 8000 seed points which shows significant over-segmentation. The lower right corner of the right image, for example shows parts of the skull that have been mistakenly segmented.

The high number of seed points used to produce the over segmentation in the right part of Figure 12 is far from the values used in practice. But as can be gathered from the linear increase in the diagram, each seed outside the lumen contributes roughly the same amount of voxels to the segmentation result.

Therefore a seed point with an intensity significantly lower than the average intensity of all seed points is removed from the set before region growing starts. Figure 13 shows that with this approach the segmentation result does not significantly change anymore with an increasing number of seeds.

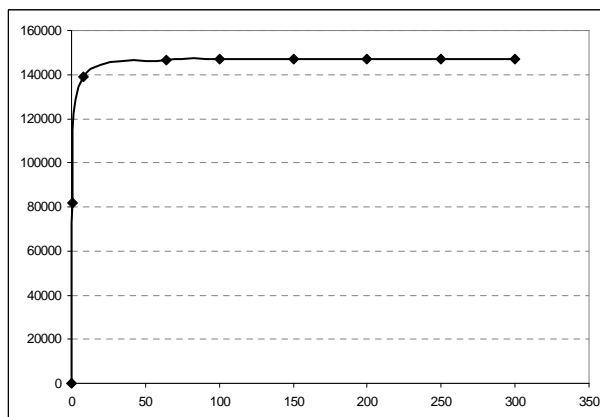


**Figure 13: Prevention of over-segmentation by eliminating seeds outside the vessel volume**

**The size of the segmented region in voxels (ordinate) depending on the number of initial seed points (abscissa) with elimination of seed points outside vessels**

### 4.3 Post-processing

For the purpose of rendering, the segmentation result is satisfactory. The segmented vessels, however, contain a view gaps and holes, usually not more than one voxel in size but nonetheless quite interfering with the task of center line extraction that will be described in chapter 5. For this reason the outcome of the segmentation was post processed with an image processing operation called closing, which is very suitable to correct such deficiencies in binary images<sup>35</sup>.

Closing is strictly speaking a combination of two elementary operations called “dilation” and “erosion”. These two operations are so-called morphological operations. All these techniques base on a so called “structuring element” (SE) [13, set 5/p.3] which can be seen as a mask containing one special voxel sometimes called “origin” or “application point”<sup>36</sup>. The mask (or kernel, as it is usually called) is put over each voxel of the binary image<sup>37</sup> and the value of the voxel under the application point is either retained or deleted depending on the values of the remaining voxels under the kernel. Dilation and erosion are the two simplest morphological operations. If the SE is used for dilation, the voxel under the application point is set if at least one voxel covered by the other voxels of the mask is set. Erosion deletes the application point, if not all the voxels under the kernel are set. [12, 9. 102] Figure 14 gives an example for such a morphological operation.

---

<sup>35</sup> Since the segmentation assigns to each voxel a certain value depending on whether it belongs to the segmentation result or not, the segmentation result itself can be seen as a binary image even if scalar values are not 0 or 1.

<sup>36</sup> Morphological operations were first used on two dimensional images and thus the application point might be a pixel, but since this thesis deals with three dimensional image processing, the word voxel will be used.

<sup>37</sup> Most morphological operations can, with some modifications, also be performed on grey scale images.

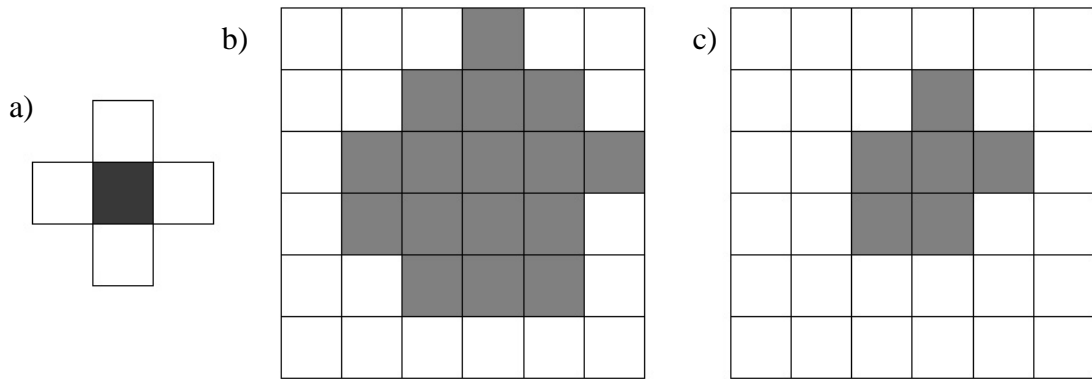


**Figure 14: Morphological operations**

- a) A “structuring element” with its application point (black)
- b) A binary image
- c) The outcome of an erosion performed with the structuring element depicted in a)

The closing operation used to eliminate little gaps in the segmentation result is merely erosion performed on the result of dilation as can be deduced from Figure 15.

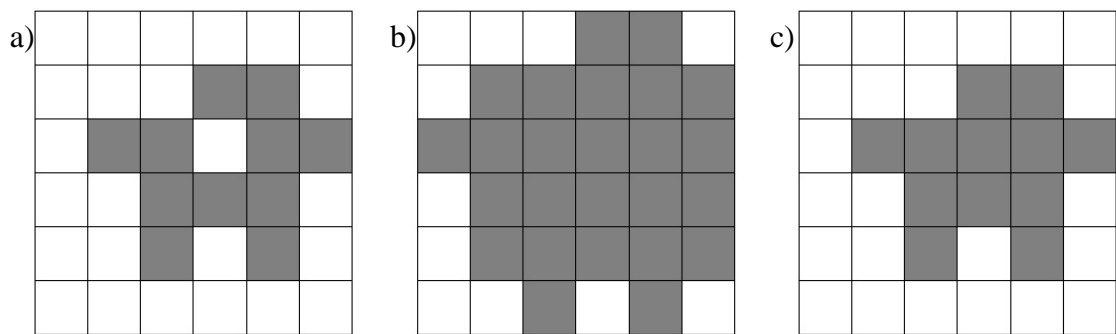


**Figure 15: Closing as an example for a morphological operation**

- a) Original picture
- b) Result of the dilation of Figure 15 a) performed with the same structuring element as used in Figure 14
- c) Result of the erosion of Figure 15 b) performed with the same structuring element as used in Figure 14

As can be seen, the hole in the middle is filled (“closed”) after the operation without changing the original image otherwise.

#### 4.4 Remarks about the Segmentation Result

The closing operation introduced in the previous section can, however, always cause some undesired changes in the original image. This is why it has to be used with care especially on medical data. Figure 16 gives an example for such an undesired effect, as it shows, how the arteria cerebri posterior and the arteria superior cerebelli appear to recombine in the closing result.

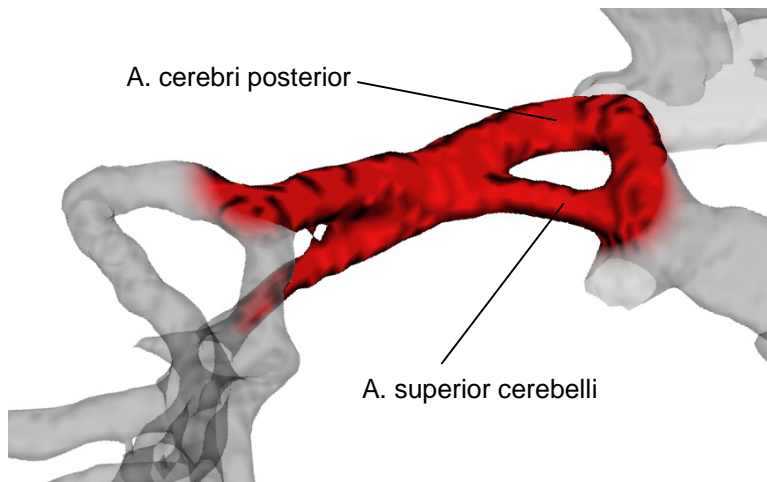


**Figure 16: Incorrect ostensible recombination of the arteria posterior cerebri and the arteria superior cerebelli in the closing result**

Most of these bogus connections, however, occur even if closing is not performed on the data. The reason is, that most of the false connections are the result of limited resolution and not closing. If the distance of two vessels is below image resolution, they appear to be connected. A maximum intensity projection (MIP)<sup>38</sup> over some slices from the preprocessing result<sup>39</sup> clarifies this issue (Figure 17).

---

<sup>38</sup> From several parallel slices, only the pixel brighter than any corresponding pixel within one of the other slices is carried over to the final image.

<sup>39</sup> No closing was performed on the data in the example.

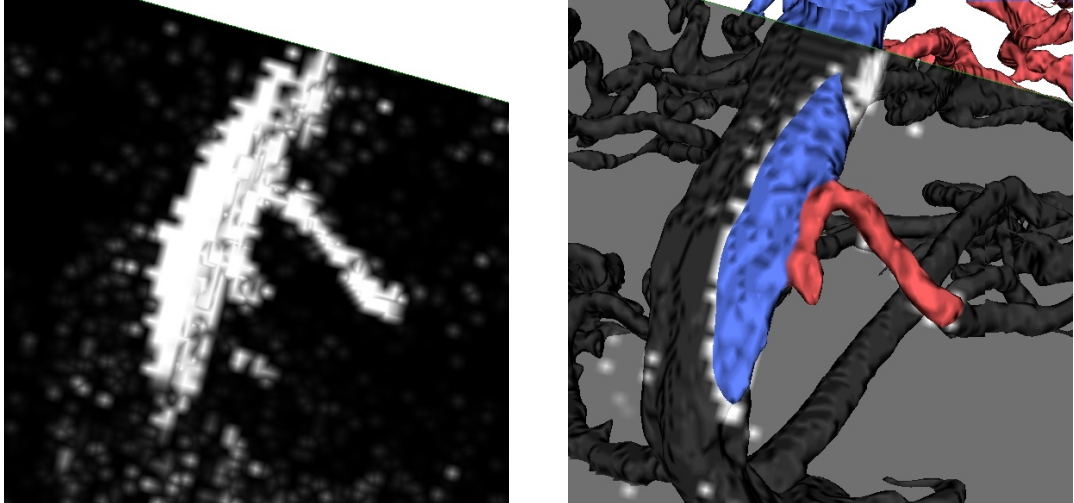


**Figure 17: Vessels wrongly segmented as connected due to limited special resolution**

**left: MIP of eleven parallel, double oblique slices**

**right: Segmentation result with the rearmost slice used for the MIP depicted semi-transparently<sup>40</sup>; the sinus sagittalis superior was manually colored to clarify the true vessel course**

Despite these inaccuracies (which will be subject in section 6.4 again), the quality of the segmentation result is perfectly sufficient to pursue the approaches introduced in chapter 3.

But although the segmentation produced a detailed 3D-volume of the cranial vessel tree, other MRI techniques like TOF are much more suitable for the volumetric acquisition of vessel lumina, as Heiland [8, p.680] points out. And since a TOF scan of the cranium takes less than 15 minutes, a comparative analysis of the overall results might be worthwhile. Unfortunately, the Ohio-data does not include any modalities better segmentable than PCA.

---

<sup>40</sup> The bright spots are high scalar values in this rearmost MIP slice with contrast enhancement applied.

## 5 COMPILATION OF AN ABSTRACT MODEL OF THE VESSEL TREE

It has been said in the first chapter already that the most promising approach to reduce the PCA data needed for flow evaluation or, in other words, to generate reliable results even from PCA data with sparse resolution, is to use information about the vessel tree's geometry. The topological structure of the vessel tree has to be converted into an abstract representation of the vessel tree. The latter can be best modeled in the form of a tree data structure consisting of special node class objects linked together<sup>41</sup>. First step to such a tree model is the centerline extraction which will be subject of the next section.

### 5.1 Centerline Extraction

#### 5.1.1 Definition and Methods

As the name already implies, a centerline is a line, which runs through the geometrical center of either a plane figure or a volume. In the simplest case of a rotationally symmetric object, the centerline would be the rotational axis itself. But in case of an asymmetric object, definition is more difficult.

A. Telea and A. Vilanova [34, p.1] summarize the criteria a centerline should fulfill in five requirements:

*“...A centerline should be*

- 1. connected: the centerline of a compact 3D object should be a set of connected voxels.*
- 2. centred: centerline voxels should be locally centred with respect to the object's boundary.*
- 3. thin: centerlines, represented as voxelized curves, should be as thin as possible ideally, not thicker than one voxel. ”*

---

<sup>41</sup> Since this is one of the most common data structures of all, it will not be explained here. Refer to [26, p.61-72] for a detailed description of trees as a data structure.

The authors furthermore name two requirements rather concerning the quality of the centerline extraction algorithm:

- “4. *insensitive to boundary noise: small surface details should not produce large twists or numerous small branches on the centerline. A simple threshold should allow gradual removal of such branches, keeping the object thin and connected.*
5. *efficient to compute: computing centerlines should run robustly and quickly on large volumes.*”

Sometimes the set of all centerlines of a complex object is called “skeleton”. The centerline extraction implemented in the course of this thesis, tries to meet all these requirements as far as they seem useful for the generation of an abstract model, which is true for four out of these five criteria. Only the second requirement is mitigated because it is not of advantage for the purpose of determining the vessel tree’s structure to have a perfectly centered skeleton.<sup>42</sup>

For binary volumes like the segmentation result of the Ohio data there exist two common approaches for centerline extraction: thinning and distance based approaches.

Distance based approaches work by calculating the minimal distance of every voxel of the object to the object’s boundaries, an operation called distance transform. In the ideal case, all the maxima of these distances indicate centerline points as the maxima in the right part of Figure 18 (white line) do for the example of a rectangle.

---

<sup>42</sup> Due to the discrete nature of digital image data, a perfectly centered point often does not exist anyway: a cube consisting of  $2 \times 2 \times 2$  voxels for example has evidently no center in voxel space.

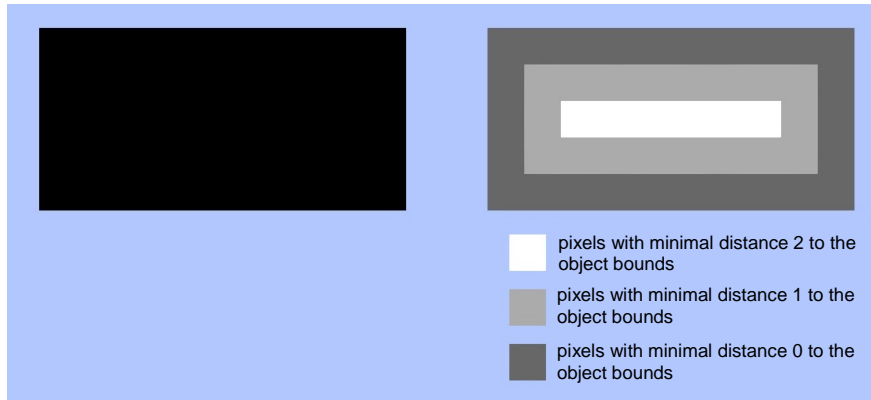


**Figure 18: 2D-Distance mapping**

**left: 2D-object**

**right: the object's distance transform map (chessboard weighted)**

The brighter the pixels in the right image of Figure 18, the further they are away from the blue background. Such an image is called distance transform map (DTM). Thus, the white stripe in the middle of the right image can be considered the black object's centerline. This approach will be explained in detail in section 5.1.2.

Thinning works by continuously removing all voxels at the boundary of an object, until only a volume one voxel in diameter, i.e. a centerline remains. Such an approach will be dealt with in section 5.1.3.

No matter how the skeleton is obtained, it is an excellent foundation for an abstract representation of a vessel tree, and can be directly stored in the common form of a tree data structure, where the centerline points serve as nodes of the tree connected over edges representing short vessel segments.

## 5.1.2 Detection of Centered Points by Means of Distance Transform Maps

### 5.1.2.1 Local Maxima of Distance Transform Maps as Centerline Nodes

The visualization toolkit (VTK)<sup>43</sup> offers several methods for extracting DTMs which in their output only differ in the way, the distances of the voxels to their object's boundaries are weighted. Let  $p$  be the investigated voxel from the set of all voxels  $P$  of an object and  $q$  the closest voxel from the set  $Q$  of all voxels outside the object. Then the distance between  $p$  and  $q$  can be expressed in different ways [6, p. 53]<sup>44</sup>.

City block distance expresses the minimal distance  $d$  of a voxel  $p$  to another voxel  $q$  in Cartesian space as

$$d = |p_x - q_x| + |p_y - q_y| + |p_z - q_z| \quad (5.1)$$

chessboard distance expresses the minimal distance as

$$d = \min(|p_x - q_x|, |p_y - q_y|, |p_z - q_z|) \quad (5.2)$$

and the Euclidean distance between the voxels is calculated according to

$$d = \sqrt{(p_x - q_x)^2 + (p_y - q_y)^2 + (p_z - q_z)^2} \quad (5.3)$$

While the first two algorithms are faster, the third algorithm is more suitable for the task of centerline extraction and other processing steps used to generate the abstract vessel tree and was thus used in the implementation.

As illustrated in Figure 18, in some cases, especially for two dimensional objects, the maxima of the distance transform map already form the centerline, or more generally speaking, the centerline can be often created by connecting the local maxima of the DTM, as shown in Figure 19.

---

<sup>43</sup> VTK is an open source graphics engine. Visit [46] for detailed information.

<sup>44</sup> The equations in [6] refer to two dimensional images and have been adapted for this thesis.

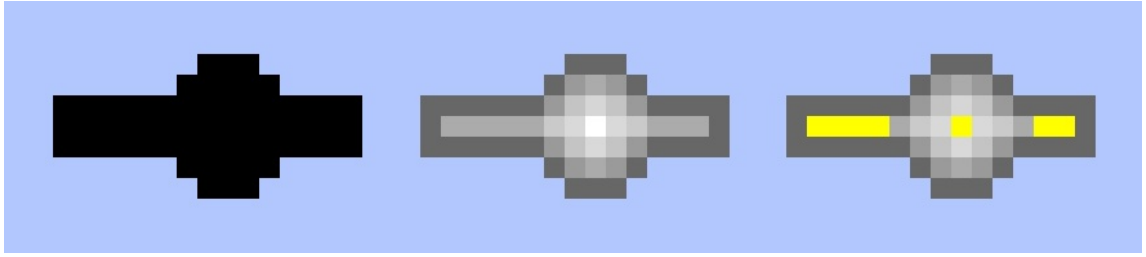


**Figure 19: Local maxima of a distance transform map**

The chessboard-weighted DTM of the black object on the left is displayed in the middle; on the right, the DTM is shown with its local maxima marked yellow.

To connect the local maxima of Figure 19 one can start with an arbitrary maximum, connect it with its closest neighbor and continue this way with this neighbor. The result of storing all local maxima in an appropriate data structure and connecting them among each other is a graph with the maxima themselves being nodes of this graph and the connections representing its edges.

To find the closest neighbor of a graph, different approaches are viable. The simplest way is to calculate the distance to all other maxima and choose the closest connectable maximum. A maximum is considered connectable, if the new edge between them does not intersect the objects hull. This approach is of complexity  $O(n^2)$  and thus not ideal for large volumes with numerous maxima.

Other approaches for the task of connecting closest neighbors are classical algorithms for the construction of minimal spanning trees<sup>45</sup>, like Priority Search [31, pp.526], the algorithm of Kruskal [31, pp. 531], or the algorithm of Prim [31, pp. 520] (also known as Dijkstra Algorithm). Such algorithms, however, would cause sham bifurcations within major vessels as will be explained later.

Therefore a different approach was implemented, where in a first step only the distances of every maximum to the center of the image volume is calculated and all maxima are stored in a map indexed by this distance. To find the closest neighbor of a local maximum  $p$  with distance  $d_p$  to the center, only maxima  $q_i$  with a similar distance to the center or, in other words, maxima with a small difference  $|d_p - d_{q_i}|$  are investigated. Due to the fact that all maxima are stored ordered by their distance to the center, this can be accomplished by searching simultaneously up and down in the map starting at the

<sup>45</sup> I.e. a connected graph where the combined length of all edges is minimal. See [31, p.474] for details.

position of  $p$ . Whenever a connectable node closer to  $q$  than any previously encountered connectable maximum is found, its distance  $\delta$  from  $p$  can serve as a (new) upper bound for the difference  $|d_p - d_{q_i}|$ . As soon as the search up or the search down the map only finds nodes with  $|d_p - d_{q_i}|$  bigger than  $\delta$ , the search can be discarded in this direction. Figure 20 demonstrates this method.

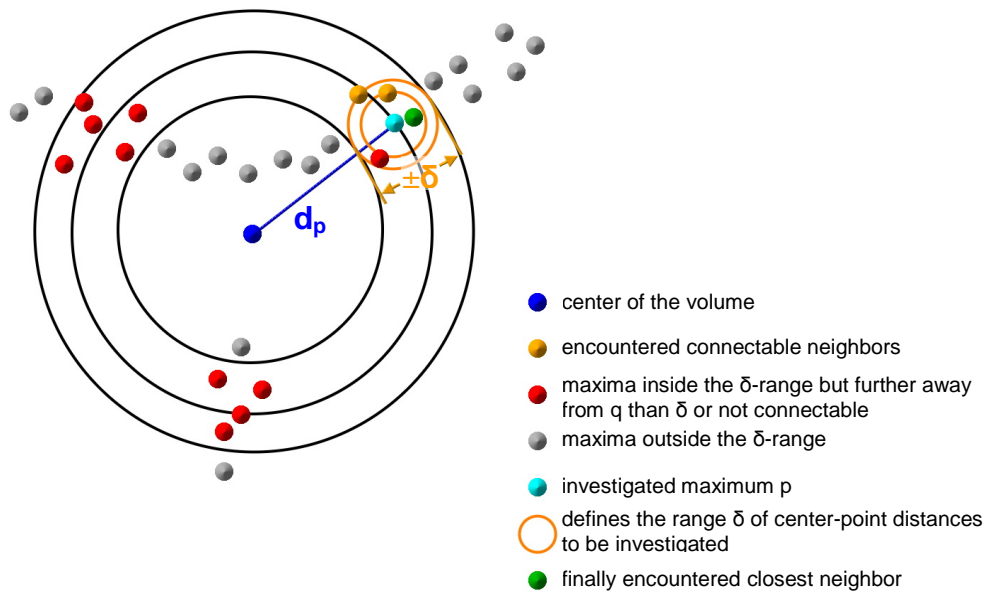


**Figure 20: Approach to reduce effort concerning the search for closest neighbors**

The described approach performs well for maxima connection but was abandoned in favor of a more general method not requiring all maxima to be known in advance, which will be described in section 5.1.3. It is, however, still in use for a similar task, which will be described in section 5.1.4.

#### 5.1.2.2 Issues Concerning Maxima Ambiguity

For complex two dimensional and even fairly simple three dimensional objects, the determination of the centerline nodes cannot be accomplished as easily as described above even for symmetrical objects. Especially ambiguity among maxima in objects lacking rotationally symmetry impedes the distance based approach, as Figure 21 illustrates. On the left, it shows a radial symmetrical 3D model based on the object from Figure 19. The yellow spheres symbolize local maxima of the DTM, the blue sphere is the overall maximum.

On the right, the spherical bulge is stretched, which causes two new local maxima to appear, having the same minimal distance to the object's bounds as the blue sphere in the middle. Such multiple maxima belonging to the same section in the centerline will be referred to as maxima multiplets in the following.

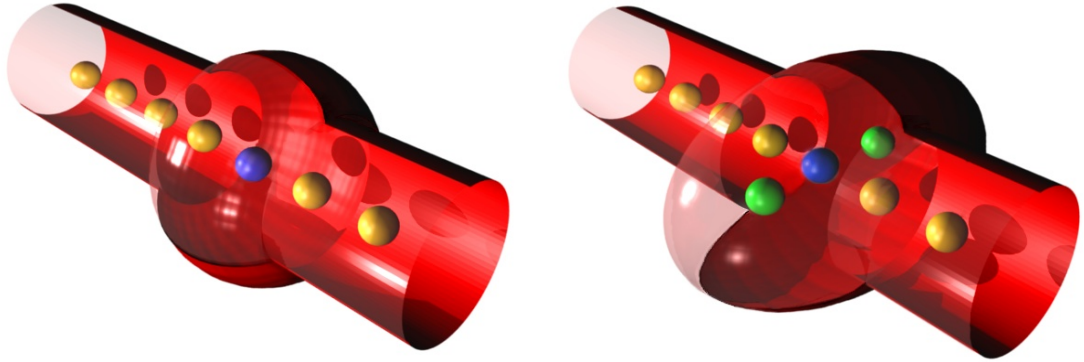


**Figure 21: Effect of a loss of radial symmetry on DTM maxima**

**left: A radial symmetrical bulge in a vessel has no effect on local maxima**

**right: A bulge without radial symmetry causes multiple local maxima**

The problem with such multiplets is that they for one thing (as already indicated before) prevent minimal spanning tree algorithms to be used for tree creation, since this would cause bifurcations within not branching vessels as Figure 22 explains.

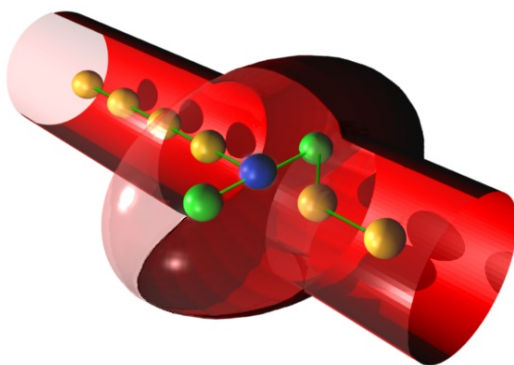


**Figure 22: Minimal spanning tree between DTM maxima**

**with undesired bifurcation at the blue node**

Such undesired branches of the centerline are hard to distinguish from justified ones at vessel bifurcations.

In the case of centerline creation by means of the described closest-neighbor method the negative effect of such ambiguous local maxima cause meanders (i.e. a sinuous structure) within vessels. While close-by surplus maxima usually just cause some zigzagging which, however, is fairly easy to handle, some vessel profiles cause multiplets, with maxima further apart from each other than from the next multiplet. One of the meanders caused thereby is shown in the left of Figure 24.

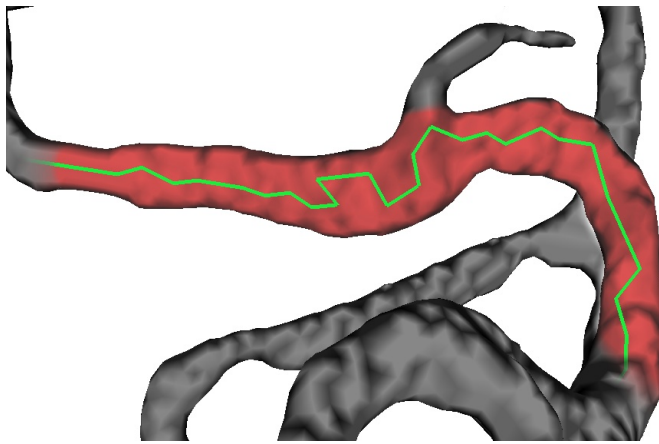


**Figure 23: Zigzagging of the centerline caused by maxima multiplets**

These meanders are hard to distinguish from bends caused by curved vessels (right part of Figure 24) and have thus to be prevented.

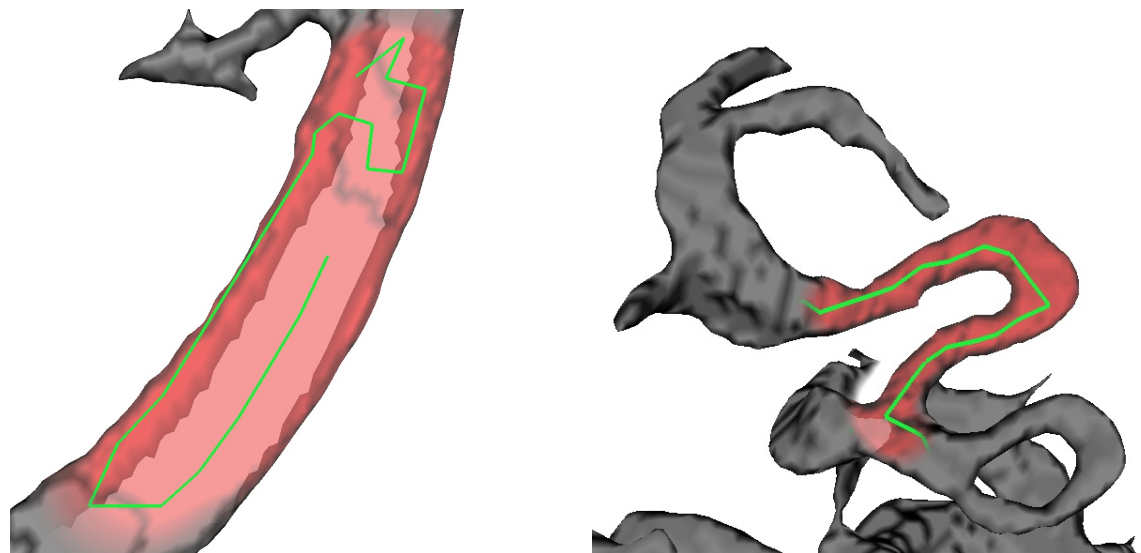


**Figure 24: Centerline meanders caused by ambiguous local maxima**

Meanders due to maxima multiplets (left) are hard to distinguish algorithmically from true bends of a vessel (right)

Several approaches were tested to prevent surplus maxima. One was to average the position of close-by maxima if their distance from each other was below a given threshold. Another one was to average over a neighborhood of encountered maxima as soon as its amount of nodes reached a predefined number. Both approaches, however, could not distinguish whether a maximum was already close to the vessels center or not. This caused undesired as well as desired maxima to be substituted and thus many unpredictable effects on the resulting centerline especially in the vicinity of branches occurred. Much more promising seems an approach, which averages over local accumulations of maxima, since such accumulations' barycenter can be expected to be close to the vessels center due to its roughly symmetrical profile. Such an approach would preferentially shift maxima closer to the center of the vessel. However, finding such accumulations and computing their barycenter for an existing set of maxima would be computationally costly.

Therefore, a way to average such accumulations before centerline extraction is performed creation had to be found.

### 5.1.2.3 Averaging Over Multiple Local Maxima by Gaussian Filtering

Such an averaging in advance can be done by applying a Gaussian (blur) filter on the distance transform map.

A Gaussian filter works similar to the closing filter explained in section 4.3 but its kernel is a “discrete approximation of the Gaussian function” [12, p.29]. Figure 25 shows two such kernels with a size of 3×3 (left) and 5×5 pixels (right) for a two dimensional filter operation. Because the result is not binary, the kernel contains rational numbers.

$$\frac{1}{16} \cdot \begin{array}{|c|c|c|} \hline 1 & 2 & 1 \\ \hline 2 & 4 & 2 \\ \hline 1 & 2 & 1 \\ \hline \end{array} \quad \text{or} \quad \frac{1}{159} \cdot \begin{array}{|c|c|c|c|c|} \hline 2 & 4 & 5 & 4 & 2 \\ \hline 4 & 9 & 12 & 9 & 4 \\ \hline 5 & 12 & 15 & 12 & 5 \\ \hline 4 & 9 & 12 & 9 & 4 \\ \hline 2 & 4 & 5 & 4 & 2 \\ \hline \end{array}$$

Figure 25: 3×3- and 5×5- kernel for a Gaussian filtering operation [12, p.29]

As long as the filter kernel has approximately the dimensions of the vessel's profile, neighboring maxima multiplets are substituted with a new maximum in their barycenter as shown in Figure 26.

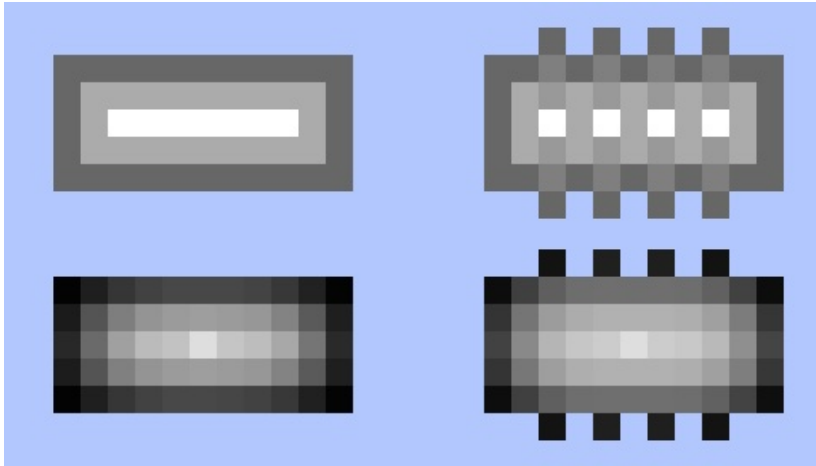


**Figure 26: Averaging over accumulations of local maxima in DTMs by Gaussian filtering**

**left: connected local maxima in a chessboard DTM (top) are averaged to one remaining local maximum<sup>46</sup> by Gaussian filtering (bottom)**

**right: even unconnected local maxima (top) are averaged to a single local maximum<sup>46</sup> by a Gaussian filter of sufficient kernel size**

The advantage of Gaussian filtering towards other filters like the Median filter is that it emphasizes the general distribution of grey values in the DTM. In tubular structures the overall maxima of the DTM in a certain branch segment can be expected to be situated in the center of the vessel already. The undesired surplus maxima, however, disperse around the center. In contrast to the Median filter, the Gaussian filter reduces this dispersion which causes the new local maxima to be more centered.

Figure 27 shows the effect of Gaussian filtering on the DTM of the segmentation result. Figure 28 illustrates the positive impact on centerline extraction.

---

<sup>46</sup> The outcome of the Gaussian filter has been contrast enhanced.

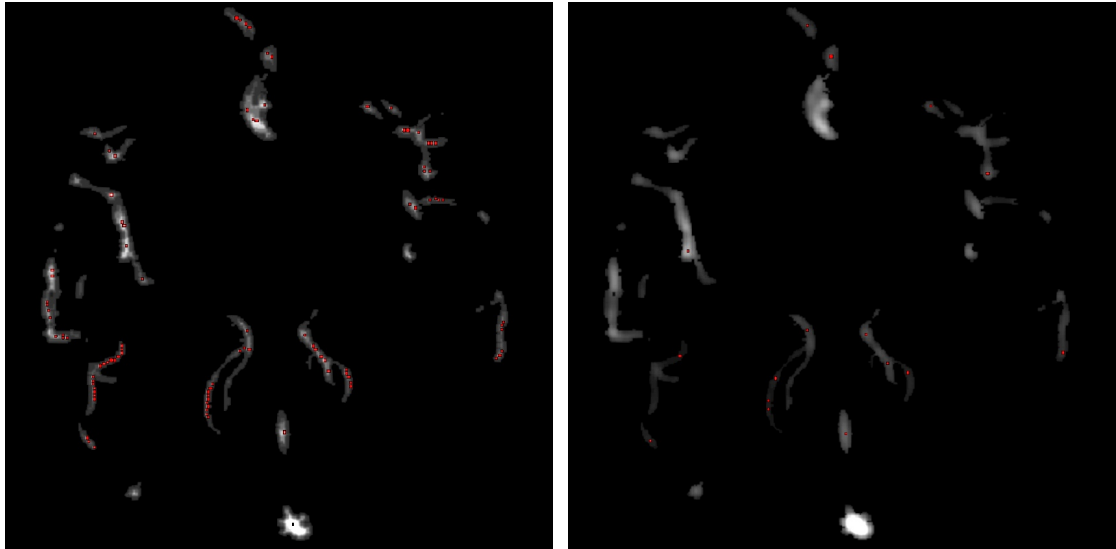


**Figure 27: Averaging over local maxima by applying Gaussian filtering<sup>47</sup>**  
left: local maxima before - right: after using a Gaussian filter.

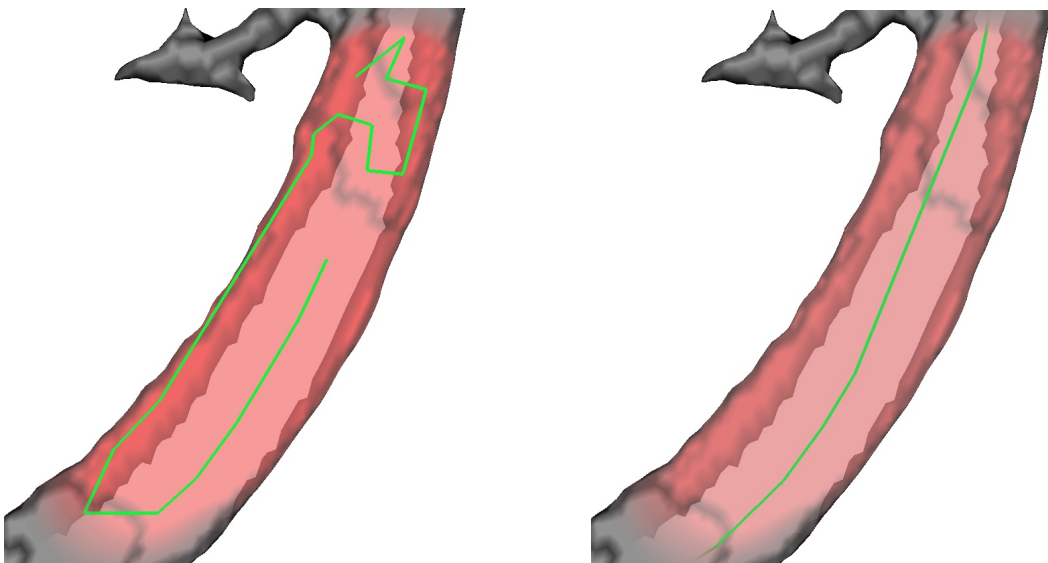


**Figure 28: Elimination of meanders by means of Gaussian filtering**  
left: Centerline with meanders before filtering  
right: Corrected centerline

As implied before, the kernel size of the filter should roughly reflect the vessel diameter. However, a tradeoff has to be found, because the ROI usually contains vessels of quite

---

<sup>47</sup> The filtered data is the segmentation result of the Ohio-data. In some areas local maxima seem to have completely disappeared. Yet, these are just regions where the new local maxima are in another image slice.

different thickness. Yet, if the chosen kernel is too small, some maxima belonging to the same multiplet might be averaged to separate nodes, if the distance between each maximum is larger than the kernel size. In this case the risk of meanders is higher. Choosing a large kernel, on the other hand, leads to a loss of connectivity in small, bended vessels, because the substitution of maxima accumulations with their barycenter can cause so many maxima to disappear, that the remaining maxima are too far apart, to recognize them as connected (compare Figure 29).

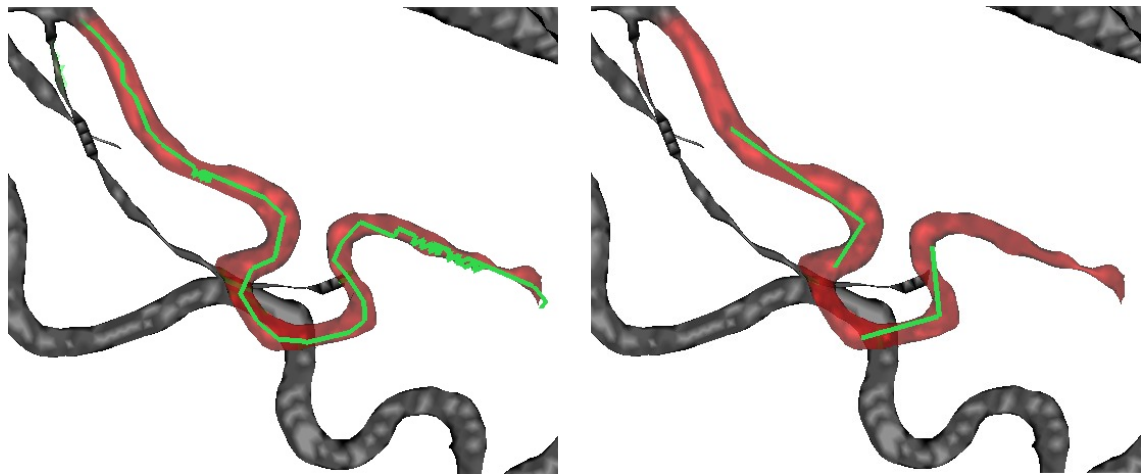


**Figure 29: Loss of connectivity in thin, curved vessels as a result of Gaussian filtering**

**left: Without a Gaussian filter applied to the DTM, the centerline shows excessive zigzagging but excellent connectivity**

**right: Applying a Gaussian filter with a large kernel destroys connectivity of local maxima**

The problems arising from too small kernels can only be solved by specially handling those maxima, which were not connected by closest-neighbor connection. Yet, this method is only promising if few and rather isolated maxima remain apart from the generated centerline, making the use of a rather large kernel inevitable.

The considerable loss of connectivity among the remaining local maxima following thereof has to be addressed by an approach providing a sufficient amount of auxiliary nodes, which can be considered as intermediate nodes for such otherwise unconnectable nodes. Such an approach will be described in the following section.

### 5.1.3 Detection of Centered Points by Means of Topological Thinning

Thinning, as explained in the end of section 5.1.1 is, an approach, which tries to iteratively reduce an objects thickness until only the skeleton remains. Metaphorically speaking, all voxels on the boundary of the object are “peeled off” layer by layer until the thickness has reached one voxel. The crucial requirement for thinning algorithms is, that they are not allowed to change an object’s topology.

Many methods have been proposed in the past. Best known probably are the two introduced by Gonzalez and Woods in their book *Digital Image Processing* [6, pp. 491, pp. 535]. Zhou et al. [37, pp. 1267] propose an improved, combined approach but Sadleir and Whelan [29, p.2] criticize this approach as still leading to imprecise results.

For reasons to be explained later, the crucial quality concerning the search for a suitable thinning algorithm with regard to the requirements of this thesis is maintained connectivity. When compared with other publications the results for 3D images given in [15] seemed to be the most promising. Furthermore the method devised by Julien Lamy poses excellent performance<sup>48</sup>.

The mode of operation can be gathered from [15] in detail and is therefore just summarized to the essential steps in the following.

Removing all voxels layer by layer would not take the topology of an object into account. Such a proceeding would completely remove fine structures connected to thicker objects before these thick objects are thinned to a single line. Hence, all thinning algorithms have to identify which points can be removed without changing the overall topology of the object. Such points will be called “simple points” in the following.

Most thinning algorithms mainly differ in the way these simple points are identified. Often operations similar to the morphological operations described in 4.3 are used as in [34] for example. In these cases several different kernels are applied to the image and only those voxels are deleted whose neighborhood matches on of the kernels.

---

<sup>48</sup> The author claims that his method is nearly 100 times faster then the thinning filter included in the ITK-library [15, p.3]. The thinning of the segmentation result from the Ohio data consisting of nearly 150,000 voxels takes less then 40 seconds on a computer with 3 GHz CPU and 1 GB RAM.

The approach by Lamy identifies such simple points not by applying kernels but it investigates the digital topology<sup>49</sup> of the neighborhood of each voxel. The performance advantage of his approach is based on the fact, that the topological properties of every voxel have to be investigated only once, while the different kernels used in other approaches have to be applied to the image volume for several times. Figure 30 shows the result of the topological thinning applied to the segmentation result of the Ohio-data.

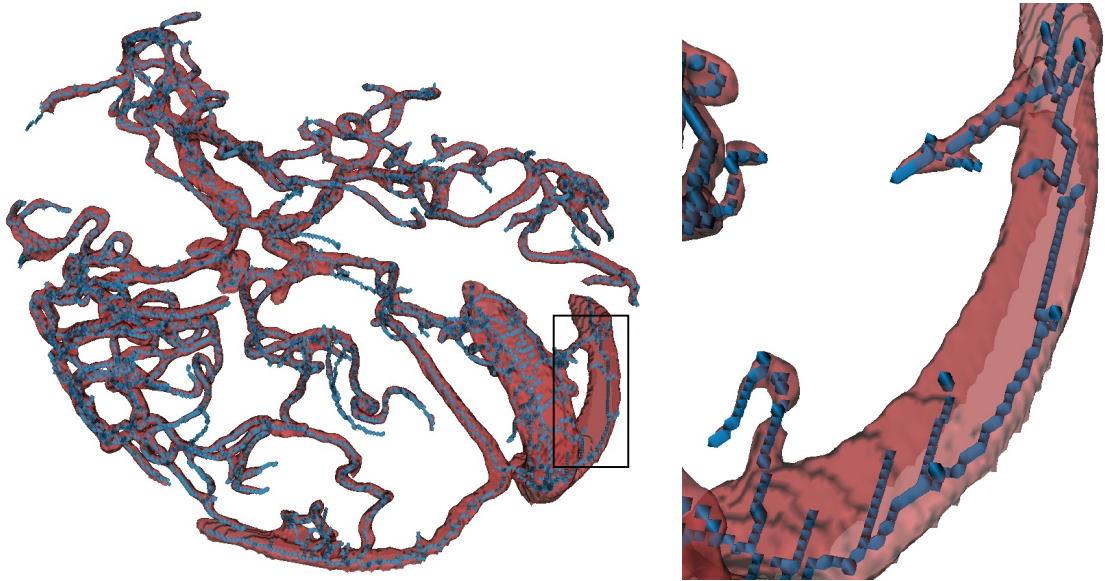


**Figure 30:** Result of topological thinning with a close up of the right sinus transversus

As the close up of the thinning result shows, topological thinning has a similar outcome as the distance based approach of the previous section when used in combination with a minimal spanning tree connection. Again some irregularities in thickness caused undesired bifurcations within the vessels. It however poses much better connectivity and can thus be used to clear the negative effect of Gaussian filtering as described in section 5.1.2.3.

---

<sup>49</sup> Digital topology deals with properties of voxels (or pixels in 2D) which correspond to concepts known from topology in mathematics.

### 5.1.4 A Combined Approach

The method of avoiding meanders by applying a Gaussian filter as explained in section 5.1.2.3 seems to be unadvisable considering the sever loss of connectivity in bended vessels. This loss of connectivity can, however, be remedied by combining the approaches of chapters 5.1.2 and 5.1.3.

The centerline voxels created by topological thinning are used to connect local maxima from the DTM if gaps appear during branch creation. The thus created branch segments are connected in a similar way among each other, using the centerline points from topological thinning again. A complete skeleton of the vessel tree is the result.

#### 5.1.4.1 Branch Creation

This combination works by finding centerline voxels from the topological thinning between close-by local maxima of the DTM from section 5.1.2.3. Candidates for such a connection could, be found in the same way as described in section 5.1.2.1 but with regard to the comparably large number of centerline voxels encountered by the topological thinning, this approach had to be discarded for the sake of performance. Instead, a modified region growing was implemented to perform closest neighbor connection of the DTM-maxima and find intermediate centerline voxels from the topological thinning in one approach.

The algorithm for branch creation consists of three major steps:

1. A vessel tree node  $M$  is created with the coordinates of an arbitrary local maximum from the result of the Gaussian filtered DTM.
2. The corresponding voxel<sup>50</sup> in the segmentation result is set as a seed for the growing algorithm. Growing itself then works similar to the approach described in section 4.2, yet with a simpler, binary growing criterion, which ensures that only voxels part of the segmentation are added to the volume and serve as new seeds in the next growing step.

---

<sup>50</sup> I.e. the voxel with the same coordinates.

In addition, in each growing step the location of any new voxels of the growing region is looked up in the topological thinning image as well as in the DTM-volume. The lookup can cause two operations:

- if the corresponding voxel in the topological thinning volume is a centerline voxel, it is stored in a vector of possible connecting voxels.
- if it is another DTM-maximum, a closest neighbor for  $M$  was found<sup>51</sup>. Region growing then terminates and the branch connection continues with step 3.

If the region growing terminates without encountering a closest neighbor, an arbitrary unprocessed local maximum is chosen from the DTM and the branch creation continues with step 1 until all local maxima have been processed.

3. Another tree node  $O$  is created with the coordinates of the encountered closest neighbor and the software checks, whether the node  $M$  and the new node  $O$  can be directly connected<sup>52</sup>. If not, the centerline voxels previously stored in the vector are used to establish a connection by means of a shortest path algorithm which will be described in the next paragraph. If so, the new node  $O$  serves as seed for the next closest neighbor search and branch creation continues with step 1.

Since the closest neighbors found by the branch creation algorithms often cannot be connected without intersecting the vessel wall, it is necessary to utilize the centerline voxels from the topological thinning to bridge such gaps.

The centerline voxels encountered during region growing are partitioned into those voxels which are directly connectable to the node  $M$  and those being connectable to the new node  $O$ .

If one of the centerline voxels is connectable to both,  $M$  and  $O$ , another new node  $N$  is created with the coordinates of this voxel and used to establish the connection between  $M$  and  $O$ .

---

<sup>51</sup> The growing algorithm is implemented in a way, which ensures that growing progresses in layers around the original seed. Hence, any voxel examined in an iteration belongs to the same layer and thus has the same distance to the original seed as any other investigated voxel, until all voxels of the same layer have been processed. In this way, the first encountered (other) local maximum of the DTM must be one of the closest neighbors.

<sup>52</sup> Two nodes are connectable, when an edge between them wouldn't intersect the vessel wall.

Otherwise the centerline voxel  $i$  which is closest to the node it is not connectable to is selected. For example, if  $i$  is in the partition of all voxels not connectable to  $O$ , but closer to it than any other voxel in this partition then  $i$  is chosen if any voxel  $j$  from the other partition is further away from  $M$  as well. In this way it is ensured, that  $i$  is close to the “middle” between  $M$  and  $O$ . After the new node  $N$  has been created with the coordinates of  $i$ , it is connected with  $M$ . After the connection it serves as new  $M$  in the next iteration step of the shortest path search. The search terminates, as soon as a centerline voxels is encountered, which is connectable to both,  $M$  and  $O$ .

If any at all, then more than one centerline point can usually be found, which is connectable to both nodes  $M$  and  $O$ . The new node  $N$  is in this case created with the location of the centerline voxel  $i$  fulfilling the criterion

$$|dist(i, M) - dist(i, O)| < |dist(j, M) - dist(j, O)| \quad \forall j \neq i \quad (5.4)$$

with  $j$  being the location of any other centerline voxel of those connectable to  $M$  as well as  $O$ ;  $dist()$  is a function returning the squared Euclidian distance between a voxel and a node, if they are connectable and  $\infty$  otherwise.

The result of the combined approach on the vessel displayed on the right side of Figure 29 is shown in Figure 31.

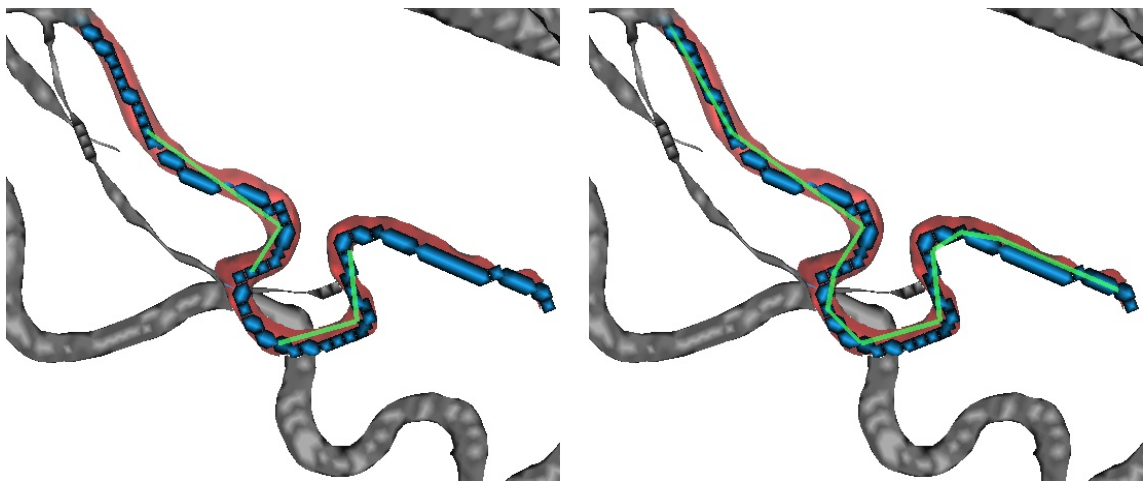


**Figure 31: Connection of local maxima of a Gaussian filtered DTM by centerline points gained from topological thinning**

**left: Result without the use of the centerline points from the topological thinning**

**right: Result when the centerline points from the topological thinning (blue) are used to connect otherwise unconnectable centerline segments.**

The processing steps performed so far create unbifurcated centerlines which can be considered branches of the tree. This is why the entirety of these steps will hence be referred to as branch creation. The thus created branches have to be connected to a tree (or skeleton if seen in the context of centerline extraction) and the necessary steps, henceforth called branch connection, will be explained in the following.

#### 5.1.4.2 Branch Connection

Special care has to be taken for branches that consist of only one node. Most of these (degenerated) single-node branches simply remained unnoticed by the branch creation, because they are not the closest neighbor of any other node. If such nodes are not chosen as initial seed points by chance, they are ignored by the closest neighbor search. These maxima can be ignored, since they are redundant for branch creation.

Not all single-node branches, however, can be neglected, since some represent the only maximum within a short branch segment. One of these brief vessel branches, henceforth referred to as stubs, is displayed below.

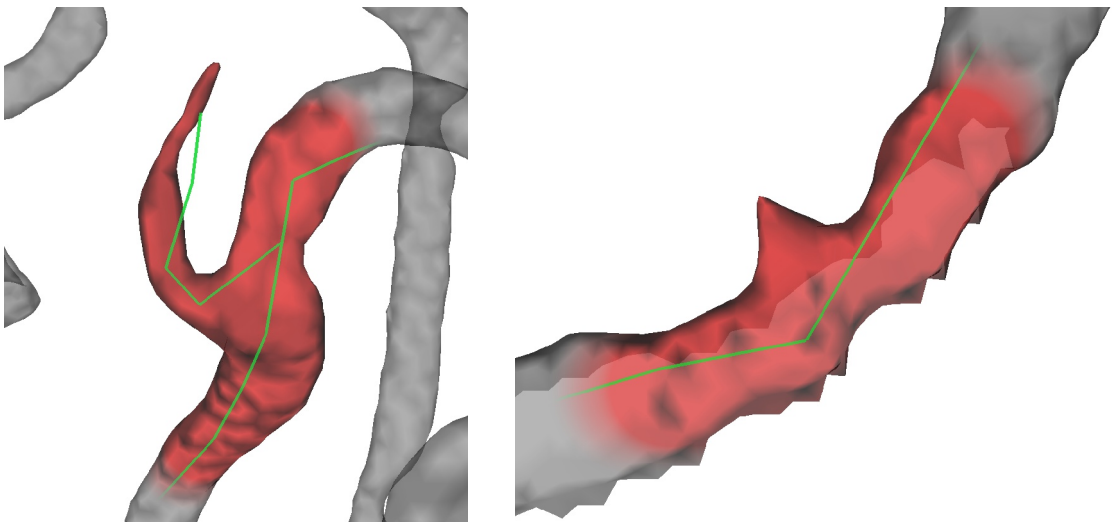


**Figure 32: Vessels with stub branching off**

**left: a stub recognized by the software**

**right: an unrecognized stub**

These stubs, usually the result of imperfect segmentation are of significant importance for flow analysis, since the in- or off-flow at such branches generate leaps in the flow

rate of an analyzed vessel. The cause of this leap in flow rate, however, cannot be made out by the software, if the stub has not become part of the abstract vessel tree.

The algorithm devised to distinguish between isolated local maxima within a vessel and those in a stub works on an assumption about the vicinity of such maxima. A sphere is assumed around such an isolated maximum. Its radius is given by the maximum's distance to the next centerline voxel. If the maximum is not part of a stub, such a sphere should mainly consist of voxels belonging to the vessel lumen. Figure 33 illustrates the basic idea: a region growing starts from the unconnected local maxima (magenta spheres), adding all voxels inside a vessel to the growing region until an existing centerline branch is encountered. Then the volume of the region is compared to that of a sphere, whose radius is assumed to be the distance from the unconnected maximum to the encountered centerline voxel. If the volume of the growing region is bigger than half of the volume of this conceived sphere (as it is the case for the small sphere on the left of Figure 33), the maximum is considered to be just one of those negligible maxima described in the first paragraph of this chapter. Otherwise it most probably indicates a stub, and has thus to be connected to the encountered centerline voxel.

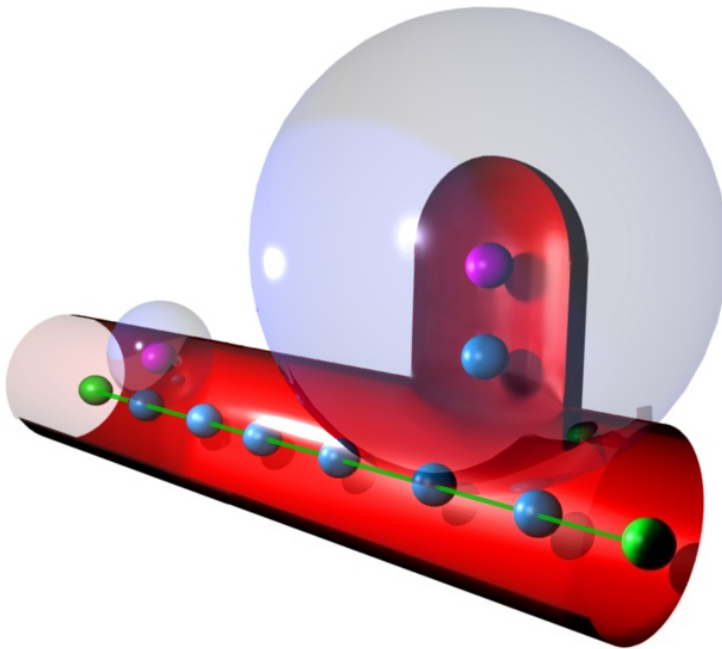


**Figure 33: Distinction between isolated local maxima within processed vessels and within stubs**

**The small sphere on the left surrounds a negligible local maximum, the one on the right belongs to a stub and has to be taken into account during tree assembly.**

The connection is established via the topological thinning's centerline voxels (blue spheres).

The branches consisting of more than a single node are connected with each other by a similar method as the one used for branch creation before. All nodes connected over just one edge can be considered the end of a branch. From these nodes, a region growing similar to the one described section 5.1.4.1 is started. The only difference is that this time the algorithm does not look for another maximum, but terminates as soon as a voxel belonging to another branch's centerline is encountered. This voxel is then converted into a node of the abstract vessel tree<sup>53</sup>. Afterwards it is connected with the end of the original branch (i.e. the local maximum from which the branch connection started). Latter happens by means of the shortest path algorithm described above.

A few centerline voxels created by the topological thinning, however, do not become part of the skeleton. Most of these are the result of inaccurate thinning and removed during the assignment of the vessel voxels to the abstract vessel tree's edges. This process will be subject of section 6.1. Those few remaining are usually situated in short vessel sections between two subsequent bifurcations. These voxels are connected to minimal spanning trees and are used to connect existing branches with each other afterwards. In Figure 34 such a minimal spanning tree of centerline voxels from the topological thinning is shown as a blue line. The existing vessel tree branches are depicted in green.

---

<sup>53</sup> To correctly insert the new node in the tree, the two nodes have to be found, which were connected by the centerline segment the new node is now part of. For this purpose all nodes of the branch are investigated, until these two nodes have been found. This task is coped with by utilizing the algorithm introduced in the end of section 5.1.2.1.

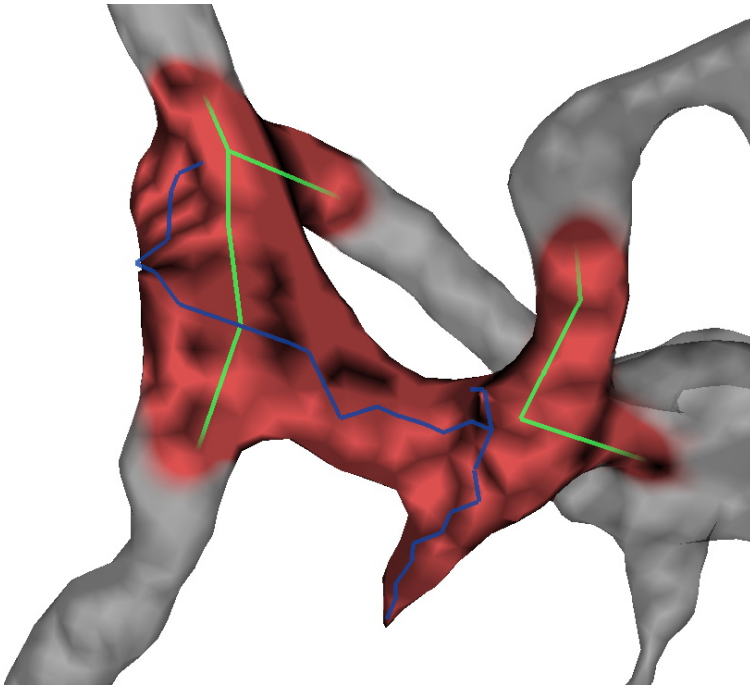


**Figure 34: Unprocessed centerline points connected to a minimal spanning tree (blue) and existing centerline segments (green)**

For the creation of the minimal spanning tree, priority search was implemented. The algorithm is one of the best established for this task and can be found in most literature dealing with data processing algorithms.<sup>54</sup> The basic idea is to start with an arbitrary node as root of the tree. Then the distance (in voxels) of all other nodes to this root is calculated and the one with the shortest distance is connected to the tree. In the next iteration step the remaining voxels' minimal distance to any of the nodes already connected to the tree is calculated. The one with the shortest distance is added to the tree and the minimal distances have to be recalculated, taking the new tree node into account. The algorithm quits as soon as all nodes have either been connected to the tree or none of the remaining nodes can be connected to the tree without intersecting the vessel hull. To reduce the computational complexity, all so far unconnected voxels are kept in a sorted map. The map is called "priority queue" and stores the voxels together with their minimal distance to the tree as index. Thus only the distances of the node just added to the tree to the remaining nodes have to be calculated in each iteration step.

The hereby created minimal spanning trees are then connected to the existing branches of the abstract vessel tree as follows.

---

<sup>54</sup> For example in [26, pp. 252].

First, all nodes of the existing branches, which are connectable to any of the nodes in the minimal spanning tree are stored in a vector.

Afterwards a new minimal spanning tree consisting of all these nodes and the nodes of the minimal spanning tree is calculated by means of priority search as described in the previous paragraph with modifications to the distance weighing as described below.

An existing connection between branch nodes is weighted with the length of the connecting edge, nodes of the existing branch cannot be connected, if they are not connected already (distance is weighted with  $\infty$ ), existing edges of the minimal spanning tree are weight with zero and a connection between a node of the minimal spanning tree and one of the branch nodes is weight with their distance in voxels. As soon as a connection between a branch node and the minimal spanning tree has been established, all nodes are deleted from the vector, for which a path to the minimal spanning tree can be found due to this new connection. In this way, it is ensured that no multiple connections are performed, but that all nodes connectable to the minimal spanning tree are linked directly or indirectly. The result can be seen in Figure 35.

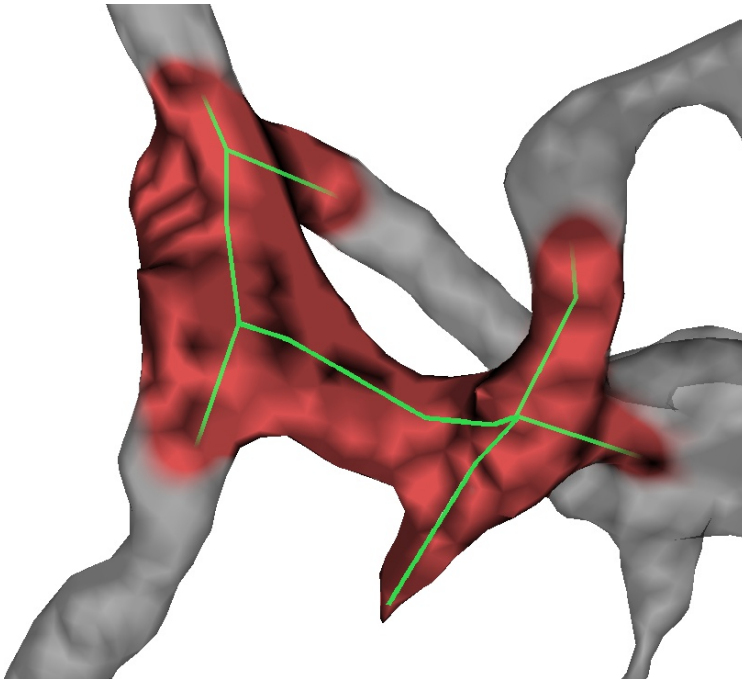


**Figure 35: Result of branch connection over centerline points from topological thinning.**

## 5.2 Assignment of Volumetric Information to the Abstract Vessel Tree

So far, only the skeleton of the segmentation result has been regarded. While the tree model representing this skeleton contains all information about the branching of the real vessel tree already, this information still has to be associated with the actual flow quantities. To achieve this, the voxels of the segmentation result have to be assigned to their corresponding edges of the abstract tree. Together with this volumetric information, the edges represent small sections of the vessel tree hence called “branch segments”. In the abstract vessel tree, these branches are implemented as a class of their own but associated with the nodes of the tree over unique identifiers (IDs).

Until now, all edges have maximal length, which means, removing one node by directly connecting its neighbors in the graph with each other is not possible since every node either represents a bifurcation or the removal would cause the new edge to intersect the vessel hull. Thus, the graph contains a minimal number of nodes until now. This is feasible since the second criterion from the centerline definition from chapter 5.1.1 has been abandoned. As a consequence, the centerline graph is rather edgy, but since angles have to be considered for the later assessment of the flow data, this is a desired condition. In a first step, however, all edges, which exceed a certain length, are subdivided. Subdivision of the edges (and thus branch segments) increases the number of data samples, which is necessary to provide a sound data foundation and to reduce the impact of local data inaccuracies on branch sections as a whole. It is performed by inserting additional nodes into edges exceeding a length threshold.

In the second step, the voxels surrounding the edges are assigned to them by means of a region growing starting from the center point of each edge. The decision whether a voxel of the growing region truly belongs to the edge is based on angular considerations. The edge encloses two angles  $\alpha_1$  and  $\alpha_2$  with the vectors between the voxel and both of the nodes connected by the edge. Only if both of these angles are smaller or equal to  $90^\circ$  (i.e. the intersection cosine is positive), the voxel is assigned to the edge. Figure 36 illustrates this method: a voxel (yellow sphere) is assigned to the blue segment of the centerline, because both of the vectors from the voxel to the nodes connected by the blue edge enclose angles smaller than  $90^\circ$ . The set of all voxels meeting this criterion make

up the transparent blue cylinder making up the volume of the branch segment defined by the blue segment of the centerline.

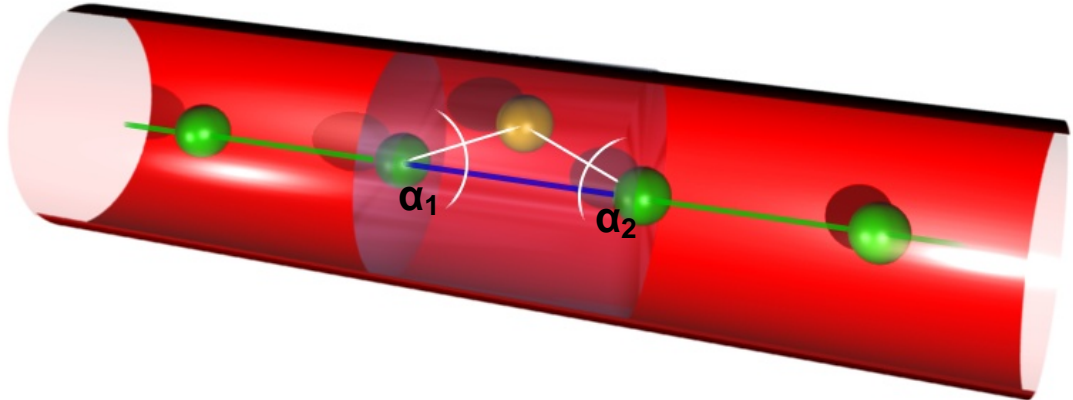


**Figure 36: Assignment of branch voxels to their corresponding centerline edge**

All voxels within the transparent blue cylinder belong to the blue segment of the centerline.

During this assignment, most of the so far unprocessed centerline points from the topological thinning are effaced as mentioned in section 5.1.4.2 already.

If there are two edges in the vicinity of the voxel, meeting the angle criterion (as it happens at bifurcations), the voxel is assigned to the closer edge. The (minimum) distance of a voxel to a line (i.e. edge) is defined by its distance to that point of the line it is perpendicular to. This distance could be calculated by means of vector analysis but since this calculation has to be performed for very many voxels and is computational costly, a different approach was chosen, that will be described in the next paragraph.

By setting all voxels of the centerline segment as seeds and applying a growing algorithm that grows layer by layer (as the one used in section 4.2) it is ensured that all voxels of the same growing iteration have the same distance to the centerline. Actually, the minimal distance of the voxel to the centerline is identical to the number of the iteration step during which it was added to the growing region. By tagging the voxels with both, the unique ID of the branch segment it belongs to and the distance of the voxel to the centerline<sup>55</sup>, it can be assured that a voxel is always assigned to the segment

<sup>55</sup> This “tagging” is performed by assigning a scalar value which is a combination of both, a unique branch segment ID as an integer value and the distance to the segment’s centerline as decimal places.

it is closest by: if a voxel is encountered during region growing, which is already claimed by another segment (indicated by a different ID tagged to the voxel), the distance to this segment's centerline is compared to the number of the current iteration step (and thus the distance to the currently processed segment's centerline). Figure 37 shows an example for the result of this approach.

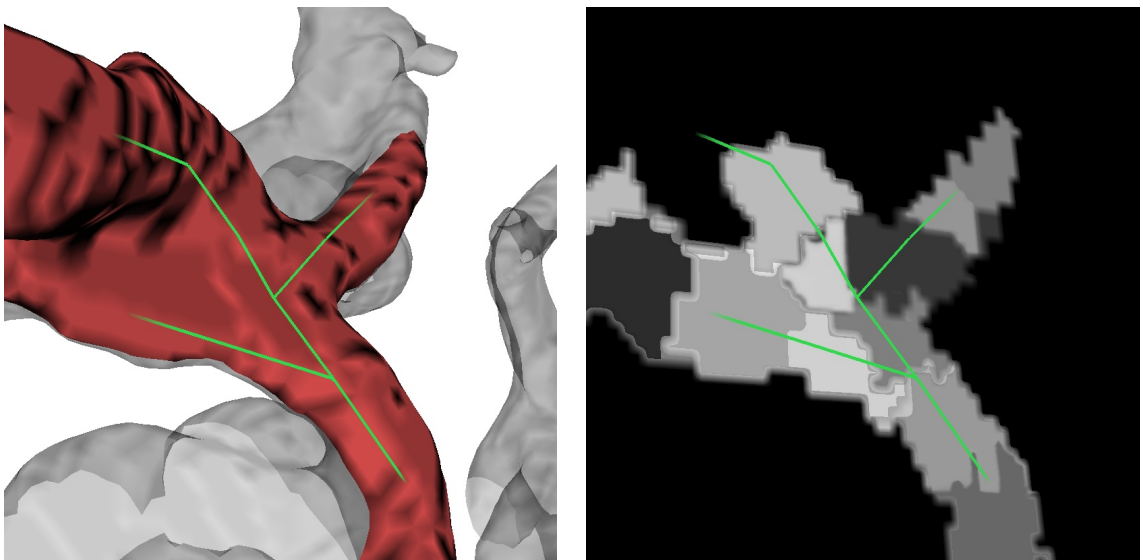


**Figure 37: Voxel assignment to segments with closest centerline**

**left: Centerline course at the confluence of the arteria cerebri anterior and the arteria communicans anterior**

**right: Double oblique slice through the segmentation result with the IDs of the associated branch segment assigned to the voxels**

The image on the right side of Figure 37 is composed of several images of the same slice with different windowing applied, because the IDs of neighboring segments usually differ only slightly which causes bad contrast. That the centerline seems to go only roughly through the segments is caused by the fact that the picture shows only a 2D projection of the 3D centerline onto the slice. Thus, pixels close to the centerline projection do not necessarily depicture voxels close to the true centerline.

The assignment of the branch segments' unique IDs to the voxels of the segmentation result additionally allows the mapping of voxels (and thus coordinates in voxel space) to segments. The resulting image volume can hence be seen as a lookup table, which will be useful throughout the next processing steps.

## 6 EVALUATION OF THE FLOW DATA BASED ON THE ABSTRACT MODEL

### 6.1 Adding Flow Information to the Abstract Model

Three kinds of data structures are available after the processing steps performed so far: an abstract representation of the vessel tree containing all topological information about the physical vessel tree, the volumetric PCA data itself and the just described data volume linking both of the other structures.

The latter can be seen as a kind of lookup table. This lookup table is used to add flow information to the abstract vessel tree. As Laub et al. propose in [16, p.66] for a PCA dataset consisting of three orthogonal PCA volume scans, the scalar values from the different PCA volume scans can be regarded as the components of a three-dimensional flow vector. Yet, this vector reflects only an approximation of the actual flow velocity and direction. The reason is that even if the vector is within the mentioned  $15^\circ$  range of one of the orthogonal axes, the other components are not zero due to noise [26, p.809] (see appendix B.2 for details)<sup>56</sup>.

To calculate the mean flow vector for a branch segment, the different PCA volumes are traversed either simultaneously or one after another and for every voxel the branch segment it belongs to is looked up. This allows adding the scalar value of the voxel to a data structure storing the sum of all flow velocities, component by component. For a branch segment  $B$  consisting of  $N$  voxels, the vector  $\bar{v}(B)$  representing the average flow velocity of the blood within  $B$  is thus determined according to

---

<sup>56</sup> If none of the vector components is roughly perpendicular to one of the axes, all the components are considerably tampered with noise.

$$\mathbf{r}_v(B) = \begin{pmatrix} v_x(B) \\ v_y(B) \\ v_z(B) \end{pmatrix} = \begin{pmatrix} \frac{1}{N} \cdot \sum_{i=0}^N e_x \cdot (X(i) - \varepsilon_X) \\ \frac{1}{N} \cdot \sum_{i=0}^N e_y \cdot (Y(i) - \varepsilon_Y) \\ \frac{1}{N} \cdot \sum_{i=0}^N e_z \cdot (Z(i) - \varepsilon_Z) \end{pmatrix} \quad (6.1)$$

where  $i$  represents a voxel location within the branch segment  $B$ ,  $X$  is a function returning the scalar value at  $i$  in the PC volume scan with gradient in x-direction<sup>57</sup> and  $Y$  and  $Z$  are functions returning these values for the PC volumes with a gradient in y- respectively z-direction.  $\varepsilon_X$ ,  $\varepsilon_Y$  and  $\varepsilon_Z$  are the scalar values representing zero flow in the related PC volume data. If this data is stored in signed format this value is zero, otherwise it has to be gathered from the DICOM tags of the original data<sup>58</sup>. The parameters  $e_x$ ,  $e_y$ , and  $e_z$  are the encoding factors for the three phase contrast scans, which map the grey values to a velocity. Since the correlation between signal intensity (phase shift) and velocity is linear (compare section B.2) this factor is just a scalar and calculated by

$$e = \frac{v_{enc}}{|I_{max} - \varepsilon|} \quad (6.2)$$

as can be deduced from [36] and [8];  $v_{enc}$  is the encoding velocity described in section 2.1 and  $I_{max}$  is the grey value representing a positive<sup>59</sup>  $v_{enc}$ . Both,  $v_{enc}$  and  $I_{max}$  have to be gathered from the DICOM tags again<sup>58</sup>.

After the PC volumes have been traversed, the three vector components of all branch segments have to be divided by  $N$ , the size of the segment in voxels. The result are the average flow components of all voxels in the segment.

So far, all Cartesian coordinates referred to voxels. Although it is not completely correct to interpret voxels as cuboids, it is sufficient to apprehend them as such for the

---

<sup>57</sup> Strictly speaking, the equation assumes that the gradients of the PC-scans are orthogonal to the axes of the ROI, which is usually the case. If not, a linear transform has to be performed first, as it is described in detail in [12, 7/p.12]

<sup>58</sup> For reasons explained in chapter 2.2 this could not be done with the Ohio-data but the value had to be hard-encoded.

<sup>59</sup> A “positive” velocity means the flow direction is parallel to the gradient of the PCA scan, a “negative” velocity refers to an anti-parallel flow direction.

considerations in this thesis. The extend of a voxel in any dimension is the ratio of the metric size  $d$  of the depicted region in that dimension and the resolution  $r$  of the scan in the same direction. Any transformation from voxel space into Euclidian space can thus be performed by scalar multiplication of a scaling-vector  $\overset{i}{\theta}$  calculated according to

$$\overset{i}{\theta} = \begin{pmatrix} \theta_x \\ \theta_y \\ \theta_z \end{pmatrix} = \begin{pmatrix} \frac{d_x}{r_x} \\ \frac{d_y}{r_y} \\ \frac{d_z}{r_z} \end{pmatrix} \quad (6.3)$$

Since the special resolution of a scan can differ from dimension to dimension, the voxels represent cuboids in Euclidian space.<sup>60</sup> The Ohio-data, for example has a spatial resolution of 1 mm per voxel in x- and y-direction and 1.5 mm in z-direction.

The first application of the scaling vector  $\overset{i}{\theta}$  in the software is the scaled rendering of the flow vectors as shown in Figure 38:

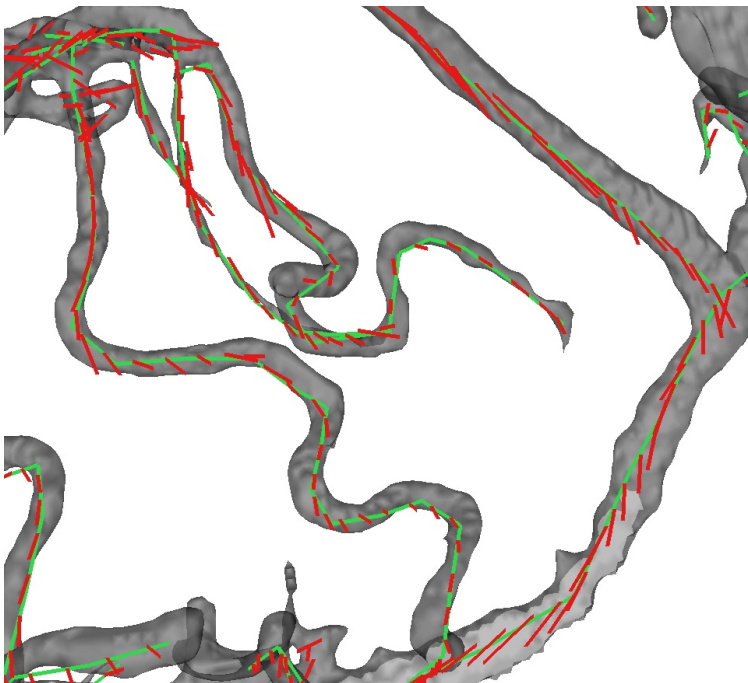


**Figure 38: Rendering of flow velocity vectors**

**Flow velocity vectors are rendered as red lines attached to the middle of the center line segments of their respective branch segments.**

---

<sup>60</sup> In practice, the scaling of the voxels has not to be calculated, but can be read from a DICOM tag.

That the velocity vectors in Figure 38 are generally not parallel to the centerline has two reasons. One is the mentioned inaccuracy of these vectors. Yet, in some areas, like the bendy vessels in the middle of the figure, the orientation reflects the course of the vessels much better than the edgy centerline. For this reason any attempt to reduce the inaccuracy of the flow vectors by projecting them onto the centerline is not advisable.

The scaling vector  $\overset{\cdot}{\theta}$  is also needed to calculate flow rates, because their computation requires knowing the average cutting area of the branch segments in Euclidian space. With the knowledge of  $\overset{\cdot}{\theta}$ , both, the metric length as well as the metric volume of the vessel segments can be calculated. The average cutting area  $A$  of a branch with length  $l$  and volume  $V$  can then be calculated by

$$A = \frac{V}{l} \quad (6.4)$$

The norm of the flow velocity vector  $|\overset{\cdot}{v}(B)|$  exhibits the effective velocity, with which blood moves through the vessel segment  $B$ . It is calculated by<sup>61</sup>

$$|\overset{\cdot}{v}(B)| = \sqrt{(v_x^2 + v_y^2 + v_z^2)} \quad (6.5)$$

Velocity is by definition

$$\overset{\cdot}{v} = \frac{d\overset{\cdot}{s}}{dt} \quad (6.6a)$$

with  $d\overset{\cdot}{s}$  being the vector of the differential change of position and  $dt$  being the differential change of time. The direction of blood flow is determined by the orientation of the vessel branch and the orientation of the branch, in turn, is given by the edge defining the branch segment and thus the length  $l$  of the segment. In other words, the blood is assumed to move along the edge<sup>62</sup>. Any position shift  $d\overset{\cdot}{s}$  can thus be interpreted as a differential change  $d\overset{\cdot}{l}$  which allows writing  $\overset{\cdot}{v}$  as

$$\overset{\cdot}{v} = \frac{d\overset{\cdot}{l}}{dt} \quad (6.6b)$$

---

<sup>61</sup> See [30, p.177].

<sup>62</sup> Figure 38 shows that the flow velocity vectors of the branch segments are not perfectly aligned with the centerline. One reason for this is that the centerline segments go straight through the branch segments, not following their bend but the major reason has to be seen in inaccuracies of the flow data.

Flow rate  $Q$  is defined as

$$Q = \frac{dV}{dt} \quad (6.7)$$

with  $dV$  being the differential interchange of volume.

Conversion with (6.4) and insertion of (6.6b) leads to

$$Q = \frac{A \cdot ds}{dt} = A \cdot v \quad (6.8)$$

In combination with the topological information of the abstract vessel tree this flow rate data does suffice to perform all the operations proposed in section 3.3.

## 6.2 Processing of the Flow Data

For data visualization five 3D surface objects are computed, one displaying absolute flow velocities, three to visualize the flow velocities component-wise in all orthogonal directions and another one to visualize flow rates. These surface objects are created from the segmentation result and colored by employing the lookup table described at the end of section 5.2 again. All voxels of the 3D surfaces are traversed and the corresponding branch segments are queried from the lookup volume. Again the indexed map is used to access the associated segment data object, but this time as a data source, not to assign a value to it. Depending on the type of data to be visualized, the value of either the norm of the flow velocity vector, or one of the vector components, or the flow rate of the branch segment are read from the object, mapped to a suitable color value<sup>63</sup> and assigned to the surface voxel.

Three of these surface objects, the one showing flow rates, the one depicting flow velocities and the one visualizing the sagittal component of the flow velocities are given in Figure 39.

---

<sup>63</sup> For this task, the minimal and maximal values of the five different kinds of flow data are determined. This allows to map all occurring scalar values to a predefined color range.

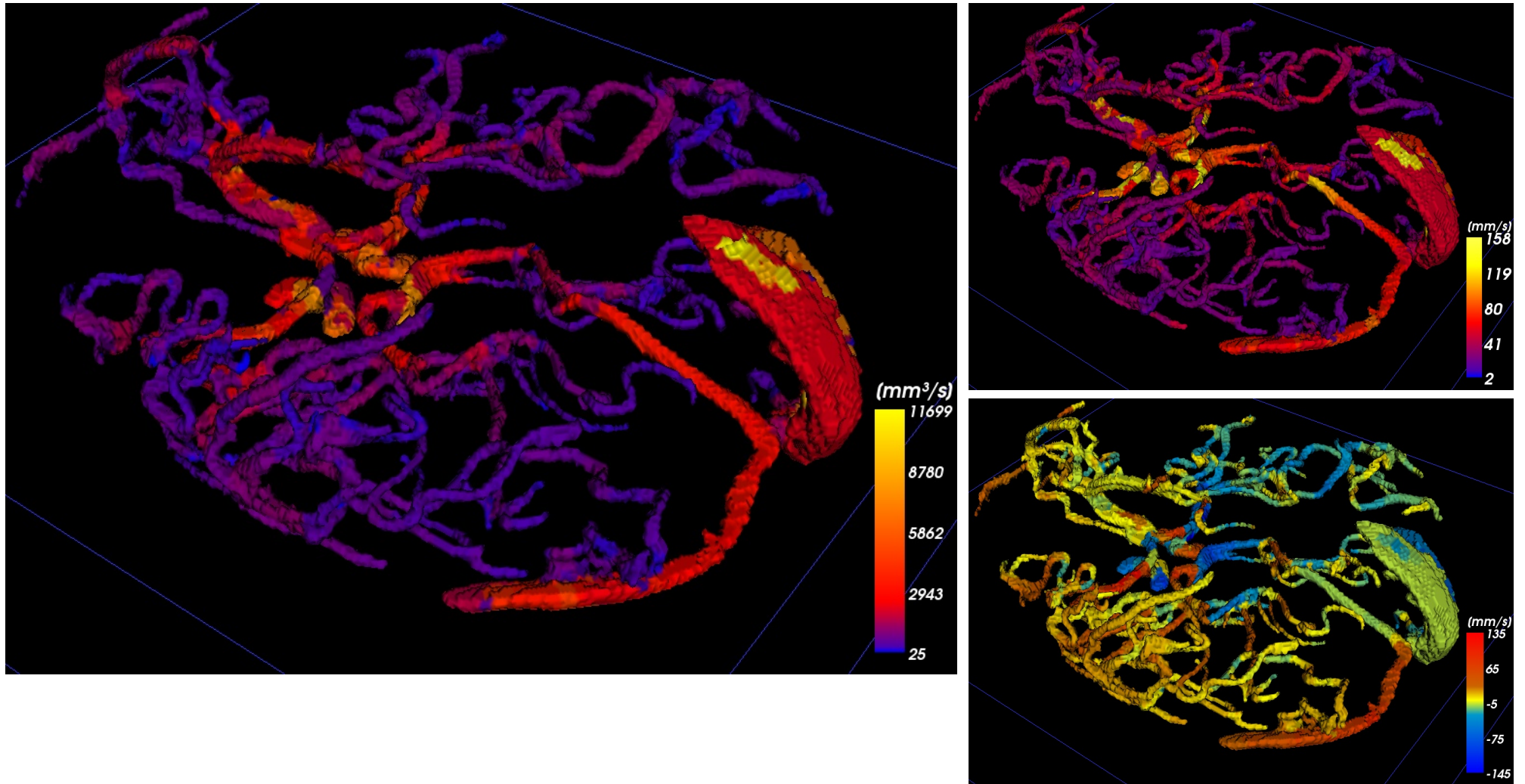


Figure 39: Visualization of flow quantities - left: flow rates; right, top: flow velocities; right, bottom: sagittal component of the flow velocity

The visualization of the flow data already allows some examinations. For example, the sagittal flow velocity data features a left-right partition as it is to be expected considering the topology of the cranial vessels with all feeding arteries positioned medial<sup>64</sup> and the draining sinus traverses running from the middle outwards. The flow rates for instance are highest in the large sinus and the feeding carotids and the arteria basilaris as to be expected.<sup>65</sup> Thus, major inconsistencies of the data would already show up in these visualizations.

A closer look at the visualization of the flow rates, however, also reveals fluctuations even in unbifurcated branches. These fluctuations will be subject to thorough examination in the next chapter, but such examinations demand better evaluation methods than mere visualization.

A thorough analysis requires the sampling of flow data at selected vessel segments as well as throughout a whole range of subsequent branch segments, hence called a branch section. Both, the selective sampling of the flow at a certain position in the vessel tree as well as the selection of start- and endpoint of the examined branch section are performed by user interaction with the 3D surface model of the flow rates.

The selection of a single branch segment in order to probe flow rate and flow velocity in this segment is triggered by moving the mouse over the 3D model. The two dimensional mouse point coordinates can then be converted into rendering window coordinates and a VTK-function returns the three dimensional coordinates of the closest<sup>66</sup> voxel of the 3D surface model, which is rendered to these window coordinates. The lookup of the flow data associated with this sample point is performed in the same way, the surface models were colorized. To trigger the analyses of a whole branch section, the start- and endpoint of this section are selected by two double-clicks.

To calculate the path from the selected branch segment defining the beginning of the section to the other segment defining the end of the section, priority search is used

---

<sup>64</sup> I.e. centered.

<sup>65</sup> Please, refer to appendix A for an overview of cranial vessel anatomy.

<sup>66</sup> Due to the possibility of semi transparent rendering, there could more then one voxels of the surface be mapped to the same pixel.

again. Since it cannot be said in advance, which nodes might become part of the path, all nodes have to be taken into account, which can possibly be expected to become part of this path. This means that, starting from the first sample point, all vessel nodes connected to it have to be added to the priority queue. The same is true for any node processed in the following iteration steps. This time, however, computational complexity can be much better reduced, since there are usually no more than two or three edges connected with each node. Since all edges are known in advance, only the distances of those nodes have to be updated, which share an edge with the node, which has just been added to the tree. This reduces the computational complexity for the creation of a minimal spanning tree to  $O(N \cdot \log(N))$  [31, p. 527]. To deduce the (shortest) path<sup>67</sup> between the selected branch segments from this minimal spanning tree, every new node is stored together with a reference to the edge by which it has been connected to the minimal spanning tree. By this means, the shortest path can be found via backtracking, starting at the end of the path. The preceding node in the path is always the one at the other end of the stored edge.

Numerous properties of the branch segments in such a section can be evaluated by the software. First of all, flow rates along the branch section can be investigated. Figure 40 for example shows the flow rates along an unbifurcated part of the sinus rectus.

---

<sup>67</sup> Since a vessel tree should not contain loops, there should always exist only one path, from one segment to another. This path would naturally be the “shortest” path. Due to the segmentation flaws described in chapter 4.3, the abstract vessel tree, however, does contain loops and thus there often would exist multiple paths between two segments.



**Figure 40: Flow rates along a section of the sinus rectus**

Apart from the flow rates also the change of flow rate along the section is determined for later analysis. A change in flow rate along a section is in general

$$\frac{dQ}{ds} \quad (6.9a)$$

with  $dQ$  being the differential change of flow rate and  $ds$  the differential displacement again. For discrete data, the change in flow rate is calculated by

$$\frac{\Delta Q}{\Delta s} \quad (6.9b)$$

where  $\Delta Q$  is the change in flow rate from one segment to the next. The discrete displacement  $\Delta s$  equals to the length of the examined segment.

The angles a vessel encloses with the gradients of the PCA scans are investigated as well, since one approach of this thesis is to examine the influence these angles have on the measured flow rates.

Since the accuracy of the PCA data is highest, if the vessel is parallel to a gradient, the smallest (i.e. best) angle  $\alpha_{min}$  is investigated. The basic idea is that if the vessel is parallel to one of the gradients, the data from the PCA scan with this gradient should be reliable, while the other PCA scans should not supply any flow components at all. Thus, a small  $\alpha_{min}$  should result in reliable scan data. Large deviations of  $\alpha_{min}$  on the other hand most probably result in large deviations from the true flow velocities. The discrete derivation of  $\alpha_{min}$  is (in analogy to 6.9b)

$$\frac{\Delta\alpha_{min}}{\Delta s} \quad (6.9c)$$

Investigating the largest angle would be equivalent, since a large intersection angle with one of the orthogonal gradients automatically results in a small intersection angle with another gradient. For similar reasons, an average intersection angle could not deliver valuable information, since this average angle holds no information about angular miss alignment. A perfect alignment to one of the axes, for example, leads to an average angle of  $60^\circ$ , resulting from one intersection angle of  $0^\circ$  and two of  $90^\circ$  with the other orthogonal axes. The same average angle, however, is the outcome if the vessel encloses an angle of  $45^\circ$  with two of the axes and  $90^\circ$  with the third one.

Similar considerations as for the flow rates and minimal intersection angles apply to any changes in flow rates and minimal intersection angles, because a drastic change of  $\alpha_{min}$  should become notable in a significant change in the flow rate as well.

These Figures allow significant evaluations as they will be the subject of the next section.

### 6.3 Analysis of Flow Rate Changes Along a Selected Branch Section

Draining or feeding vessels along the selected branch section cause a sudden raise or drop of flow rates at the bifurcations. This effect is expected and can be compensated as by limiting samples to unbifurcated branch sections. Thus, all sampled vessels can be treated as unbifurcated without loss of generality.

Yet, in the Ohio-data even unbifurcated vessels pose fluctuations of both, flow rates and flow velocities, as can be gathered from the figures 39 and 40.

While fluctuations of the flow velocities along a vessel could be caused by changes in the vessel diameters, a change in flow rates can only be caused by pulsatile effects. If these pulsatile effects were compensated during data acquisition as demanded in section 2.2, the reason for these fluctuations can only be seen in inaccuracies of the flow data. Apart from missing compensation of pulsatile effects, the only parameter, which can

possibly cause a varying<sup>68</sup> distortion in the PCA scan results, are angular misalignments as described in section 2.2 as well. Hence, it has to be checked whether such misalignments are the cause of the observed fluctuations.

The analysis of the flow rate at a branch segment does not allow making any assertions concerning accuracy of this data sample. Even if the flow rate in the sampled branch segment differs significantly from the flow rates of the feeding and draining segments, this incongruity could be caused by inaccuracies concerning these other segments. Nonetheless, assertions about the influence of  $\alpha_{min}$  on the accuracy can be made. If inaccuracies are caused by immoderate minimal intersection angles (as was put forward at the end of the previous section already) a constant  $\alpha_{min}$  should result in constant flow rates in an unbifurcated branch, because any flaw caused by misalignment of the vessel with respect to the gradients should remain constant then as well. Thus there has to exist either a positive or negative correlation between flow rates and  $\alpha_{min}$ . The same applies to any change in flow rates as calculated by (6.9).

The correlation between two sets of variables  $X$  and  $Y$  is determined by means of the correlation coefficient  $\sigma(X, Y)$ , which is by definition [19, p. 201]

$$\sigma(X, Y) = \frac{\text{cov}(X, Y)}{\sigma_x \cdot \sigma_y} \quad (6.10a)$$

where  $\sigma_x$  and  $\sigma_y$  are the standard deviation of  $X$  and  $Y$  and  $\text{cov}(X, Y)$  is the covariance which is defined as

$$\text{cov}(X, Y) = E[(X - E[X]) \cdot (Y - E[Y])] \quad (6.10b)$$

with  $E[ ]$  being the expected value operator.

For series of measurement (i.e. samples), the covariance is computed by [19, p.198]

$$\frac{1}{n} \cdot \sum_{i=1}^n (x_i - \bar{x}) \cdot (y_i - \bar{y}) \quad (6.10c)$$

---

<sup>68</sup> Failures in the PCA flow data can, of course, have many causes, but flaws due to faulty scan parameters would occur uniformly distributed over the whole scan volume and not cause fluctuations.

and the standard deviation of X according to

$$\sqrt{\frac{1}{n} \cdot \sum_{i=1}^n (x_i - \bar{x})^2} \quad (6.10d)$$

with n being the number of samples and  $x_i$  and  $y_i$  being a single sample value;  $\bar{x}$  is the mean of X [19, p.198]. The standard deviation of Y is computed likewise.

The result of inserting (6.10c) and (6.10d) into (6.10a) is the Pearson product-moment correlation coefficient  $r_{x,y}$  [19, p.199]:

$$r_{x,y} = \frac{\frac{1}{n} \cdot \sum_{i=1}^n (x_i - \bar{x}) \cdot (y_i - \bar{y})}{\sqrt{\frac{1}{n} \cdot \sum_{i=1}^n (x_i - \bar{x})^2} \cdot \sqrt{\frac{1}{n} \cdot \sum_{i=1}^n (y_i - \bar{y})^2}} \quad (6.10e)$$

The correlation coefficient allows verifying if the fluctuations of flow rates in the unbifurcated branch as visible in Figure 40 are the result of angular misalignments of the vessels.

## 6.4 Results of the Flow Rate Evaluation

If a correlation exists, it is justified to either substitute flow rates in badly aligned branch segments with values of well aligned segments as proposed in the approach of section 3.3, or to even find out a corrective factor, which allows deducting the flaw in flow data caused by angular misalignments as it is subject of section 3.4.

The course of flow rates and minimal intersection angles along six sampled branch sections are depicted in the following. Figure 41 shows the location of the samples with regard to the cranial vessel tree and Figure 42 displays the associated six diagrams of flow rates and minimal intersection angles. For two of the samples number 2 and number 5) the discrete derivations of flow rate (compare equation (6.9b)) and the discrete derivations of the minimal intersection angle (equation (6.9c)).

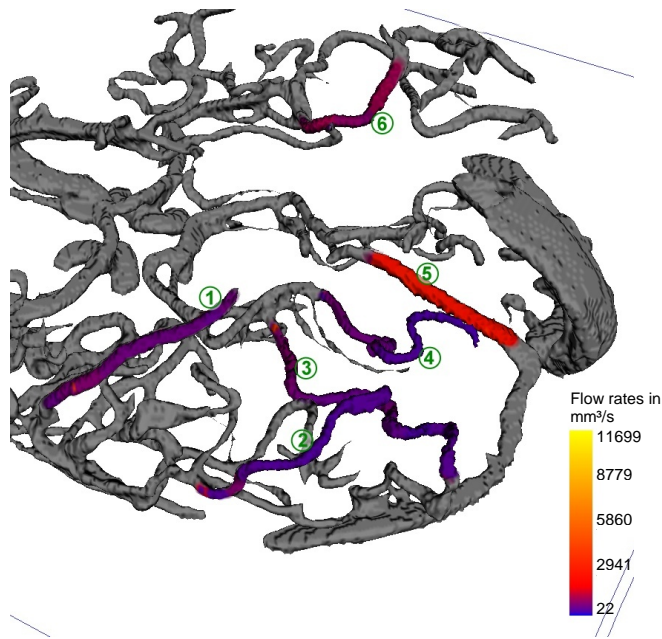
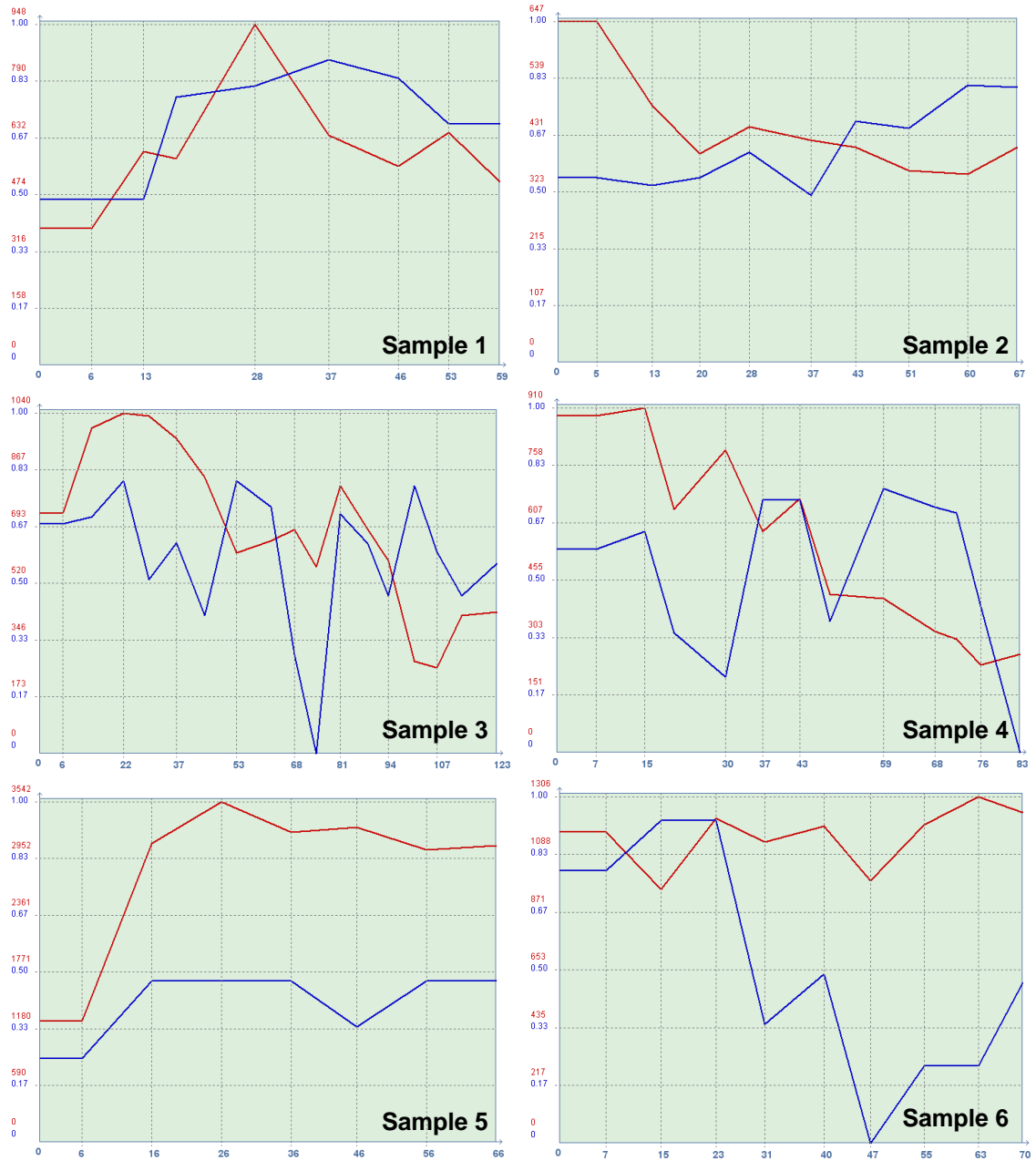
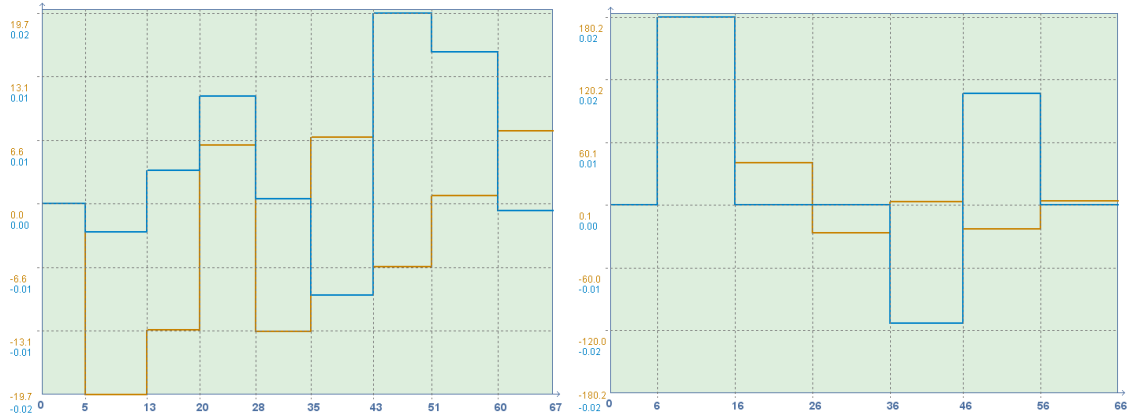


Figure 41: Location of six branch sections selected for flow evaluation



**Figure 42: Flow rates and minimal intersection angles of the six sampled branch sections displayed in Figure 41**

The abscissas give the position in the branch section in mm, the ordinates the flow rate in mm<sup>3</sup> per second (red lines) and the minimal intersection angle in radians (blue lines).



**Figure 43: Changes in flow rates and change of the minimal intersection angles of the samples 2 and 5 from Figure 41**

The abscissas give the position in the branch section in mm, the ordinates the changes of flow rate per mm in  $\text{mm}^2/\text{s}$  (orange line) and the change of the minimal intersection angle per mm in  $\text{rad}/\text{mm}$  (blue line).

The six examined branch sections consist of 62 branch segments. The correlation for these 62 samples are  $r_{Q, \alpha_{\min}} \approx -0.20$  and  $r_{\frac{\Delta Q}{\Delta s}, \frac{\Delta \alpha_{\min}}{\Delta s}} \approx 0.17$ .

Since correlation values around zero imply that the compared variables are not related with each other [19, p.199], the angular misalignment cannot be the cause of the fluctuations.

Yet, other explanations than angular misalignment for the high fluctuations of the values have to remain speculative, considering the limited data foundation. Plausible reasons can be given for some of the more noticeable leaps. The low flow rate at the beginning of sample 5, for example is probably caused by an artifact in the flow data which is shown in Figure 51. The cause of this artifact is explained in appendix B.2. And the drop of the flow rates in sample 4 seems to be caused by two small draining segments, which did not become part of the segmentation, but can be guessed from two tiny stubs on the vessel surface.

But even if these leaps are manually excluded from the determination of the correlation coefficient, the results do not significantly change. After removing the 10 segments with

the highest changes in flow rate, the resulting Pearson product-moment correlation coefficients are  $r_{Q, \alpha_{min}} \approx 0.11$  and  $r_{\frac{\Delta Q}{\Delta s}, \frac{\Delta \alpha_{min}}{\Delta s}} \approx 0.30$ .

Again these correlations are unsatisfactory. Since all other possible causes have been ruled out, data inconsistency is the only possible cause for the fluctuations in the unbifurcated branches. These most likely originate from the fact, that no heart beat triggering was performed during the scan of the Ohio-data as it has been explained in section 2.2. As a consequence, every slice of the PCA volumes has been recorded in a random phase of the heart beat. This assumption is corroborated by the fact that the fluctuations of flow velocities in the sinus is lesser than in the arteries as can be seen on the right side of Figure 39 in the top image. This is to be expected, since blood flow in the veins is less pulsatile than in the arteries [8, p.679].

These results are disappointing with regard to the application of the two major improvement approaches, proposed in sections 3.3 and 3.4. Both, the conditioning of flow data in segments which have to be considered unreliable as well as the deduction of a corrective factor to compensate for misalignments of the vessels with regard to the PC-gradients, rely on the consistency of the scanning results. For this reason these approaches could not be implemented in the course of this thesis.

## 7 CONCLUSIONS

A novel method has been devised in the course of this thesis, which allows performing QMRA analysis more efficiently. So far technical limitations of PCA make it necessary to perform QMRA examinations in two steps. One planning step which involves an anatomical scan and the actual PCA scan itself. The new method requires one scanning session only. It consists of two approaches:

First, the necessity for an anatomical scan for segmentation is evaded by performing the segmentation of the vessel lumen directly on the PCA data.

Furthermore, the necessity of planning the quantitative scan is eliminated. So far it is the proceeding to define slices for the PCA scan on the basis of an anatomical scan performed before. This inefficient workflow is avoided by creating an abstract model of the vessel tree, which allows associating the flow data with the topological information from the tree. Hereby the technical limitations of PCA can be taken into account which allows increasing the overall reliability of the flow data throughout the vessel lumen. In theory the resulting flow data should be equal in quality to the data measured in pre-planned slices in every section of the vessel tree. However, comparative studies would be necessary to prove this assumption but such studies would go beyond the scope of this thesis.

Apart from the simplified and time saving workflow, the approach also provides more comprehensive data than the previous method, since it delivers flow information for the whole lumen and not only for some selected slices.

Acquisition of the PCA volume data as it is required for the issues of this thesis, unfortunately, proved difficult. Until the end of this work, only one dataset became available. Yet, this dataset posed inconsistencies. For this reason the second approach could only be investigated as far as it concerned the creation of the abstract vessel tree and the analysis of the data. However, it was not feasible to examine any methods which might allow effacing inaccuracies and thus optimizing the flow data throughout the whole vessel tree.

Nonetheless, it can be regarded as a success that the implemented software disclosed the inconsistencies in the data. It has thus proved capable to immediately detect such inconsistencies, which is already a valuable application in itself.

All future work that will be carried out in order to continue this work will rely on the acquisition of reliable data. With regard to the increasing number of clinical applications for PCA techniques, PCA volume scans can be expected to become available more easily than today. A solid data foundation would allow pursuing the promising approaches introduced with this work.

It also seems to be a promising idea to use the results of the flow analysis to improve the segmentation results. Since segmentation faults have a severe impact on the flow analysis, as it turned out during the course of this thesis, the latter could be utilized to detect and correct such faults. In turn, this would have a positive effect on the quality of the flow analysis. Such a mutual improvement could significantly enhance the overall results of both, segmentation and flow analysis as performed by the QMRA software.

## Appendix A: Anatomy of the Cranial Vessel Tree

The processing results of some steps like segmentation or centerline extraction can be best explained by screenshots of their rendering results. To draw the readers attention to some anatomical structures where the respective step can be best understood it is sometimes necessary to name these anatomical structures. Therefore some of the most important cranial vessels are given below as they can be found in either Sobotta's Anatomical Atlas or Netter's Atlas of Clinical Anatomy. These structures will be indicated in the segmented Ohio data as well for easier orientation.

The most important veins<sup>69</sup> visible in the Ohio data are sinus sagittalis superior, sinus transverses, and sinus rectus:

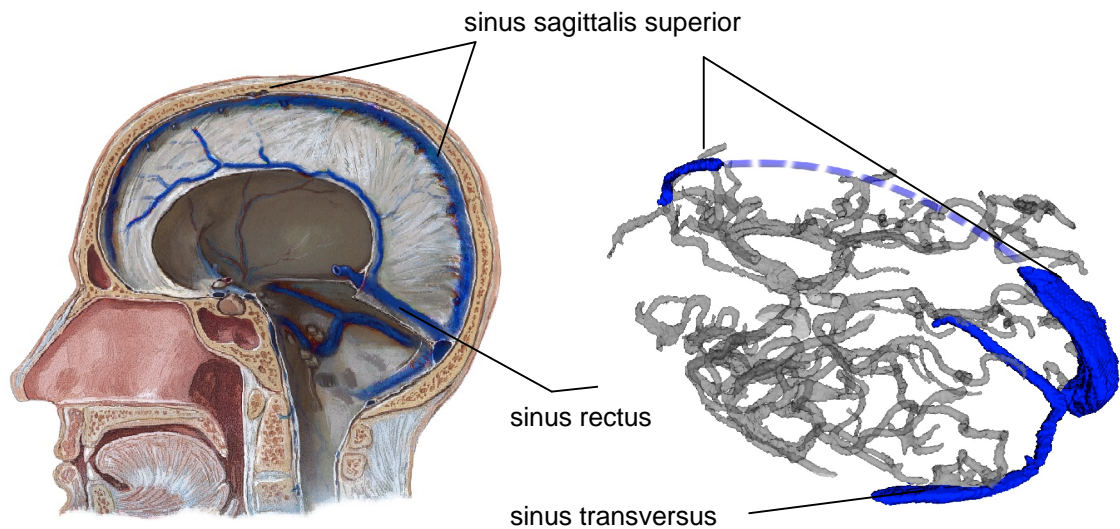


**Figure 44: The major cranial veins**

**left: anatomical illustration from [22]; the sinus transverses are not depicted**

**right: segmentation result from the Ohio data. (The upper part of the sinus sagittalis superior (dashed line) is outside the data volume; only the left sinus transversus is visible)**

<sup>69</sup> Strictly speaking these vessels are not the same type of veins as they can be found in other body parts but venous channels between layers of the meninges.

The most important arteries visible in the Ohio data are: arteria cerebri anterior, arteria communicans anterior, carotis interna, arteria cerebri media, arteria cerebri posterior, arteria superior cerebelli and arteria basilaris.

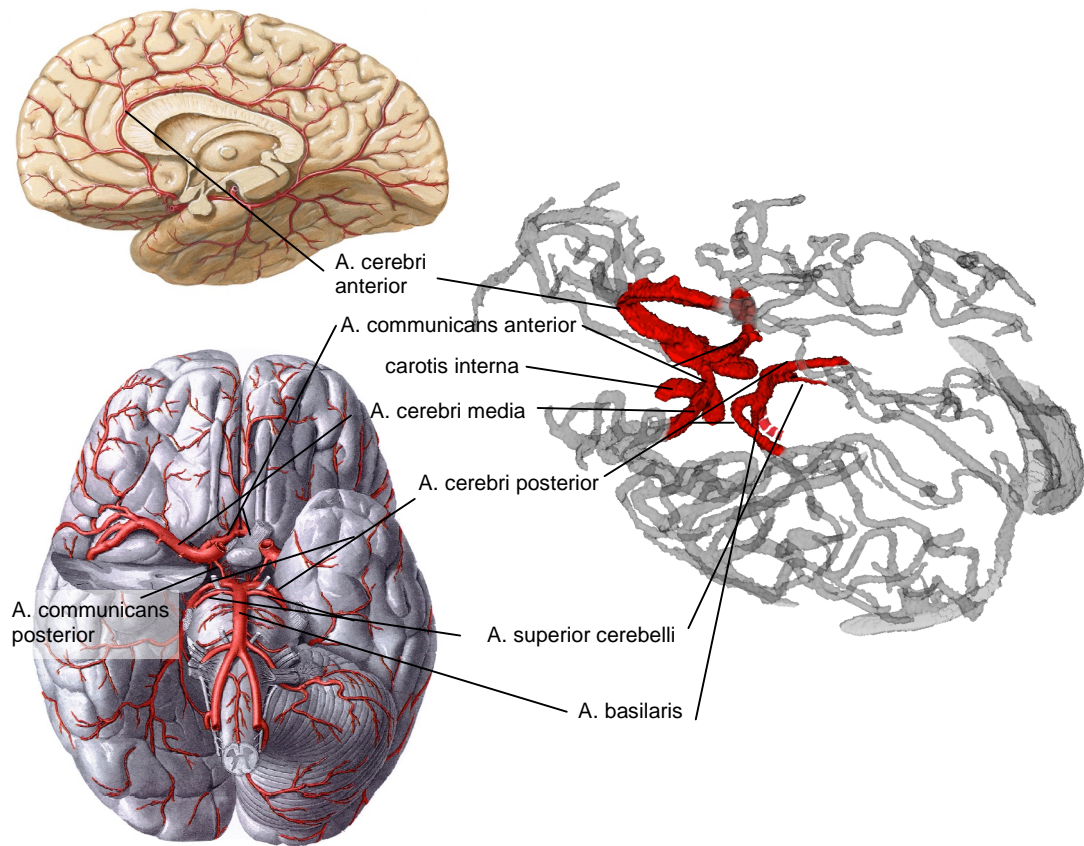


**Figure 45: The major cranial arteries (as far as visible in the Ohio data)**

**left, top: illustration of the medial view from [22]**

**left, bottom: arteries of the brain as seen from below from [32]**

**right: segmentation result from the Ohio data. (the arteria basilaris (dashed line) is nearly completely outside the data volume; the carotis interna is not pictured in the anatomical illustrations, the diameter of the arteria communicans posterior – completing the circulus arteriosus cerebri<sup>70</sup> – is below the resolution of the scan and could thus not be segmented.)**

<sup>70</sup> The circulus arteriosus cerebri (also called Circle of Willis) is a circular structure, connecting the arteria basilaris and the two arteriae carotis internae among each other).

## Appendix B: MR Fundamentals

### B.1 Physical Fundamentals of MRI

#### B.1.1 Magnetic Moment and Spin

As described by Maxwell's equations, a moving charge carrier generates a magnetic field. In the simplest case of an electric conductor loop carrying a current  $I$  the magnetic moment  $\mu$  is yielded by<sup>71</sup>

$$\mu = I \cdot A \quad (\text{B.1})$$

thus the product of the current and the area circum-flown by this current. Consequently the unit of the magnetic moment is  $\text{A} \cdot \text{m}^2$ .

As, according to the Bohr Model, the shell electrons are moving on a circular course around the nucleus, it has been assumed at the beginning of the last century already that even an outwardly resting atom is supposed to possess a magnetic moment. Since Bohr had already postulated that the course impulse of the electrons has to be quantized<sup>72</sup>, the magnetic moment was expected to be quantized as well. In 1920 the experimental physicists Otto Stern and Walter Gerlach proved atoms have in deed a magnetic moment and this is quantized as expected. A surprising result of this experiment becoming famous as Stern-Gerlach-Experiment, however, was that even those atoms in which the magnetic moments of the shell electrons are supposed to annihilate each other, pose a magnetic moment. Hereof could be concluded (and experiments within the same decade proved this) that nuclei as well as the elementary particles of which they consist possess a magnetic moment.

It is an explanatory model for this effect, to (in analogy to the orbital angular momentum of the electrons) assume an intrinsic angular momentum<sup>73</sup> of these (electrically charged) particles around their own axis. An image, which also appropriately describes numerous

---

<sup>71</sup> All equations and formulas are taken from [17] if not said otherwise.

<sup>72</sup> The postulation for quantization was necessary to explain why electrons do on certain paths not use up their kinetic energy by emitting electromagnetic radiation, as it would be to expect in a macroscopic system.

<sup>73</sup> The image of an elementary particle as a little ball spinning around its axis does of course not match reality and is inconsistent with numerous experiments. For the effects describing magnetic resonance behavior, as they are relevant for this chapter this conception is, however, totally sufficient.

other experimentally observable quantum phenomena. This quantized intrinsic angular momentum is denoted as spin  $\overset{\circ}{S}$  and the associated magnitude of this momentum is calculated according to

$$\overset{\circ}{S} = \hbar \cdot \overset{\circ}{s} \quad (\text{B.2})$$

Since the magnetic moment can be interpreted as a direct result of this angular momentum, it is proportional to it and thus can be expressed as the scalar product

$$\overset{\circ}{\mu} = \gamma \cdot \overset{\circ}{S} \quad (\text{B.3a})$$

with  $\gamma$  being a constant for every nucleus.

The constant of proportionality  $\gamma$  is called gyromagnetic ratio and is characteristic for every chemical element. Written like

$$\gamma = \frac{\overset{\circ}{\mu}}{\overset{\circ}{S}} \quad (\text{B.3b})$$

the unit of the gyromagnetic ratio follows from

$$\frac{\frac{A \cdot m^2}{kg \cdot m^2}}{s \cdot (rad)} = \frac{A \cdot s}{kg} \cdot (rad) = \frac{1}{T \cdot s} = \frac{Hz}{T} \quad (\text{B.3c})$$

For a single proton (i.e. a hydrogen nucleus) it amounts to 42.577 MHz/T [28, p. 436].

### B.1.2 Potential energy of the nucleus in an external magnetic field

Since the magnetic moment acts perpendicular to the rotational axis of the proton, this leads to a deflection of the rotational movement along the direction of the external magnetic field  $B_0$ .

Therefore the proton performs a precession in addition to its rotation around the axis, akin to a spinner deflected by a magnet.

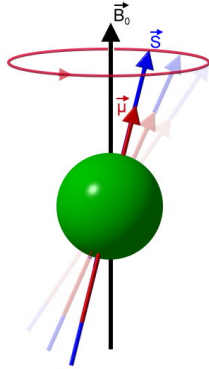


**Figure 46: Precession of a proton along the direction of the external magnetic field**

The frequency  $\omega_0$  of this precession depends on the ratio of the angular moment given by

$$\overset{\cdot}{M} = \overset{\cdot}{\mu} \cdot \overset{\cdot}{B}_0 \quad (\text{B.4a})$$

to the magnitude of the intrinsic angular momentum  $S$  leading to the equation

$$\omega_0 = \frac{\overset{\cdot}{M}}{S} = \frac{\overset{\cdot}{\mu}}{S} \cdot \overset{\cdot}{B}_0 = \gamma \cdot \overset{\cdot}{B}_0 \quad (\text{B.4b})$$

In analogy to a bar magnet aligned in an external magnetic field the potential energy  $E_m$  of an elementary particle in an external magnetic field  $\overset{\cdot}{B}_0$  with magnitude  $B_0$  amounts to

$$E_m = -\overset{\cdot}{\mu} \cdot \overset{\cdot}{B}_0 = -\gamma \cdot S \cdot \overset{\cdot}{B}_0 = -\gamma \cdot s \cdot \hbar \cdot B_0 \quad (\text{B.5a})$$

As already explained, the spin of an elementary particle is quantized and can only adopt certain values. For a proton these values are  $+1/2$  and  $-1/2$ . Hence, the potential energy of a proton in an external magnetic field amounts to

$$E_m = \gamma \cdot \pm \frac{1}{2} \cdot \hbar \cdot B_0 \quad (\text{B.5b})$$

Accordingly the anti-parallel alignment of a previously parallel-aligned proton in an external magnetic field requires the energy amount of  $\gamma \cdot B_0$  electronvolts and the contra wise procedure discharges this amount of energy in the form of electromagnetic radiation.

It might be mentioned that the nuclei at room temperature do not, in an effort to reach the most favorable (i.e. energetic lowest) state, as expected align parallel to the external magnetic field, but that in fact the energy difference in question is too marginal compared with the environments thermal energy to preponderate. A near equipartition of the parallel and anti-parallel state is the result.

According to the Boltzmann distribution the ratio  $p_1$  to  $p_2$  for the occupation of these energy levels is determined by

$$\frac{p_1}{p_2} = e^{\left(\frac{E_2 - E_1}{kT}\right)} \quad (\text{B.6a})$$

For a temperature of 20° Celsius (293.15 °K) the distribution for hydrogen nuclei in an external field with a strength of one Tesla calculates as

$$\frac{p_1}{p_2} = e^{\frac{\gamma \cdot \hbar \cdot B_0}{k \cdot T}} = e^{\frac{42,577 \frac{\text{MHz}}{\text{T}} \cdot 1,0545 \cdot 10^{-34} \text{ Js} \cdot 1\text{T}}{1,3807 \cdot 10^{-23} \frac{\text{J}}{\text{K}} \cdot 293,15 \text{ K}}} \approx 1,000\,001\,109 \approx 1 + \frac{1}{900.000} \quad (\text{B.6b})$$

or, to express it in different words: there are about one million anti-parallel and a million plus one parallel aligned protons<sup>74</sup> in two millions within a field of one Tesla strength. Nevertheless, in one milliliter of water (roughly  $3 \cdot 10^{19}$  molecules) there is still an excess of about 15 trillion parallel-aligned protons.

To cause the protons to emit a measurable signal it is necessary, as described in equation (B.5b) to excite them onto a higher potential. Since only the parallel and exactly anti-parallel state are quantum mechanically permitted, this must happen by a light quantum of the precisely right energy and thus precisely right frequency as described by Planck's law

$$E_p = \hbar \cdot \nu \quad (\text{B.7a})$$

---

<sup>74</sup> Henceforth the words proton and hydrogen nucleus are used synonymously, since heavy hydrogen isotopes, consisting of one or two additional neutrons, amount to only less than two per mille of the body's hydrogen and can thus be neglected.

According to

$$\Delta E_m = 2 \cdot \gamma \cdot \pm \frac{1}{2} \cdot \hbar \cdot B_0 = \gamma \cdot B_0 \cdot \hbar = \nu \cdot \hbar = E_p \quad (\text{B.5c})$$

the frequency  $\nu$  of the incitation pulse has to amount to  $\gamma \cdot B_0$ . This frequency is called Larmor frequency and with respect to its property to incite nuclei precessing with this same frequency to precess with a higher (i.e. energetic positive) potential is also called resonance frequency. The radiation emitted in response to the excitation pulse is called (spin) echo.

### B.1.3 Semi-classical Description of a Multi-Proton-System.

Despite only the parallel and anti-parallel state being allowed for a proton's spin, the image of the proton as a rotating spinner can be quite well applied as far as the longitudinal magnetization (i.e. the magnetization parallel to the external magnetic field) is concerned. This direction will be referred to as z-axis by definition. This is possible when a whole ensemble<sup>75</sup> of protons is described, since in thermal equilibrium the vectors of all angular momentums (i.e. spins) behave in their sum equally to such a simple system.

For the measurable reaction of the system to an external excitement only the excess of parallel spins present in thermal equilibrium are of interest and will therefore solely be examined in this chapter. The majority of those nuclei of which the magnetic moments annihilate each other can be neglected without loss of validity. Figure 47 illustrates this applicability of the classical model.

---

<sup>75</sup> In quantum mechanics a group of equally prepared particles is called an ensemble.

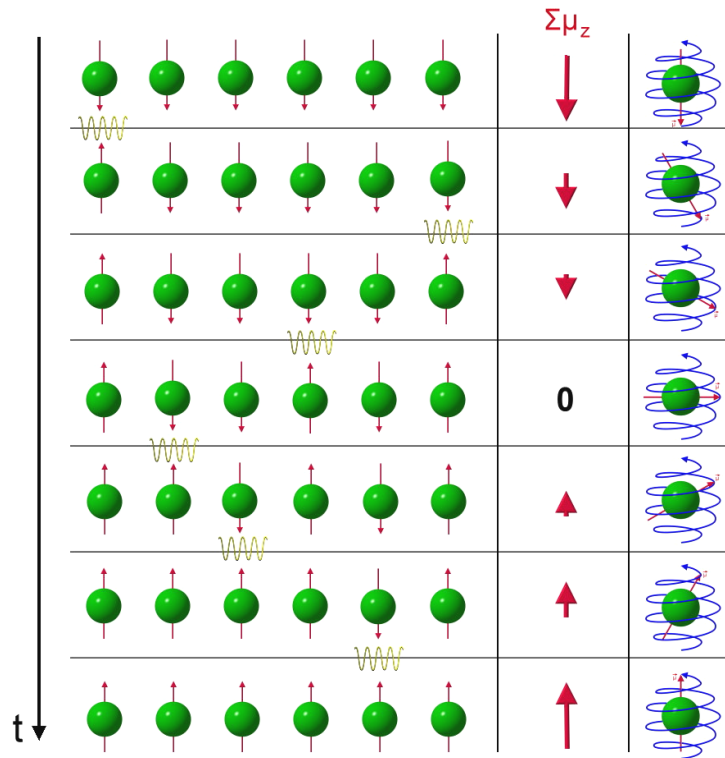


Figure 47: Classical interpretation of the longitudinal magnetic moment

The ensemble of the protons initially incited to the anti-parallel state by a EM-pulse of the frequency  $\nu = \omega_0$  (left column) sums up to a primarily maximal anti-parallel momentum (center column); by emitting electromagnetic radiation of the Larmor frequency these fall back to the parallel state over the time  $t$ ; altogether (for a sufficiently large ensemble) the observable magnetic moment in z-direction resembles a classical, non quantized system (right column).

The velocity with which the hydrogen nuclei return to the thermal equilibrium is called relaxation time. As far as it concerns the longitudinal magnetization it only depends on the strength of the external magnetic field and how easily they can dispense the released energy to the surrounding atomic grid [28, p. 14]. If the grid does not immediately absorb the emitted photon, it incites another nucleus again to the anti-parallel state, thus delaying the relaxation time. The longitudinal relaxation time is therefore called spin-grid-relaxation-time or T1.

In longitudinal direction (which will be referred to as xy-direction henceforth) such a system cannot be described like a classical system. A pseudo-classical behavior can, however, be achieved by external means: by applying an external magnetic field  $B_I$

rotating perpendicularly around  $B_0$  with the Larmor frequency  $\omega_0$  a longitudinal magnetic moment can be induced.

Naturally, the intention of such a proceeding is not simply to achieve a classically describable bearing, since no advantages concerning image acquisition could be derived thereof. Purposeful it is, however, since the surrounding tissue provides a small magnetic field itself, which adds to the external  $B_0$  field. Since, according to equation (B.4b) a difference in the external field results in a change of the precession frequency, causing nuclei to run out of phase depending on the strength of the local magnetic field, a dephasing results from local field inhomogeneities. [28, p.15] This dephasing affects only the longitudinal magnetization adding a valuable second component holding information about tissue properties to the spin echo.

Since those local field inhomogeneities are generated by the spins of the elementary particles in the surrounding, the relaxation time related to this phenomenon is called spin-spin-relaxation-time or T2. Table 1 lists some relaxation times of typical tissues:

Tissue	T2 [ms] at 1.5 Tesla	T1 [ms] at 1.5 Tesla
Skeletal muscle	47 ± 13	870 ± 160
Cardiac muscle	57 ± 16	870 ± 140
Liver	43 ± 14	500 ± 110
Kidney	58 ± 24	650 ± 180
Fat	84 ± 36	260 ± 70
Gray matter	101 ± 13	920 ± 160
White matter	92 ± 22	790 ± 130

**Table 1: Relaxation times of different tissues [28, p. 17]**

## B.2 Phase-Contrast MR

Protons moving through the examined slice (usually in the form of hydrogen nuclei in the flowing blood) have some often undesired effects on the MR signal, causing motion artifacts. This undesired effects can, however, be utilized in order to measure blood flow. Especially one technique, called phase contrast angiography has proven useful for such tasks.

As the name already implies, the velocity of the protons is determined from the differences of their phase. That an external magnetic field causes a shift in the phase of the magnetic moments (spins) of protons was elaborately explained in the previous chapter. To induce a difference (contrast) in the phase it is sufficient to apply a magnetic gradient in the vicinity of the examined slice:

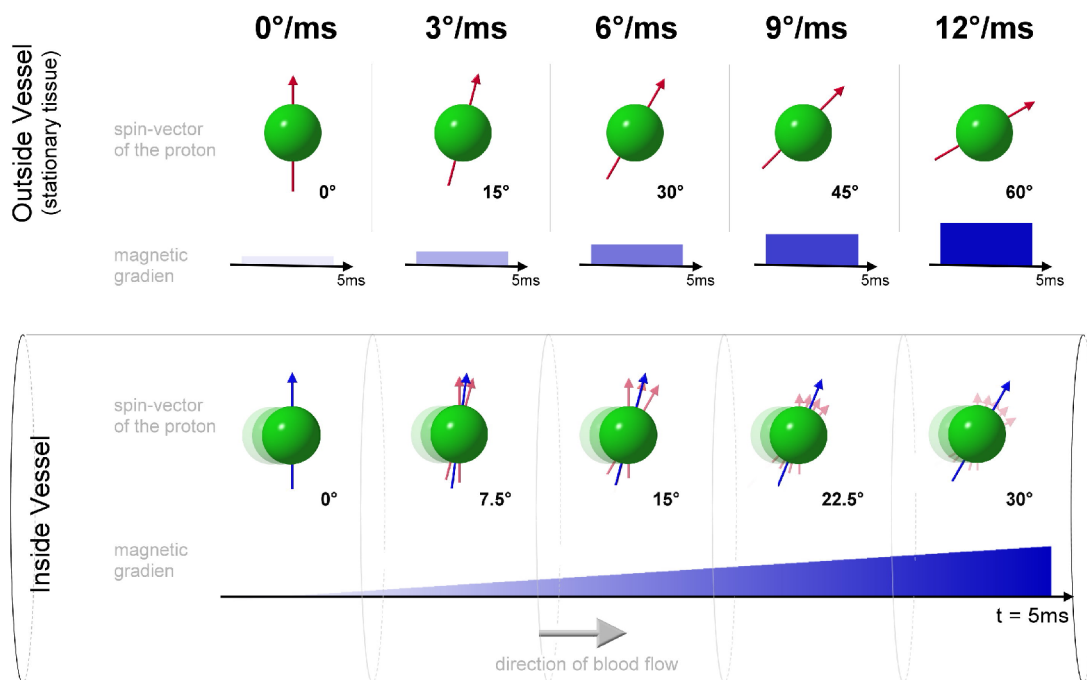


**Figure 48: Induction of a phase shift by applying an external magnetic gradient.**

**top:** different field strengths cause different phase shifts over the duration of the gradient in stationary tissue.

**bottom:** Protons of the blood move from areas of low external field strength to higher field strengths experiencing in the average always less dephasing than the stationary tissue they pass.

The phase shift  $\Delta\Phi$  resulting from an applied gradient  $\Delta m$  can be calculated from

$$\Delta\Phi = (\omega_1 - \omega_2) \cdot \Delta t \quad (\text{B.8})$$

and (B.4b) by integration as shown in [28, p.16] leading to the equation

$$\Delta\Phi = \gamma \cdot \Delta m \cdot v \quad (\text{B.9})$$

which shows a proportional relation between phase shift  $\Delta\Phi$  and velocity  $v$ , with the product of the gyromagnetic ratio  $\gamma$  and the magnetic gradient  $\Delta m$  as proportionality factor.

Since the phase shift in the spin echo can be detected and visualized by modern MR scanners, and a single gradient already causes a difference in phase shift between flowing blood and stationary tissue, applying such a unipolar gradient would already suffice to quantify flow. Yet, contrast between stationary and dynamic tissue would be rather poor. It, however, can be improved by applying a second gradient with opposite direction after  $\frac{1}{2} \cdot \Delta t$ , as Figure 49 illustrates:

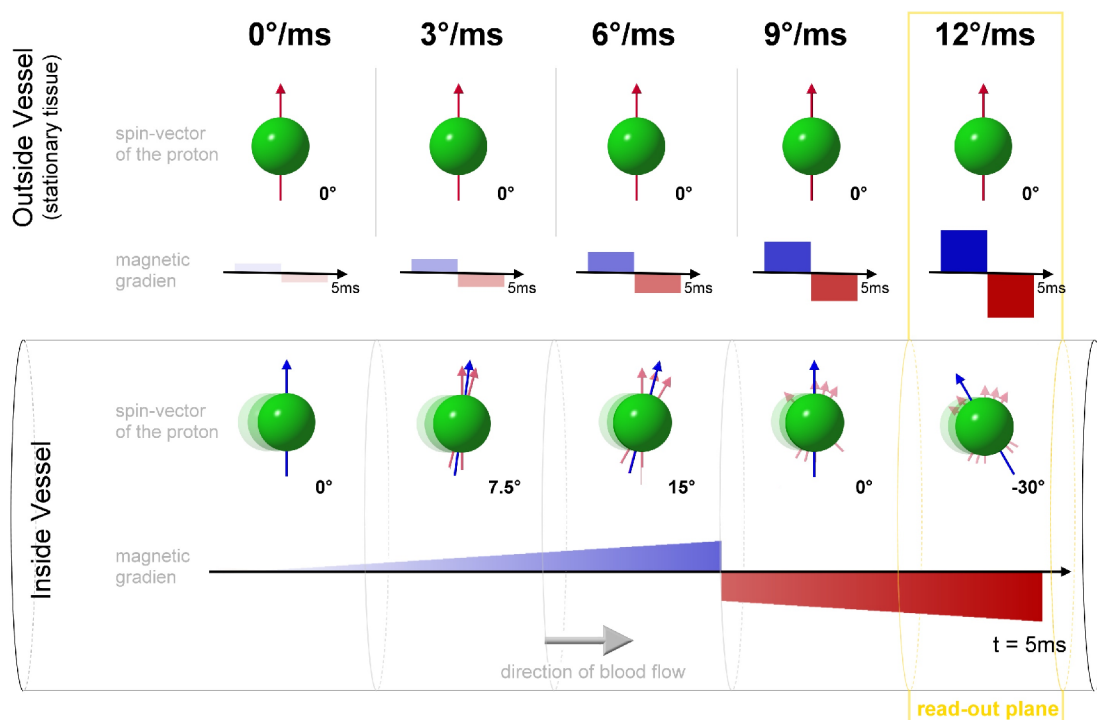


**Figure 49: Applying a bipolar gradient improves phase contrast towards stationary tissue annihilating phase shift of stagnant protons.**

Engaging a gradient with opposite polarity but equal strength after half of the dephasing time  $\Delta t$  allows the stationary tissue to rephase and thus any previously acquired phase shift is annihilated in that tissue. Moving protons however do receive a stronger dephasing during the second half of the dephasing time and the initial dephasing is thus overcompensated resulting in a net dephasing when these protons reach the imaging slice.

Figure 49 also illustrates the reason for the directional sensitivity of phase contrast imaging as it was a predominating issue throughout this thesis: only those protons moving roughly parallel to the gradient (i.e. perpendicular to the imaging slice) receive a phase shift.

The second weakness of PCA mentioned, the limited velocity range can also be envisioned by means of Figure 49:

As Krestin points out:

*“Since phase is unique only over  $360^\circ$ ,  $v_{enc}$  determines the largest measurable velocity”*  
[14, p.5]

and Heiland notes that already angles higher than  $180^\circ$  cause aliasing in the form of leaps in phase. The reason for this is, that flow phase shifts between zero and  $180^\circ$  belong to flow parallel to the encoding gradient and phase shifts between zero and  $-180^\circ$  are caused by flow anti parallel to the gradient.

In other words, because the phase shift is proportional to the velocity of the protons, protons faster than  $v_{enc}$  will cause phase shifts larger than  $180^\circ$ , which will be interpreted as shifts smaller than  $0^\circ$ . Figure 50 taken from [17] illustrates the effect.

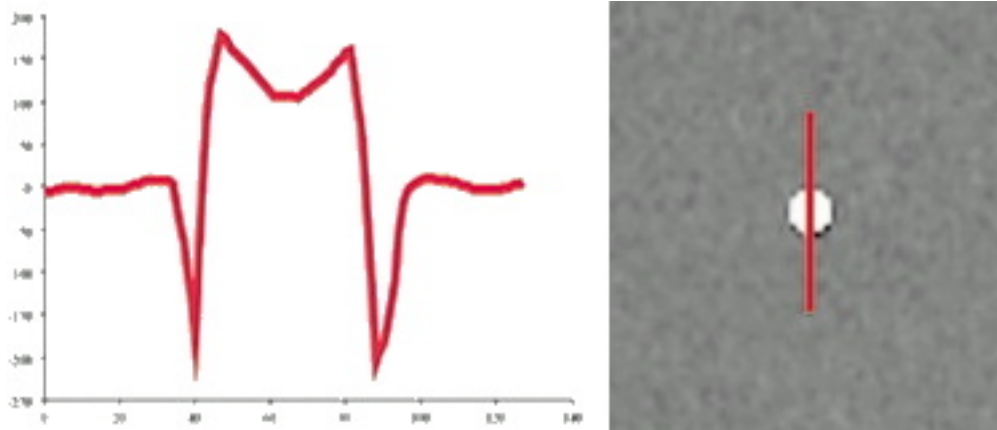


**Figure 50: Velocity aliasing caused by exceeded  $v_{enc}$**

Unfortunately the image has a quite low resolution, but as can be read in [17, p. 657] the picture shows the results of an experiment with a flow velocity of 320 cm/s and a constant  $v_{enc}$  of 210 cm/s. The abscissa gives the positions of the different sampling points taken along the red line in the right part of Figure 50, the ordinate reflects the measured flow velocities as gathered from the grey values of the PCA image on the right. As can be seen, flow velocities higher than  $v_{enc}$  are somehow “warped around” as Oppelt [23, p. 655] calls it.

Figure 51 shows an example for such a velocity artifact from the axial scan of the Ohio-data, showing a typical bright/dark leap.



**Figure 51: Velocity artifact in the sinus rectus as it can be found in the axial scan of the Ohio-data.**

The artifact was already mentioned in section 6.4, where it was suspected to have caused a leap in the sample 5 of Figure 42.

The velocity encoding is parameterized by „*the pulse amplitude and the distance between the gradient pulse pairs.*“ [39]. Yet, setting  $v_{enc}$  very high is not feasible either, as Pelc et al. explain:

“*...noise in flow measurement is minimized whenever velocity encoding ( $v_{enc}$ ) is as small as possible.*” [26, p. 809].

Thus, the highest expectable flow velocity within the ROI and hereby  $v_{enc}$  has to be estimated in advance.

### **B.3 Some remarks about other techniques**

There are numerous other imaging techniques capable to depict cranial vessels. Most of these use contrast agents. These are substances which are, depending on the imaging technique, either opaque to X-rays or alter the magnetic properties of the protons in their vicinity<sup>76</sup>. MR imaging techniques which make use of contrast agents to depict vessels are called Contrast Enhanced MRA (CE-MRA). These methods are not completely none invasive, since the contrast agent can cause allergic reactions.

Apart from PCA, there exists another MR technique, which is capable to depict vessels with high contrast and does not rely on the application of a contrast agent, called Time-of-Flight (TOF). Its functional principle is to excite all protons in the read-out slice (as described in section B.1.3) until saturation is reached. The saturated protons do only emit a dim signal, if the time between the exiting pulses is shorter than T1. Flowing blood, however, moves unsaturated spins into the read-out plane, which produce a much brighter signal during the relaxation time. TOF poses a better contrast and is more suited for the imaging of small vessels than PCA, but it cannot be used to quantify flow, since there exists no correlation between signal strength and flow velocity [8, pp. 678].

---

<sup>76</sup> The agent is injected in the vessel, which is to be depicted immediately before or during the scan.

## Appendix C: Annotations Regarding the Software

The software was implemented in C++ and makes use of three major class-libraries:

- VTK

For most visualization tasks as well as approximately two third of all filter operations the open source library VTK (visualization toolkit) was used (see [43] for details). It is based on OpenGL but encapsulates it and is object oriented. Apart from some interfaces it is platform independent.

- ITK

While it does not provide classes for visualization, it amends some advanced filtering operations when used together with VTK. The provided filtering operations have an emphasis on medical applications, especially segmentation and registration. Like VTK it is platform independent.

- MFC

For the software framework as well as for the user interface the Microsoft-Foundation-Class library (MFC) was chosen, since it provides a mature object oriented framework for application development. Other frameworks like QT might provide this as well, but the prevalence of MFC makes it more likely that the interface to the utilized graphical libraries is mature and well tested. In addition the MFC seamlessly supports direct Windows-API calls which are usually more potent as well as efficient than other interfaces and its compatibility with all current Microsoft operating systems has been well proven.

The data processing itself happens in a separate rendering thread to allow user interaction during rendering. The individual steps of this image data processing are explained in detail in the chapters 3, 4 and 5 of this thesis. An overview of the application flow apart from these processing steps is displayed in Figure 52.

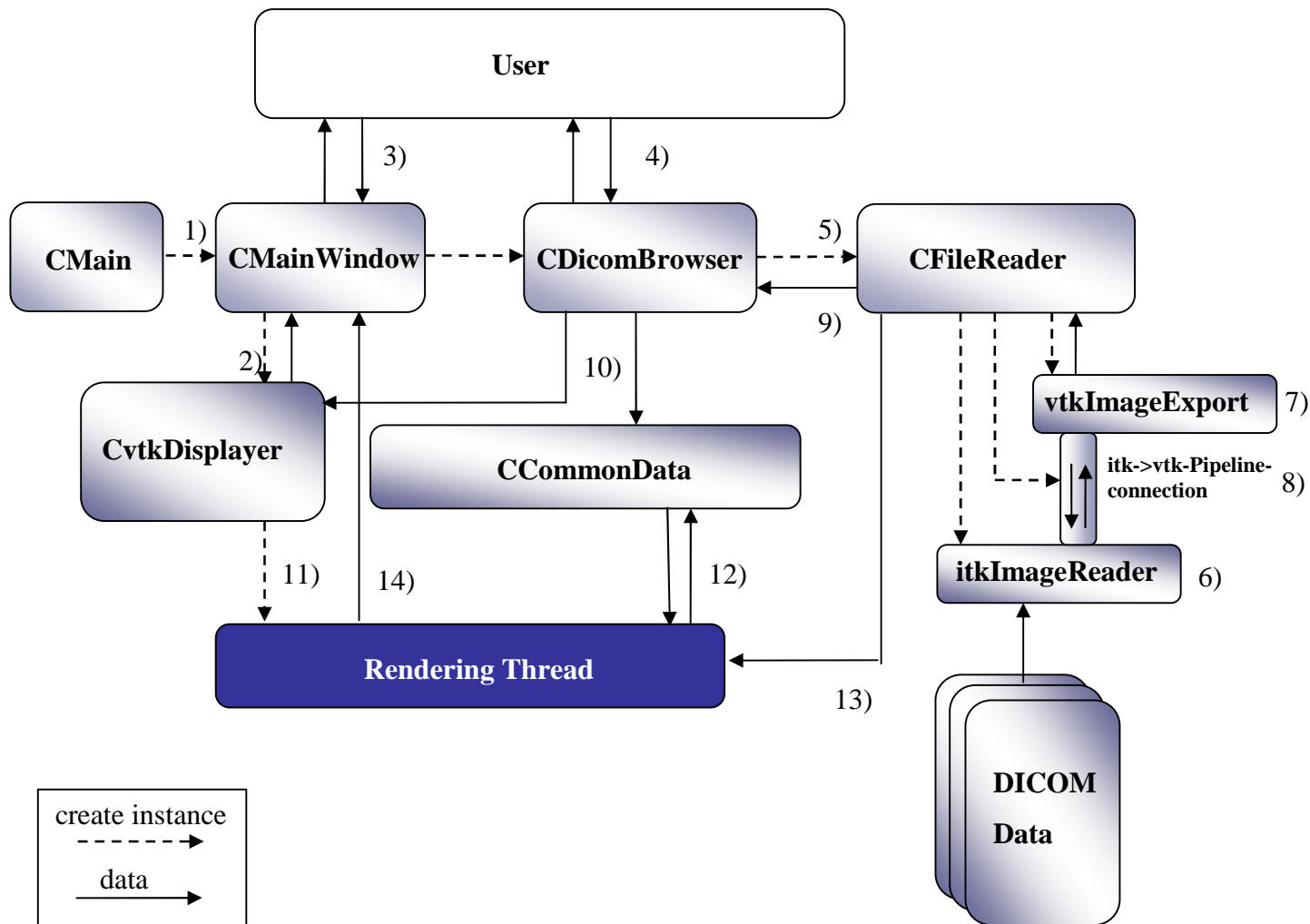


Figure 52: Application flow

The image processing steps within the rendering thread are explained in the chapters 3, 4 and 5 of this thesis, the figures are explained below

- 1) The main-window instance of class CMainWindow is created at the beginning of execution.
- 2) An instance of the Displayer-class is created on initialization but in the beginning just renders a blank screen which is displayed by the CMainWindow-instance
- 3) The user tells the main-window to create and open a DICOM-Image-Browser-instance
- 4) After the user has selected a dataset
- 5) a instance of the class CFileReader is created<sup>77</sup>, which itself invokes
- 6) an instance of itkImageReader
- 7) and an instance of the ITK-class vtkImageExport.
- 8) As soon as the DICOM data has been read in, the itkImageReader passes it to the vtkImageExport-instance over a global pipeline-connection function.
- 9) The CFileReader-instance makes the data available for previewing by the CDicomBrowser instance.
- 10) As soon as the user confirms the data, a reference to the data is given to an instance of the thread save singleton CCommonData and CvtkDisplayer is told to invoke data processing.
- 11) CvtkDisplayer starts a new thread to prevent the user interface from freezing.
- 12) The instance of CvtkDisplayer running in the rendering thread takes the reference to the data read by the CFileReader-instance from the CCommonData singleton
- 13) and passes the data to its methods in order to process it as described in the chapters 3, 4 and 5.
- 14) During data procession, all rendering results are passed to the CMainWindow-instance for displaying.

---

<sup>77</sup> Strictly speaking the steps 5 to 8 already happen during the file browsing in order to render preview images. Despite two different kinds of readers (one reads the metadata for user information and groups files possibly belonging to different DICOM-datasets the other just reads single DICOM-images instead of whole volumes for quicker previewing) the steps are identical to the ones which are finally required to read the whole dataset.

**Bibliography**

- [1] Amin-Hanjani, S.: *“Evaluation of extracranial–intracranial bypass using quantitative magnetic resonance angiography”*, Neurosurg 106, 2007
- [2] Bertram P.: *“Segmentation and Visualization of Vessel-Trees in the Brain”*, 2007
- [3] Bronstein, I.N. et al.: *“Taschenbuch der Mathematik - 5. Auflage”*, Verlag Harri Deutsch, 2000
- [4] Eiho, Sekiguchi, S.H., Sugimoto, N. et al.: *“Branch-Based Region Growing Method For Blood Vessel Segmentation”*, Systems and Computers in Japan, 2005
- [5] Frangi A.F.et. al: *“Multiscale Vessel Enhancement Filtering”*, Springer, 1998
- [6] Gonzalez, R.C., Woods, R.E.: *“Digital Image Processing, 3rd Ed”*, Prentice Hall International, 2002
- [7] Grangova, M. et al.: *“Fast Phase Contrast Imaging At A Single Time Point - A Feasibility Study”*, Proc. Intl. Soc. Mag. Reson. Med 9, 2009
- [8] Heiland S. et al.: *“MR-Angiographie: Technische Grundlagen und Anwendungen in der Diagnostik neurologischer Erkrankungen”*, Georg Thieme Verlag, 2001
- [9] Hemmingsson, A.: *“MR-Angiography”*, Bayer Schering Pharma AG (Publisher), 1998
- [10] Hoffmann, K.: *“Bewertung der globalen linksventrikulären Funktion”*, 2005
- [11] Hoogeveen, R.M. et al.: *“Real-time Quantitative Flow using EPI and SENSE”*, Proc. Intl. Soc. Mag. Reson. Med 9, 2001
- [12] Keil A. ,Navab, N.: *“Computer Aided Medical Procedures”*, Chair for Computer Aided Medical Procedures, 2007
- [13] Konen, Zielke: *“Bildverarbeitung und Algorithmen - Skript zur Vorlesung”*, Fachhochschule Köln, 2007
- [14] Krestin, G.P.: *“Magnetic resonance angiography in the abdomen and pelvis”*, STAR, 1996
- [15] Lamy, J.: *“Integrating digital topology in image-processing libraries”*, Elsevier Ireland Ltd, 2005

- [16] Laub, G. et al.: *“Techniken der Magnetresonanz-Angiographie”*, electromedica, 66/2, 1998
- [17] Lotz J., Meir C., Leppert A. et al.: *“Cardiovascular Flow Measurement with Phase-Contrast MR Imaging: Basic Facts and Implementation”*, RSNA, 2002
- [18] Maier, F.: *“Vessel Segmentation - Final Report”*, 2006
- [19] Merziger G. et al.: *“Formeln und Hilfen zur höheren Mathematik”*, Binomi Verlag, 1996
- [20] Moran, P.R.: *“A Flow Velocity Zeugmatographic Interlace for NMR Imaging in Humans”*, Magnetic Resonance Imaging Vol. 1, Pergamon Press, 1983
- [21] Nekolla S.G.: *“Principles of Tomographic Imaging”*, 2006
- [22] Netter, F.H. et al.: *“The Interactive Atlas of Human Anatomy Version 3.0”*, DxR Development Group, 2003
- [23] Oppelt, A (Ed.): *“Imaging Systems for Medical Diagnostics: Fundamentals, Technical Solutions and Applications for Systems Applying Ionizing Radiation, Nuclear Magnetic Resonance and Ultrasound (2nd Edition)”*, Publicis Corporate Publishing, 2005
- [24] Park J.B. et al.: *“Measuring time-averaged velocity with ungated Spiral and 2DFT Phase-Contrast MR”*, Proc. Intl. Soc. Mag. Reson. Med 9, 2001
- [25] Passig K., Scholz A.: *“Lexikon des Unwissens”*, Rowohlt Verlag, 2007
- [26] Pelc, L.R. et al.: *“Arterial and Venous Blood Flow: Noninvasive Quantitation with MR Imaging”*, RSNA, 1992
- [27] Pless, D., Boll, D.T., Fleiter, T.R.: *“Validierung der numerischen Blutfluss-Simulation (CFD) am Aneurysmen- und Bifurkationsmodell”*, Uniklinikum Ulm, 2002
- [28] Reiser, M., Semmler, W.: *“Magnetresonanztomographie”*, Springer Verlag, 1997
- [29] Sadleir, R.J.T. , Whelan, P.F.: *“Colon Centerline Calculation for CT Colonography using Optimised 3D Topological Thinning”*, Dublin City University, 2004
- [30] Schreckenberg, M.: *“Basics of Medical Ultrasound Imaging”*, 2006
- [31] Sedgewick, R.: *“Algorithmen in C”*, Addison-Wesley, 1992
- [32] Sobotta, J., Putz, R., Papst, R.: *“Atlas der Anatomie des Menschen”*, Urban & Schwarzenberg, 1993

- [33] Summers, P.: *“Multi-site Comparison of Accuracy, Linearity and Precision in MR Flow Measurements”*, Proc. Intl. Soc. Mag. Reson. Med 9, 2001
- [34] Telea, A., Vilanova A.: *“A Robust Level-Set algorithm for Centerline Extraction”*, G.-P. Bonneau, S. Hahmann, C. D. Hansen (Editors), 2003
- [35] Zaho, M., Charbel, F.: *“Real-time prescription by three-dimensional vessel localization in cine phase-contrast flow measurement”*, Proc. Intl. Soc. Mag. Reson. Med 9, 2001
- [36] Zhao, Charbel, Alperin, Loth, Clark: *“Improved phase-contrast flow quantification by three-dimensional vessel localization”*, Elsevier, 2000
- [37] Zhou, R. W., Quek, C. et al.: *“A novel single-pass thinning algorithm and an effective set of performance criteria”*, Pattern Recognition Letters 16/Issue 12, 1995
- [38] <http://medical.nema.org/dicom/geninfo/Brochure.pdf>, 02/2008
- [39] <http://www.mr-tip.com/serv1.php?type=db1&dbs=phase%20contrast>, 02/2008
- [40] [http://www.philippi-trust.de/hendrik/braunschweig/wirbeldoku/hagen\\_poi.html](http://www.philippi-trust.de/hendrik/braunschweig/wirbeldoku/hagen_poi.html), 02/2008
- [41] <http://www.vassolinc.com>, 02/2008
- [42] <https://simtk.org/xml/index.xml>, 02/2008
- [43] <http://www.vtk.org/>, 02/2008